Safety Investigation of Millimeter Wave Radar to Monitor Vital Signs in the NICU

C.R. Ramsey

Safety Investigation of Millimeter Wave Radar to Monitor Vital Signs in the NICU

by

C.R. Ramsey

to obtain the degree of Master of Science
at the Delft University of Technology,
to be defended publicly on Thursday October 8, 2020 at 09:30 AM.

Student number:	4936450	
Project duration:	October 1, 2019 – October 8, 2020	
Thesis committee:	Prof. dr. ir. W. A. Serdijn,	TU Delft, supervisor
	Dr. M. Spirito,	TU Delft
	Dr. M. Alonso del Pino,	TU Delft
	Ir. T. G. Goos,	TU Delft & Erasmus Medical Center

This thesis is confidential and cannot be made public until December 31, 2024.

An electronic version of this thesis is available at http://repository.tudelft.nl/.
Q&CE-AQUA-MS-2019-14

Acknowledgements

Before I present my master thesis, I would like to thank all of the people who made it possible. First, I would like to thank my daily supervisor Tom Goos. He not only supported me continuously during my thesis research but also helped me write multiple grants in hopes of continuing this work. I truly believe this technology can help many people when applied in the healthcare domain, and I am glad to say Tom shares my passion. He was always readily available for consultation and assistance, and, of course, other application ideas.

Second, I would like to thank Wouter Serdijn and Marco Spirito. Wouter's feedback and Marco's support were both of significant value, and, without either, I wouldn't be where I am today. Their contributions helped me increase the scientific value of my research. Third, I would like to thank Maria Alsonso Del Pino for her constant assistance. Without our weekly meetings, I would not have had maintained a consistent direction towards research that will contribute to the improvement of neonatal healthcare.

A special thanks to Carmine de Martino for his help with my lab set-up and Jos van 't Hof for his patience with my continuous stream of lab questions. I would also like to thank Ger de Graaf for his COMSOL guidance and Ralph van Schelven for his detailed explanation of e-fields in skin layers. I would like to also thank Luca Zilberti of the Istituto Nazionale di Ricerca Metrologica for his quick responses to my questions about his research and its contribution to my work. I would like to thank Francesco Fioranelli for his help with my signal processing. Furthermore, I would like to thank my proof-readers, who took the time to read my thesis and provide me with important feedback. Without them, my thesis would not be as clear and concise as it is now. I would like to thank my friends and companions in the life of a master thesis student: Ríkarður Jón Ragnarsson, Matthew Al Disi, Shivani Sinha, Gayatri Argawal and Lucas Enthoven. Without our everyday lunch breaks, this project would probably have lasted a lot longer and, more importantly, it would have been a lot less fun. Finally, I would like to thank my family for supporting me throughout my entire studies and the Bioelectronics group for their encouragement.

C.R. Ramsey
Delft, October 2020

Abstract

Neonates are among the most fragile in the human population. Even more so when born prematurely. Their loss of development time in the womb disrupts their growth, and the neonatal intensive care unit environment can add multiple stresses that hinder their development. This can partly be attributed to the intrusive environment of a neonatal intensive care unit incubator. Neonatal development cannot be monitored without multiple wires and sensors, such as pulse oximetry and electrocardiogram (ECG). The strong adhesives of these sensors can hurt the delicate skin of the neonates and the sensors make bonding with parents difficult.

The issue of the intrusive nature of current neonatal healthcare has led this thesis towards something not normally associated with healthcare: radar. Millimeter wave radar with frequency modulation of the continuous wave transmission has been shown to measure adult's heart and respiration rate without contact with the patient. Using the small wavelength and high configurability of frequency modulated millimeter wave radar, the goal will be to scale down this technology from adults to neonates that can be as small as 500 grams.

This thesis provides a look into the application investigation of frequency modulated millimeter wave radar in monitoring neonates. It dives into the the environment of the neonatal intensive care unit incubator and the radar monitoring system operation. The environment is modelled with a thermal focus to avoid high temperature increases caused by the radar module. The system operation is described and the most influential component simulated and characterized. Lastly, the thermal model of the neonatal intensive care unit incubator is validated to understand how the system operation influences the environment. And the radar system operation will be characterized for measuring the smallest amplitude changes of a chest to understand how the environment influences the system performance. The conclusion of this thesis will provide reasoning for why or why not the application of frequency modulated millimeter wave radar has the capability to be safely implemented in the neonatal intensive care unit.

Contents

1

Introduction

Neonates born premature must take a long and arduous path towards health stabilization and monitoring their vital signs, heart and respiration rate, is of significant help to know their progress[1]-[3]. For example, 75% of all neonatal deaths occur during the first week of life in Europe with two of the main causes being infection and asphyxia[4]. Monitoring heart rate (HR) and respiration rate (RR) help detect both[3],[5]. But monitoring these vital signs are cumbersome due to the required contact of sensors. Not only is the skin of newborns delicate[6], but the wires used to monitor them can be many and thus constraining[7]. This can restrict sleep, which is a critical activity in neonatal brain development[8]. And there is a significant impact skin to skin contact with parents has in aiding neonatal development[9]. Yet, the multitude of wires stops this physical bonding during this especially critical time[7].

Millimeter wave radar has been introduced in the automotive industry as a sensor that can assist drivers and even help cars drive themselves[10]. It is the same concept as other radars, there is a transmitted signal that bounces off the world around it to be received back again by the same sensor[11]. After mixing together the transmitter output and receiver input, a tone is seen in the frequency domain[12]. In the case of automotive radar, this tone is generally the position of another car nearby. What makes millimeter wave radar different is its high frequency. In the 30-300GHz range[13], as in electromagnetic waves with a wavelength measured in millimeters, it has low absorption to rain, fog, smoke, and dust making it ideal for assisting in driving in dangerous road conditions[14]. But another avenue being pursued in the automotive industry is contactless driver monitoring[15], something that can be transferred to healthcare in contactless patient monitoring.

Millimeter wave does not penetrate deep into the body, in all actuality its highest penetration depth into the skin is barely a millimeter[16]. But, the heart and lungs push on the chest causing it to move, and this high frequency radar can measure these small displacements[11]. The sensor can not only pinpoint the patient but see how the patient is moving or, for a more specific example, breathing[15]. In the frequency domain, the heart and lungs have completely different behaviors, so differentiating between the two is quite simple[11]. When breathing, the lungs have a behavior that can be translated to a large amplitude and low frequency. As for the heart, it has a small amplitude and high frequency. Simple bandpass filters can be used to focus on either[17].

The goal is to take this concept and scale it down to fit the characteristics of premature neonates within their clinical environment. With such a small wavelength the goal would be to detect the minute displacements in the chest that lower frequency sensors cannot[18]. But the difficulties of scaling down a technology for an adult to an extremely small baby, sometimes with a weight of 500 grams[19], can be many. For example, a premature neonate's heart pumps blood throughout the body at a higher frequency than an adult[20] and this number can vary greatly over time[21]. These factors coupled with a much smaller amplitude means extracting the neonate's heartbeat from the noise of its environment becomes much more complicated than if doing so for a driver of a car. But another benefit of this radar technology is the use of a modulation technique called frequency modulated continuous wave (FMCW). Instead of continuously transmitting at one frequency, this sensor sweeps the frequency over time[11]. So, for example, instead of operating at only 78.5GHz, it sweeps the transmitter's output signal between 76 and 81GHz over a designated time interval. The flexibility and

variability of FMCW make it potentially more accurate than continuous wave (CW) Doppler[11], and so it could help when pushing millimeter wave radar towards the edge of its abilities.

The introduction of new millimeter wave radar could be very beneficial in aiding such small patients, but they pose a question of safety. The Institute of Electrical and Electronics Engineers (IEEE) determined the only potential harm millimeter wave radar could do onto the patient is in the thermal domain[22]. That means, burns or thermal pain. Many researchers have investigated the thermal output of the highest output power allowed by IEEE and other regulatory agencies[23], yet they have done so in an cool ambient environment with adult skin structure and high blood perfusion. In order to determine the safety of millimeter wave radar and its use in the neonatal intensive care unit (NICU) incubator, further investigation into millimeter wave's heat effects is required.

Previous research in millimeter wave radar thermal safety lacks investigation into the impact age and environment have on thermal increase of the skin. For example, Ziskin et al.[24] acknowledges that infant skin has many different properties that make it different from adult skin. Infant skin is significantly larger in surface area to body volume ratio, the stratum corneum has a higher water content and is thinner, the papillary dermis is thinner and production of sweat is reduced making it so a baby is not able to regulate its body temperature as well as adults. Ziskin et al.[24] acknowledges the elderly have different skin composition as well, which is important to researchers who want to monitor elderly falls, yet Ziskin et. al[24] only focuses on the thermal dosage an adult would receive. Another important note about neonates is they have a higher chance of becoming septic compared to other age ranges[25], which causes blood flow through the tissue to go to zero[26]. As blood flow decreases, temperature increases because the blood in tissue is what dissipates the heat throughout the body[27].

And when it comes to the environment, a NICU incubator crib environment is quite dissimilar to the ambient environment commonly used in RF thermal calculations. The NICU crib has a relative humidity between 60-80% and the ambient temperature is around 36.5C[28] compared to the ambient temperature of 23C and relative humidity of 0% assumed in most models[24],[27],[29]. The convection fan pushes air from the head to the feet[30], maybe the only environmental variable similar to an adult i.e. one who is sitting underneath air conditioning. These factors should be acknowledged since they change the heat transfer coefficient that is normally assumed in RF thermal calculation models.

The combination of skin structure and environment composition is required when using millimeter wave radar to branch out in healthcare. Premature neonates are in an extremely vulnerable state and their safety is priority. And these precautions should be extended to other scenarios where healthcare could benefit from millimeter wave radar, even outside a hospital setting should be of interest since adults won't be the only one using 5G, another technology using millimeter wave radar. Consequently, the main goal is to determine how to safely use millimeter wave radar to monitor neonatal vital signs in a NICU clinical setting and if FMCW millimeter wave radar has the capability to scale down from adults to neonates to measure very small chest displacements. These results will help continue the investigation of whether millimeter wave radar can be used to monitor the vital signs of premature neonates in the NICU itself.

1.1. Problem Statement

Neonates are among the most fragile in the human population. At this early point in life, what happens to a neonate affects them for the rest of their lives. And so, there is constant investigation to improve these delicate beings' health and safety. When monitoring premature neonates, today's sensors require adhesive contact to determine their health status. This can be of issue because premature neonates have delicate skin, so removal of sensors can be harmful. In order to solve this problem, sensors that reduce their direct contact with the patient need to be investigated and implemented safely. A new sensor using millimeter wave radar can measure respiration rate and heart rate without any contact with the adult being monitored. Radar has not normally been implemented in healthcare, but currently more precise, smaller and cost effective sensors have been introduced that make it easier to fit them into a clinical setting. The main goal of the thesis is to scale down the current system that monitors adults to implement new millimeter wave radar sensors in a safe manner and thus help improve neonatology healthcare.

1.2. Objectives

In order to investigate the safety of the application of the millimeter wave radar in measuring the heart and respiration rate of a neonate in a NICU incubator, the definition of safety must be clarified. There have been multiple investigations into how millimeter wave can negatively affect the health of a person, but the only harm that millimeter wave RF has been shown to produce is a temperature increase. Because of this, the focus of the thesis is on the temperature increase of the skin a neonate may have while being continuously monitored within the incubator. Within this scope, there were still a few steps that must be done. First, the safety must be defined as to how high the temperature increase could be without harming the neonate, then a thermal model must be produced and validated to correctly calculate the thermal increase caused by millimeter wave and, finally, the parameters of the radar configured, with help from the model, to remain within the defined safety limits. Another investigation was done into the capability of FMCW millimeter wave radar has of measuring the chest displacement caused by the heart and lungs of a neonate, some as small as 500 grams. This was done by measuring the smallest amplitude the radar evaluation module could measure using FMCW parameters designed to measure the heart and respiration rate of an adult and signal processing techniques similar to the ones done for the heart and respiration calculation from radar data. Consequently, the objective can be broken into two parts: understanding the environment and understanding the system, so that they can be put together to safely implement FMCW millimeter wave radar. The final work were divided into several tasks:

- To model the environment and implementation of radar with a thermal focus for safe implementation
- To describe the system and model and characterize certain components for NICU implementation
- To validating the system component models and thermal model for clinical scenario
- To combine knowledge of system and environment to understand how to implement the system safely

1.3. Boundaries

The thesis will not investigate other potential areas of harm. Since the IEEE has determined the only potential source of harm caused by millimeter wave radar for humans is the thermal increase it causes on the skin, the investigations into other health effects will not be undertaken. These include membrane effects on a cellular level, stimulation of immune system, influence on gene expression, increase in cellular proliferation, etc. that have been investigated previously but no effect has been shown.

1.4. Outline

Chapter 1, the introduction, gives the background information on the project. It begins with the problem statement to help explain the project objectives. The boundaries of the project were also stated to define the project scope.

Chapter 2 focuses on the environment the system will be applied in. It will analyze the modelling of the thermal increase for a neonate in a clinical scenario. It is divided into four parts: the explanation of why only the thermal hazard was considered, the heat transfer coefficient calculation, the continuous wave thermal model and the analysis of the thermal model created.

Chapter 3 focuses on the system itself. It describes the system model, overviewing how the entire system will work and then focuses on a specific component that must be understood for safe implementation. The simulation and characterization of the component is given.

Chapter 4 explains the validation of the environment and system model. It explains how the thermal model was validated and the resulting updates to the initial thermal model. Then, it explains the FMCW configuration and signal processing validation for measuring the smallest amplitude detection of a neonate's chest.

Finally, Chapter 5 will give a conclusion of the thesis as well as future work to bring the proof of concept to fruition in a clinical application.

2

Thermal Modelling of Clinical Scenario

Implementation of millimeter wave radar to monitor neonates has been broken into two parts: the system and the environment. In this chapter, the thermal model of the clinical scenario is modelling of the system's operation in the neonate's environment. There are hazards a continuous stream of electromagnetic radiation could cause, addressed individually in the first section, with the conclusion being temperature increase is the only one with actual potential for harm. Using this conclusion, first how to incorporate a neonate's environment into the thermal model will be addressed with the calculation of a NICU incubator's heat transfer coefficient. Then, the explanation of how to model biological tissue in a way that incorporates electromagnetic waves will be given in order to describe the temperature elevation equations. The final section will combine both heat transfer coefficient and temperature elevation equations to create the thermal model.

2.1. Thermal Focus Explanation

A compilation of studies was done that investigate what effects a continuous stream of millimeter electromagnetic waves could have on the human body. And from this research, multiple possibilities were found. All but temperature increase were dismissed due to a variety of reasons. This section focuses on what those possibilities are and their specific reason as to why they were not included in the final safety investigation.

First, the influence of millimeter wave radar on gene expression, the processing done inside a living organism where information from a gene is used to create a protein or any other gene product[23], was looked into. Logani et al.[31] investigated the genotoxic potential, potential to cause cancer, of 42.2GHz millimeter wave radiation on adult male mice. Quément et al.[32] did the same for 60.4GHz with an average incident power of 1.8mW/cm^2 and Zhadobov et al.[33] also studied 60GHz but at very low power densities, 5.4nW/cm^2 and 0.54mw/cm^2. All three concluded the millimeter wave frequencies were not genotoxic, which aligns with the view that non-ionizing radiation does not cause cancer.

Millimeter wave frequencies are being researched to treat cancer by overheating the cancer cells to kill them, which aligns with the waves' potential to increase temperature. But there are other implementations of millimeter wave frequencies used to treat cancer that may have an impact on the immune system itself. A drug that is used to combat cancer, cyclophosphamide (CPA), has a negative side effect of enhancing tumor metastasis because it suppresses the natural kill (NK) cell activity. Beneduci et al.[34] researched the effect millimeter wave has on cellular proliferation of tumor cells in order to reduce metastasis when combined with CPA. In the study, low power, less than 50μW, millimeter wave radiation from 50-80GHz was transmitted at tumor cells, which did result in the termination of their proliferation. Radzievsky et al.[35] found a 61.22GHz millimeter wave signal at 13.3mW/cm^2 was able to suppress melanoma tumor growth. Logani et al.[36] studied the effects of millimeter wave radiation at 36.5mW/cm^2 on tumor metastasis and found it reduced cellular proliferation but concluded this was due to millimeter wave radiation's effect on the immune system. Logani et al.[36] found millimeter wave radiation caused an increase in NK cell activity originally suppressed by CPA. And so suggested that a reduction in tumor metastasis by millimeter waves is mediated through the activation of NK cells by these frequencies.

Since millimeter wave radiation potentially stimulates the immune system, Logani et al.[36] proposed they be used in immunotherapy, inclusive in a method to fight cancer. Though this may not technically be considered a danger, it is important to note that the millimeter wave signal ideally would not come into contact with the immune system nor cancer, so the hazard of unnecessarily stimulating the immune system could be ignored. Still, more research was done into the potential millimeter wave transmission has to stimulate NK cells.

Experiments in 1998 with wounded laboratory animals showed a wounded surface under the exposure of millimeter waves healed two times faster than if no radiation was applied[37]. The electromagnetic waves at these frequencies seemed to stimulate the response of the immune system to respond faster and more efficiently. It was shown low intensity 42GHz millimeter wave exposures has anti-inflammatory effects on humans[38],[39]. This may be attributed to the fact the electromagnetic waves heat the tissue simulating a fever causing the rest of the immune system to respond faster. Still, an immunologist at Erasmus Medical Centre was consulted. He went through a few of the studies and determined they did not have sound conclusions and there wasn't more support of their research from other sources. The decision was to remove the investigation of the immune system stimulation potentially caused by millimeter wave radiation from the safety requirements of the thesis.

The last effect studied was how the millimeter wave could affect cellular membranes. The cellular membrane is a phospholipid bilayer that protects the contents inside a cell from its outside environment. Several studies have reported millimeter waves may have some effect on this membrane. Zhadobov et al.[40] suggested 60GHz millimeter wave exposure at power density levels around 0.9 mW/cm^2 created an increase of lateral pressure in artificial membranes. Szabo et al.[41] observed modification, without cellular damage, in cellular membranes during 42.2GHz exposure at a power density of $35.5mW/cm^2$. Szabo et al.[41] suggests this modification can still effect cellular signaling or other interactions even if there was no cellular damage.

Zhadobov et al.[40] and Szabo et al.[41] theorize that millimeter wave radiation can interfere with the orientation of charged, dipolar molecules in cellular membranes. With this potential, there is a potential for it to modify the neural membrane's permeability potentially stimulating neuron endings or affecting the electric signal transmitted to the rest of the body[42]. Thus, Zhadobov et al.[40] proposes millimeter wave can change one's environmental perception, such as creating the sensation of pain. However, applying oscillating electromagnetic fields to reorient large, dipolar molecules, even when the molecules are free to rotate, is not known to occur above the low megahertz frequency band. It would be difficult to explain why molecules that are bound by other molecules, as in a membrane, can be influenced by millimeter wave frequencies considering the current understanding of its interaction with large, dipolar molecules[43]. The main reason the potential for millimeter wave to affect cellular membranes, though, was that the neither research from Zhadobov et al.[40] nor Szabo et al.[41] have been independently reproduced.

Since these studies either did not fall within the application space of the thesis, were not reproducible or were found to have no negative effects in different respects, temperature increase was only included in the safety investigation. The temperature increase was researched for its potential to cause thermal pain and burns. Thermal pain occurs around 10C above normal skin temperature and thermal burns occur at temperature increases that are considerably higher[27]. There has been research into using millimeter wave as nonlethal crowd control, but these power densities reach $10{,}000W/m^2$ in order to cause only 8 second-degree burns out of 11,000 exposures[23]. The maximum power that will be used is $10W/m^2$. Still, neonates are unable to show pain because they cannot cry or otherwise communicate, and so the temperature increase of these millimeter wave frequencies needs to be understood in the application of the system.

2.2. Heat Transfer Coefficient Calculation

In order to compensate for the environmental influence a neonate's NICU incubator has on the temperature increase caused by the electromagnetic waves, the current millimeter wave thermal increase models need to be adjusted from their normally assumed environmental variables. The variables that need to be modified within the thermal models are ambient air temperature and relative humidity, since those have the most influence on the heat loss types within a NICU incubator. Since those variables are not directly transferable to

the model created, the change in relative humidity and ambient air temperature need to be incorporated into the heat transfer coefficient, a variable intended for environment adjustment in the thermal model.

Ambient air temperature and relative humidity cause a significant change in the value of the heat transfer coefficient. In a NICU incubator, these environmental values are meant to keep the neonate from reaching hypothermia. For example, the ambient air temperature in a NICU incubator is generally very close to the skin temperature. A neonate is basically unable to regulate its body temperature. For an incubator to regulate a neonate's temperature for them, it needs to be as close to ideal skin temperature as possible making the neonate's skin temperature as close to ideal as possible.

There are four forms of heat loss: convection, conduction, radiation and evaporation, see Figure 2.1[44]. In the incubator these come down to the fan that moves air from head to feet (convection), the heat loss from the neonate to the mattress (conduction), the heat loss due to the difference in the surrounding air outside the incubator (radiation) and the heat loss due to sweating (evaporation)[45]. In order to reduce convective and radiative heat loss, the air temperature is kept the same as the skin temperature and moved throughout the crib at a very low speed. The air humidity is kept relatively high to reduce evaporative heat loss. And the mattress is heated to reduce the conductive heat loss. The difference in mattress temperature and neonate temperature is so small that conduction heat loss is normally ignored in neonatal heat loss calculations.

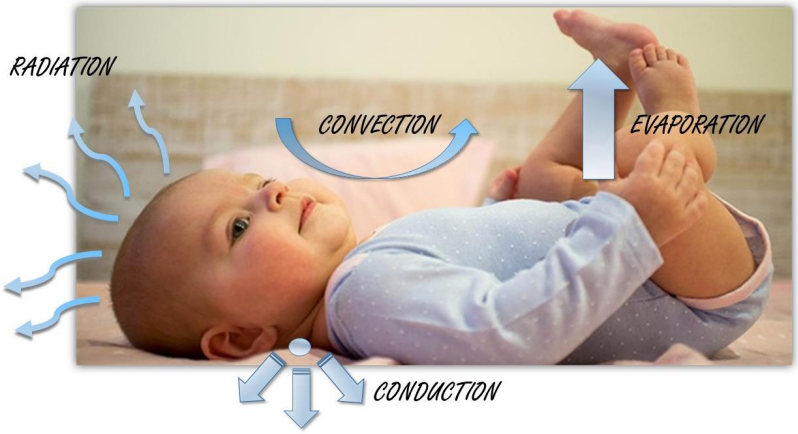

Figure 2.1: The four forms of heat loss for a neonate according to the World Health Organization (WHO)[44]

In order to take into consideration the three heat loss factors with significant heat loss contributions, multiple neonatal heat loss papers were read. Many researchers did not include evaporative heat loss in their calculations[45]. It is very difficult to include evaporation in heat loss calculations because mannequins are normally used as replicas for neonates in these measurements as not to endanger a neonate, and it is difficult to simulate sweating in a mannequin. Thus, many studies only were able to calculate convection, conduction and radiation heat loss (dry heat losses). One paper was found that did incorporate the evaporative heat loss measurement: Belghazi et. al[46]. The researchers were able to build a mannequin that could mimic sweat by pumping water throughout a mannequin that had small holes for the water to escape, see Figure 2.2[46].

Figure 2.2: The 'sweating' mannequin used by Belghazi et. al to calculate total heat loss caused by evaporation on the skin of the neonate[46]

Though Belghazi et. al[46] solved the problem of calculating evaporative heat transfer coefficient, there were many other challenges that arose from trying to calculate the total heat transfer coefficient. Each form of heat loss has its own heat transfer coefficient associated with it. Thus, once the heat transfer coefficient for each heat loss form is calculated, an equation must be found that can incorporate all of them together since the millimeter wave temperature increase calculation only uses one heat transfer coefficient. Another challenge was all the studies found in literature were focused on total heat loss of the neonate, not the calculation of the heat transfer coefficient. Consequently, the heat transfer coefficient must be calculated back from the results of Belghazi et. al[46]. Though this may be a better way to determine heat transfer coefficient. In most studies, convective heat transfer coefficient calculation theory is based on standing adults in natural or forced convective environments, which leads to errors when applied to a neonate. Neonates generally have larger convective heat transfer coefficients than adults[45] and a smaller useful area due to lying on a heated mattress.

The last issue is the heat loss calculations from Belghazi et. al[46] did incorporate evaporative heat loss, but they did not give a calculation for this form of heat loss based on relative humidity. The study kept the humidity at a fixed value of 50% inside the incubator and then measured the total evaporative heat loss, resulting in a static heat loss value and thus no way to adjust for an incubator at a different relative humidity. This adds difficulty as the relative humidity for the cribs that will be used in the monitoring application varies between 60% and 80%.

First, the heat transfer coefficients for each heat loss form were calculated individually. For conduction, as stated before, that form of heat loss is next to nothing because the mattress the neonate lays on has almost exactly the same temperature of the neonate. Consequently, it is ignored[46]. The convective heat transfer coefficient was calculated based on the total amount of dry heat loss Belghazi et. al[46] measured. Convective heat loss accounts for 1-3% of dry heat losses in a NICU incubator[46], so 2% of the total dry heat loss measured by Belghazi et. al[46] was used to calculate the convective heat transfer coefficient. The convective heat transfer equation defined as:

$$C = h_c A_c (T_a - \overline{T}_s) \tag{2.1}$$

where C is the heat loss due to convection, h_c is convective heat transfer coefficient, A_c is convective surface area exchanging heat with the environment, T_a is the air temperature and $\overline{T}_s$ is the mean skin temperature. The ambient air temperature, T_a, was set to 33C and mean skin temperature, $\overline{T}_s$, set to 35.7C. Both values taken from the Belghazi et. al[46] study. The convective surface area, A_c, was taken as one half of the body surface area (BSA). The BSA equation is defined as:

$$BSA = 0.2157 Wt^{0.425} H^{0.725} \tag{2.2}$$

where BSA is body surface area, Wt is body mass in kilograms and H is height in meters. The skin temperature and ambient temperature of the validation scenario in Chapter 4 were different than the Belghazi et. al[46] study. Consequently, a convective heat loss ratio between the two scenarios was realized to adjust for the discrepancy. In the validation scenario, the ambient air temperature, T_a, was set to 35C and mean skin temperature, $\overline{T}_s$, set to 37C. After calculating the convective heat loss ratio between the validation scenario and the Belghazi et. al[46] study, it was multiplied by the convective heat transfer coefficient, h_c, first calculated and so a new heat transfer coefficient was created based on the validation environment.

For the evaporative heat transfer coefficient, an evaporative heat loss ratio between the Belghazi et. al[46] study and the final application environment was also calculated. But first the evaporative heat transfer coefficient of the Belghazi et. al[46] study needed to be found. This was done using the equation that relates convective heat transfer coefficient, h_c to evaporative heat transfer coefficient, h_e, defined as:

$$h_e = 1.67 h_c \tag{2.3}$$

where h_c is the convective heat transfer coefficient and h_e is the evaporative heat transfer coefficient. Using the convective heat transfer coefficient, h_c, found before the convective heat loss ratio was applied, the Belghazi et. al[46] evaporative heat transfer coefficient was calculated.

Using the resulting evaporative heat transfer coefficient value,h_e, the difference in partial pressure of the skin surface area and air was calculated using the total heat loss caused by evaporation equation defined as:

$$E = h_e A_w (P_{s,H2O} - P_{a,H2O}) \tag{2.4}$$

where E is the total heat loss caused by evaporation, h_{e} is evaporative heat transfer coefficient, A_{w} is the wetted skin surface area available for water evaporation, $P_{\mathrm{s,H2O}}$ is the partial pressure of the skin surface area and $P_{\mathrm{a,H2O}}$ is the partial pressure of the air. Belghazi et. al[46] provided the total heat loss, E, due to evaporation and the wetted skin surface area, A_{w}, was estimated to be around half of the neonate's BSA since part of the neonate is laying on the mattress. Using the evaporative heat transfer coefficient calculated using equation 2.3, the difference in partial pressure of the skin surface area and air was found.

Belghazi et. al[46] used a fix value of 50% humidity for their measurements. In order to adjust for the difference in humidity from Belghazi et. al[46], the partial pressure of the skin at full saturation was found and the partial pressure of the air at full saturation was taken as 65.6mbar. From there, the assumption was both skin and air water vapor increased linearly from 30% skin surface wettedness and 50% relative humidity. So, an increase from 50% to 80% in relative humidity would cause an increase from 30% to 48% water vapor on the skin's surface. Using the saturated values of skin and air, the new vapor difference was found. From here the new evaporative heat transfer coefficient, h_{e}, can be computed.

Finally, the radiative heat transfer coefficient was calculated. The equation for the radiative heat transfer coefficient is defined as:

$$R = h_r A_r (\overline{T}_r - \overline{T}_s) \tag{2.5}$$

where R is the heat loss due to radiation, h_{r} is radiative heat transfer coefficient, A_{r} is radiative surface area exchanging heat with the environment, $\overline{T}_{\mathrm{r}}$ is the mean radiant temperature and $\overline{T}_{\mathrm{s}}$ is the mean skin temperature.

The mean skin temperature, $\overline{T}_{\mathrm{s}}$, for Belghazi et. al[46] and the final application have already been stated. The radiative surface area, A_{r}, was estimated to be around half of the neonate's BSA since part of the neonate is laying on the mattress. This leaves the mean radiant temperature, which must be calculated using the ambient incubator temperature, T_a. This equation given by Wheldon[47] and is defined as:

$$\overline{T}_r = 1.43 + 0.761 T_a + 0.169 T_{room} \tag{2.6}$$

where $\overline{T}_r$ is the mean radiant temperature, T_a is the ambient incubator temperature and T_{room} is the temperature of the room the incubator is in, taken as 23C for all heat transfer coefficient calculations.

Using the new convective heat transfer coefficient and actual skin and ambient temperature of the application environment, a new convective heat loss, C, was calculated using Equation 2.1. Since this new C counts as 2% of the total dry heat losses, it can be used to calculate the radiative heat loss, which is the remaining 98%. Using the new radiative heat loss number and the application radiant temperature, calculated using 2.6 and the application ambient temperature, and skin temperature values, the new radiative heat transfer coefficient is found using equation 2.5.

With all the heat transfer coefficients calculated, they were integrated together to create one variable that could be put into the thermal model as a representation of the NICU incubator. The heat transfer coefficient combination equation was taken from the overall heat transfer coefficient calculation for heat transfer between the fluid inside a pipe and the pipe's external surface. It is defined as:

$$\frac{1}{h_{combined} \cdot A_{combined}} = \frac{1}{h_c \cdot A_c} + \frac{t_s}{k \cdot A_c} + \frac{1}{h_r \cdot A_r} + \frac{t_s}{k \cdot A_r} + \frac{1}{h_e \cdot A_e} + \frac{t_s}{k \cdot A_e} \tag{2.7}$$

where $A_{combined}$ is surface area that the combined heat transfer coefficient will be used for, t_s is thickness of the skin, k is the thermal conductivity of the skin, h_r is radiative heat transfer coefficient, A_r is radiative surface area exchanging heat with the environment, h_e is evaporative heat transfer coefficient, A_w is the wetted skin surface area available for water evaporation, h_c is convective heat transfer coefficient and A_c is convective surface area exchanging heat with the environment.

The results of the heat transfer coefficient calculation showed it to be dependent on not only the environment but also the surface area that the radiation applies to. For example, if only one fifth of the BSA of the neonate is taken into consideration when calculating the combined heat transfer coefficient, then the heat transfer coefficient becomes five times the amount computed for the entire BSA. The heat transfer coefficient showed to depend little on the convective heat transfer coefficient since convective heat loss accounts for only 1-3% of the total dry heat losses. Since the mean radiative temperature, $\overline{T}_r$, is dependent on the ambient temperature, T_a, and the radiative heat transfer coefficient, h_r, is dependent on the mean skin temperature, $\overline{T}_s$, these variables associated with convective heat loss still affect the combined heat transfer coefficient. But the method the mean radiative temperature, $\overline{T}_r$, is calculated using Equation 2.6 and ambient temperature, T_a, has not been validated[45], which adds uncertainty to the resulting value and how ambient temperature, T_a, plays a roll in calculating mean radiative temperature, $\overline{T}_r$.

2.3. Continuous Wave Based Thermal Model

The thermal model produced is dependent on a continuous wave application of the radar module. In the final application of the system, FMCW will be used instead of continuous wave. But continuous wave induces higher temperature increases than FMCW because the transmitter is constantly transmitting with no modulation techniques. The decision to focus on continuous wave was to provide a worst case scenario that is either safe or shown how to be safely implemented. With the worst case scenario considered safely applied, the actual FMCW configuration of the radar module can be as well. In this section, the main bioheat equation will be introduced and its parts broken down to explain how it comes together to create a thermal model.

2.3.1. Penne's Bioheat Equation

Many millimeter wave radar frequency induced temperature increase calculation papers were found: Ziskin[24], Foster[27], Ting[29]. Each paper used the same bioheat equation: Penne's bioheat equation. All of these equations calculated using a continuous wave signal after temperature had stabilized. The Penne's bioheat equation is defined as:

$$\rho c \frac{\partial T(z)}{\partial t} = k \frac{\partial^2 T(z)}{\partial z^2} - h_b(T(z) - T_{blood}) + Q_m + SAR \cdot \rho \tag{2.8}$$

where SAR is the specific absorption rate, Q_m the metabolic rate, T_{blood} is the temperature of blood, k is the thermal conductivity of the tissue, t is time, ρ is the mass density of the tissue, c is the specific heat capacity

of the tissue, z is the distance into the tissue, h_b is the heat transfer coefficient of blood and $T(z)$ is body temperature.

Due to the low penetration depth, the SAR impact is generally ignored as it is extremely small[24]. The metabolic impact is so large that it must be taken out to not interfere with the electromagnetic wave calculation[29]. And the temperature elevation is calculated after temperature is stabilized, so the dependence on change over time goes to zero. Thus, Penne's bioheat equation is usually left with temperature elevation caused by electromagnetic waves as related to the heat transfer coefficient of blood and the thermal conductivity of the tissue. Each paper calculated the increase in temperature differently. Ziskin[24] based it on the power density of the electromagnetic waves, penetration depth of the radio frequencies and blood perfusion of the tissue. Foster[27] based it on only the penetration depth. Ting[29] based it on multiple factors: the reflected and incident electric field, the propagation constant and the characteristic impedance of the tissue. Ting[29] was used for further understanding of modelling the tissue.

2.3.2. Tissues as Transmission Lines

When considering electromagnetic radiation within and around tissue, the electric and magnetic fields must be taken into consideration. As power is transferred between tissues, some energy is reflected back and some energy is reflected forward at the tissue boundary layers. The fields that are reflected back are called the reflected electric field and the waves that are transmitted forward are called the incident electric field. As the distance into the tissue gets deeper, these values change. They get weaker as more power is absorbed into the tissue. Both the incident and reflected electric fields can be combined together to create the total electric field and magnetic field at a certain distance into the tissue. The electric field is defined as:

$$E(z) = E_i^+ e^{-jk_i z} + E_i^- e^{jk_i z} \tag{2.9}$$

where $E(z)$ is the electric field at distance z, E_i^+ is the incident electric field, k_i is the propagation constant of tissue i and E_i^- is the reflected electric field. The magnetic field is defined as:

$$H(z) = \frac{E_i^+}{\eta_i} e^{-jk_i z} - \frac{E_i^-}{\eta_i} e^{jk_i z} \tag{2.10}$$

where $H(z)$ is the magnetic field at distance z, E_i^+ is the incident electric field of tissue i, k_i is the propagation constant of tissue i, η_i is the intrinsic impedance of tissue i and E_i^- is the reflected electric field of tissue i.

Equation 2.9 and 2.10 are both dependent on a variable called the propagation constant, k. And Equation 2.10 is dependent on the intrinsic impedance, η. This is because each tissue has different electromagnetic properties associated with it. The propagation constant, k is a measure of the changes the tissue has on the electromagnetic waves as it propagates through a medium, both for phase and amplitude. The intrinsic impedance, η, is the ratio of the electric field to magnetic field within the tissue.

Each tissue has different propagation constants and different intrinsic impedances. Consequently, at each tissue boundary, the incident wave is transmitted and reflected differently. It is based on the reflection coefficient, Γ, which can be calculated using the tissue's different properties. This equation is defined as:

$$\Gamma = \frac{Z_{in} - Z_0}{Z_0 - Z_{in}} \tag{2.11}$$

where Γ is the reflection coefficient, Z_0 is the characteristic impedance of the tissue and Z_{in} is the input impedance of the preceding tissue.

The characteristic impedance, Z_0, is the ratio of the voltage and current propagating through the tissue and is a given value dependent on which tissue is being measured. The input impedance, Z_{in}, is similarly dependent on the tissue properties but requires further calculations because it incorporates multiple tissue characteristic impedances. When working with two tissues that meet at one boundary, Equation 2.11 can be used without any further calculation. But to use Equation 2.11 when there are multiple characteristic impedances, i.e. tissues, connected next to each other, the input impedance, Z_{in}, needs to be calculated. The equation for calculating Z_{in} is defined as:

$$Z_{in} = Z_0 \frac{Z_L + jZ_0 \tan \beta l}{Z_0 + jZ_L \tan \beta l} \tag{2.12}$$

where Z_{in} is the input impedance, Z_0 is the characteristic impedance of the tissue, Z_L is the load impedance of the subsequent tissue, β is the propagation constant of the tissue and l is the length of the tissue.

As an example for how to calculate the input impedance, Z_{in}, and to show its difference with characteristic impedance, Z_0, the input impedance of the fat and muscle together is explained. Fat is considered before muscle in a body model (skin then fat then muscle), so muscle is considered the 'load' connected to the fat. First, the load impedance, Z_L, of the muscle must be found. Since, it theoretically continues infinitely according to the electromagnetic waves, i.e. no reflections at the end of the tissue, its load impedance, Z_L, is its characteristic impedance, Z_0. Thus, the load impedance, Z_L, in equation 2.12 is the characteristic impedance, Z_0, of muscle. The characteristic impedance, Z_0, of equation 2.12 is the characteristic impedance of fat. Using the length, l, and the propagation constant, β, of the fat tissue, the combination of the fat and muscle tissue impedance, the input impedance Z_{in}, can be calculated. This results in the input impedance, Z_{in}, of fat and muscle combined and will be the new load impedance, Z_L, when combining fat and muscle with skin for an input impedance, Z_{in}, of skin and fat and muscle.

Using this technique to continue to combine connecting tissues, the input impedance, Z_{in}, can be calculated at every tissue interface. And then Equation 2.11 can be used to calculate how the electric fields transmit and reflect within the tissues.

Putting all these variables together: input impedance, Z_{in}, characteristic impedance, Z_0, reflection coefficient, Γ, the tissue layers can be considered a series of transmission lines, see Figure 2.3. In Figure 2.3, each tissue boundary has a new reflection coefficient based on a new input impedance that causes the different values of the incident and reflected electric fields. Each tissue has its own characteristic impedance and leads to the load impedances based on the depth into the model.

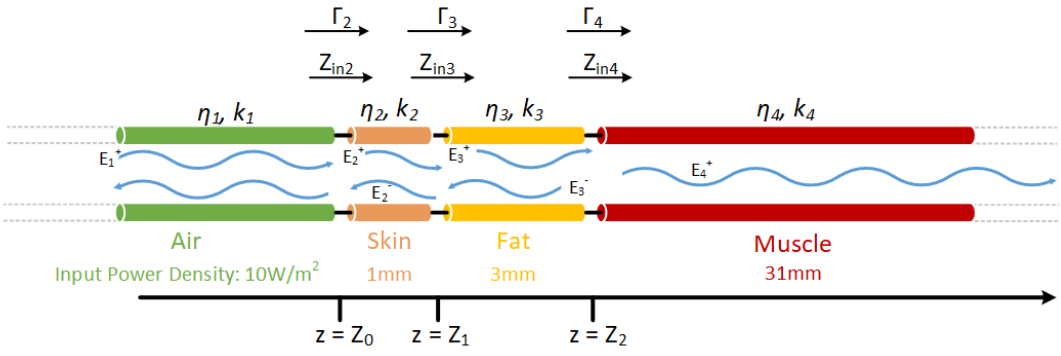

Figure 2.3: Different tissue layers pictured as transmission lines

The tissues can be considered as complex impedance transmission lines of varying lengths connected to each other in series. The air touching the skin and the muscle at the end of the model are both considered infinite. For the muscle, that means there are no reflections at the end of the tissue layer, the energy continues infinitely into the body. This assumption can be made because the energy at the muscle has been accepted as dissipated into the body and thus has no ability to increase body temperature. Because the air can be considered an infinite transmission line before the tissues begin, there is no reflection of the reflected wave back onto the skin.

With a input impedance, Z_{in}, of the entire body model (skin, fat, muscle), the reflection coefficient of the air to body can be calculated. Now the amount of energy actually transmitted to the body is known based on the power density of the wave in air. In order to get a value based on the polarization of the wave, Ting[29] provided an equation to calculate the parallel reflection coefficient defined as:

$$R_{\parallel} = \left| \frac{-\epsilon^* \cos\theta_i + \sqrt{\epsilon^* - \sin^2\theta_i}}{\epsilon^* \cos\theta_i + \sqrt{\epsilon^* - \sin^2\theta_i}} \right| \tag{2.13}$$

where $R_{\parallel}$ is the reflection coefficient for parallel polarization, ϵ^* is the relative complex permittivity of the skin and θ_i is the angle of incidence. The equation to calculate perpendicular reflection coefficient is defined as:

$$R_{\perp} = \left| \frac{\cos\theta_i - \sqrt{\epsilon^* - \sin^2\theta_i}}{\cos\theta_i - \sqrt{\epsilon^* - \sin^2\theta_i}} \right| \tag{2.14}$$

where $R_{\perp}$ is the reflection coefficient for perpendicular polarization. See Figure 2.4 to show the difference between parallel and perpendicular orientation of the signal.

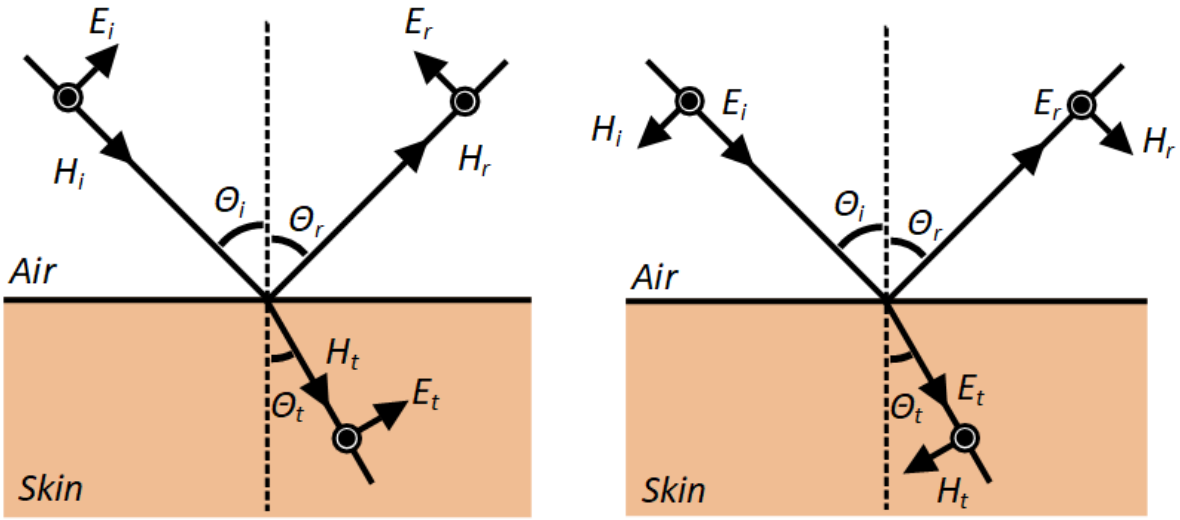

(a) Parallel polarization

(b) Perpendicular polarization

Figure 2.4: Different polarizations of the electromagnetic waves when interacting with the skin

Equations 2.13 and 2.14 can be used to compute the initial power that is absorbed by the skin. And then the subsequent incident and reflected electric fields can be calculated using the continuity of the magnetic and electric fields at each tissue layer. By setting the tissue boundaries to have the same electric field, see Equation 2.9, and magnetic field, see Equation 2.10, at those depths, z, the incident and reflected waves for each tissue can be computed. The next section will explain how to incorporate these values into the temperature increase calculation.

In order to confirm that the initial temperature increase is correct, an ADS schematic was created with ideal transmission lines as the tissues. Using a coupler, it was shown that the input power of the thermal model was correct in its calculations based on the characteristic impedances of the tissues.

2.3.3. Incorporation of Bioheat Equation and Electric Fields

Now that each tissue has been modelled as a transmission line and thus their magnetic and electric fields set equal to one another at each tissue boundary, they can be incorporated into the temperature elevation equation. In the Ting[29] study, the incident and reflected electric fields were used in the temperature elevation calculations, so it will be the focus of this section. In Ting[29], the temperature elevation calculation is defined as:

$$\theta(z) = T(z) - T_s(z) \tag{2.15}$$

where $T_s(z)$ is baseline body temperature before exposure, $T(z)$ is body temperature after exposure and $\theta(z)$ is the temperature caused only by electromagnetic radiation. The equation for calculating temperature increase by electromagnetic radiation, $\theta(z)$, is broken down into four parts and is defined as:

$$\theta(z) = \varphi(z) + \varsigma(z) + \xi(z) + \psi(z) \tag{2.16}$$

where $\varphi(z)$ is defined as:

$$\varphi(z) = C_A e^{-\sqrt{\frac{h_b}{k}}z} + C_B e^{\sqrt{\frac{h_b}{k}}z} \tag{2.17}$$

where Ca and Cb must be solved for by forcing boundary boundary conditions shown in Equations 2.21 and 2.24, h_b is heat transfer coefficient of blood, k is the thermal conductivity of the tissue and z is the distance into the tissue.

and $\varsigma(z)$ is defined as:

$$\varsigma(z) = -\frac{\sigma}{2(4\alpha^2 k - h_b)} \left|E^+\right|^2 e^{-2\alpha z} \tag{2.18}$$

where σ is the conductivity of the tissue, h_b is heat transfer coefficient of blood, α is the imaginary part of the propagation constant i.e. the phase constant, E^+ is the incident electric field, k is the thermal conductivity of the tissue and z is the distance into the tissue.

and $\xi(z)$ is defined as:

$$\xi(z) = -\frac{\sigma}{2(4\alpha^2 k - h_b)} |E^-|^2 e^{2\alpha z} \tag{2.19}$$

where σ is the conductivity of the tissue, h_b is heat transfer coefficient of blood, α is the imaginary part of the propagation constant i.e. the phase constant, E^- is the reflected electric field, k is the thermal conductivity of the tissue and z is the distance into the tissue.

ans $\psi(z)$ is defined as:

$$\psi(z) = -\frac{\sigma}{2(4\beta^2 k + h_b)} \left[u\cos 2\beta z + v\sin 2\beta z\right] \tag{2.20}$$

where σ is the conductivity of the tissue, h_b is heat transfer coefficient of blood, β is the real part of the propagation constant i.e. the attenuation constant, k is the thermal conductivity of the tissue and z is the distance into the tissue.

There are multiple variables that are necessary to calculate the temperature elevation into the tissue, but they are all constant over the change in power density: heat transfer coefficient of blood, conductivity and permittivity of tissue, propagation constant (dependent on frequency) and depth into tissue. Thus, the variables that change with power density into the tissue is the incident and reflected electric waves, denoted as E^+ and E^- respectively. The boundary Equation associated with the internal tissue, see Equation 2.24, can ignore the body temperature equation because it is the same for the boundary tissues since it is the same distance at a certain distance into the body z. But the first boundary equation associated with skin and air, see Equation 2.21, requires the body temperature equation in order to find the relation between it and air. The first boundary equation is defined as:

$$k_1 \left.\frac{\partial T(z)}{\partial z}\right|_{z=Z_0} = h(T(z_0) - T_{air}) \tag{2.21}$$

where k_1 is the thermal conductivity of the first tissue layer, h is the heat transfer coefficient from outer skin surface to air, T_{air} is the ambient air temperature and $T(z)$ is body temperature.

In the Ting[29] paper, there was no body temperature equation, but it cited Kanezaki[48] that contained a body temperature equation defined as:

$$T_n(z) = T_n(0)\cosh\sqrt{\frac{b_n}{\kappa_n}}z + T_n'(0)\frac{1}{\sqrt{b_n/\kappa_n}}\sinh\sqrt{\frac{b_n}{\kappa_n}}z + \left(T_b + \frac{A_n}{b_n}\right)\left(1 - \cosh\sqrt{\frac{b_n}{\kappa_n}}z\right) + S_n(z) \tag{2.22}$$

where $T_n(z)$ is the temperature distribution in tissue n through distance into tissue z, $T_n(0)$ is the temperature at body surface, b_n is the blood flow of the tissue n, κ_n is the thermal conductivity of the tissue, T_b is the

capillary blood temperature, A_n is the metabolic heat production, $S_n(z)$ is the temperature increase caused by plane wave exposure, and $T_n'(0)$ is the derivative of the body temperature equation at the surface layer.

Equation 2.22 requires variables dependent on the physiological response of the skin to the environment. It was decided to estimate these values for an adult in a 23C ambient environment. A 23C ambient environment estimated values come to be the worst case scenario for hot environments i.e. the skin not attempting to cool itself. It was decided that this value would remain for even the hot environments, simulating a neonate's skin which generally does not have the ability to cool itself. In order to estimate these values, they were chosen so a change in magnitude of temperature elevation at the skin surface was reflected in an equal change in magnitude of power density.

In order to estimate the body temperature equation values, each part of the body temperature equation was broken down into its corresponding heat increase parts and removed if necessary. For example, $S_{\mathrm{n}}(z)$ represents the plane wave temperature increase, so that was ignored completely. For the part of the body temperature equation based on blood temperature, see 2.23, that could be ignored for skin because at $z = 0$, cosh(0) = 1, thus setting this value to zero. That leaves the skin temperature and differential of the skin temperature to be solved for. The skin temperature was set to 35C as that is generally the value of adult skin, and so only the differential needed to be estimated. Once this was done, the body temperature equation is created.

$$\left(T_b + \frac{A_n}{b_n}\right)\left(1 - \cosh\sqrt{\frac{b_n}{\kappa_n}}z\right) \tag{2.23}$$

Using the initial temperature calculated by the body temperature equation and reflected and incident waves, the temperature at the skin and into the tissue could be found using the internal boundary equation, see Equation 2.24. Each tissue temperature elevation were calculated with these values and the boundary conditions forced. The internal boundary equation for the skin and fat and fat and muscle meeting points is defined as:

$$T(Z_i^-) = T(Z_i^+), \quad k_{i-1}\frac{\partial T(Z_i^-)}{\partial z} = k_i\frac{\partial T(Z_i^+)}{\partial z} \tag{2.24}$$

where $T(Z_i^-)$ is the temperature of the initial tissue at the boundary, $T(Z_i^+)$ is the temperature of the sequential tissue at the boundary and k_i is the thermal conductivity of tissue i. The final boundary requirement is to set the temperature elevation value to 0C at 35mm into the tissue because the assumption is the heat has completely dissipated into the tissue at this point.

Using the values calculated for the incident and reflected electric field, with forcing the different boundary equations at each tissue, the temperature elevation for each tissue can be calculated. Once this is done, the temperatures are stitched together based on the thicknesses and choice of tissue and plotted along penetration depth into the body model.

2.4. Results

The final results is a model that can take in different inputs. These include the skin structure, tissue type within the model, amount of blood perfusion, input frequency and heat transfer coefficient. Figure 2.5 contains multiple model examples. For comparison, Model 1 contains muscle as the final third layer and Model 2 contains bone. Bone has less blood perfusion than muscle and is generally considered to be a better representation of the head when it replaces muscle, which is important for 5G communications models. Most people will place the 5G devices, cell phones, near their heads for phone calls. The thermal model can also take into consideration models that contain clothing between the skin and air, which is represented in Models 3 and 4. Clothing does not reduce the output power of the electromagnetic radiation but it does trap the heat that the electromagnetic radiation causes to the skin. All models assume a normal incident propagation of the waves, also seen in Figure 2.5, meaning the angle of incidence is 0°.

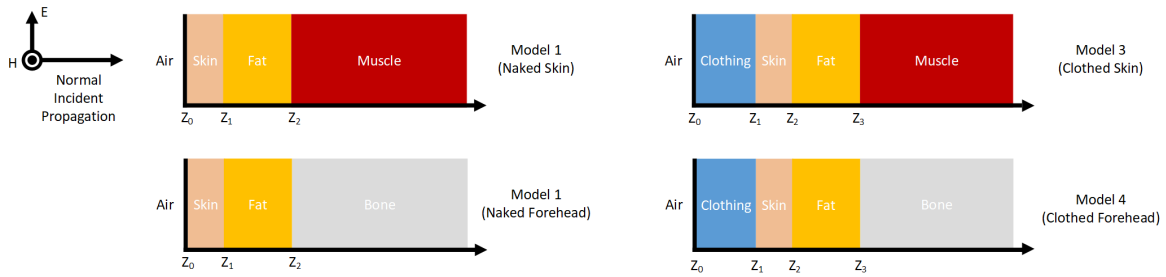

Figure 2.5: Basic model the heat increase was based off of in thermal calculations

In order to confirm the model's accuracy, the 60GHz results were calculated and shown to be the same as the Ting[29] paper, see Figure 2.6. This means a 0.2C increase in temperature for 10W/m^2 based on Model 1. Once the 60GHz model was recreated, the model was also adjusted for 80GHz because the evaluation module works at 76-81GHz and Ting[29] provided the electromagnetic properties of skin for only 40GHz, 60GHz, 80GHz and 100GHz. A change in frequency requires changing the skin conductivity and permittivity as well.

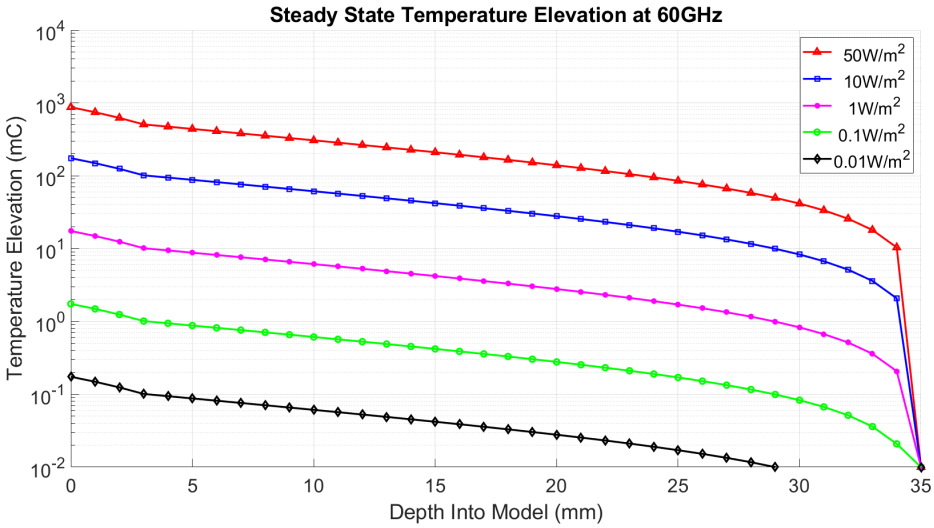

Figure 2.6: Results of the temperature elevation caused by 60GHz into the tissue at adult ambient environment

The temperature increase caused by 80GHz at an adult ambient environment was calculated to be lower than 60GHz. This seems counter intuitive since the penetration depth of the signal is much lower at 80GHz and thus the energy is more concentrated into one area, so temperature increase should be higher. In order to confirm the validity of the model, 60GHz was put into the model with 80GHz skin electromagnetic wave properties and the model showed an increase of 3mC from 60GHz to 80GHz. So, it seems the lower amount of temperature increase from 60GHz to 80GHz was due to the additional changes in electromagnetic properties of the skin. Something else to note is the penetration depth of the heat into the tissue was smaller for 80GHz, reaching 0 °C around 25mm into the model compared to 35mm for 60GHz, see Figure 2.7. This is likely due to the low penetration depth of electromagnetic waves at 80GHz.

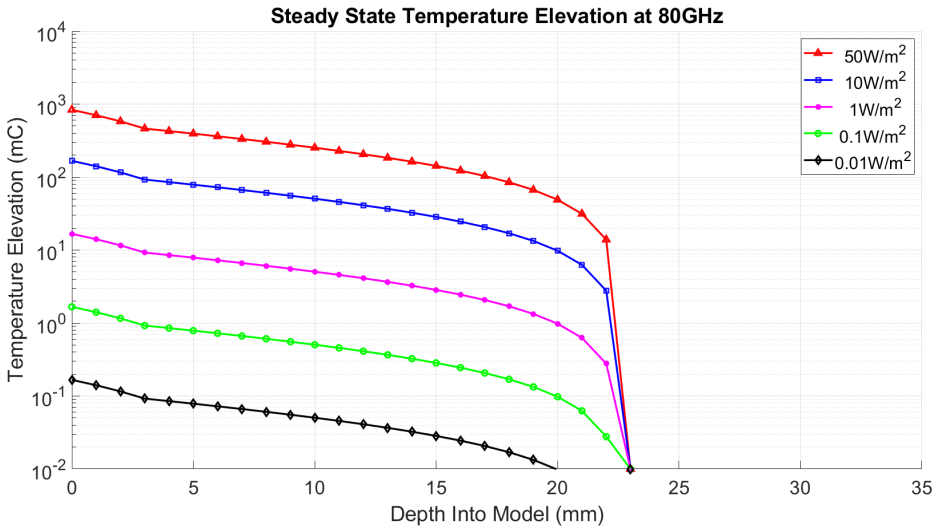

Figure 2.7: Results of the temperature elevation caused by 80GHz into the tissue at adult ambient environment

There is a limitation of the model: correct modeling of the physiological response of the skin to hot environments. Once the body is put into an environment that could cause damage to the body, there is a physiological response that changes the skin's properties to give it more of an ability to dissipate heat. The blood flow to the skin increases and the skin starts to sweat. This is to increase the heat transfer coefficient of the skin to the air, compensating for the reduction in the environment's ability to cool the skin. The body temperature equation and associated values with a cool environment were kept the same, meaning the change in physiological response of the skin to hot environments was not incorporated. As the environment becomes hotter and the skin properties continue to change, the equations representing this change become increasingly complicated. Consequently, it was decided not to recreate these changes in skin behavior for hotter environments. It's important to note that a neonate doesn't have many of the abilities adults have to regulate their temperature: sweating and increased blood perfusion if hot and shivering if cold. So, even though the model is not adjusted for different skin properties at hotter environments, the resulting temperature increases calculated could still be relatively accurate.

3

System Model and Characterization

With the environment is modelled, the system itself must be understood. In this chapter, the overview of the radar module system in the first section will be given including its operation in a NICU setting and a more in depth explanation of FMCW parameters and configuration. This will also help explain the next section that focuses on one component of the system. In order to better understand the implementation of the system in the NICU this component was simulated and characterized which the section will both describe.

3.1. System Description

A block diagram of the system is given in Figure 3.1. The radar module will be placed placed outside of the NICU incubator on the metal bars that are part of the incubator unit. The transmitter and receiver antennas will be pointed at the neonate's chest. The goal of the transmitter antennas' design will be to have distinct illumination area that is limited to the neonate's chest. The basic premise of using radar to read the heart and respiration rate is to measure the small movements of the chest. The heart and lungs push on the chest with little notice from the everyday observer, but the displacements caused by the heart and lungs are large enough that millimeter wave radar can measure by how much the chest is moved. Using the consistent frequency of the displacements of the chest the heart and lungs cause, their rates can be processed from the resulting measurement data output of the radar integrated circuit (IC).

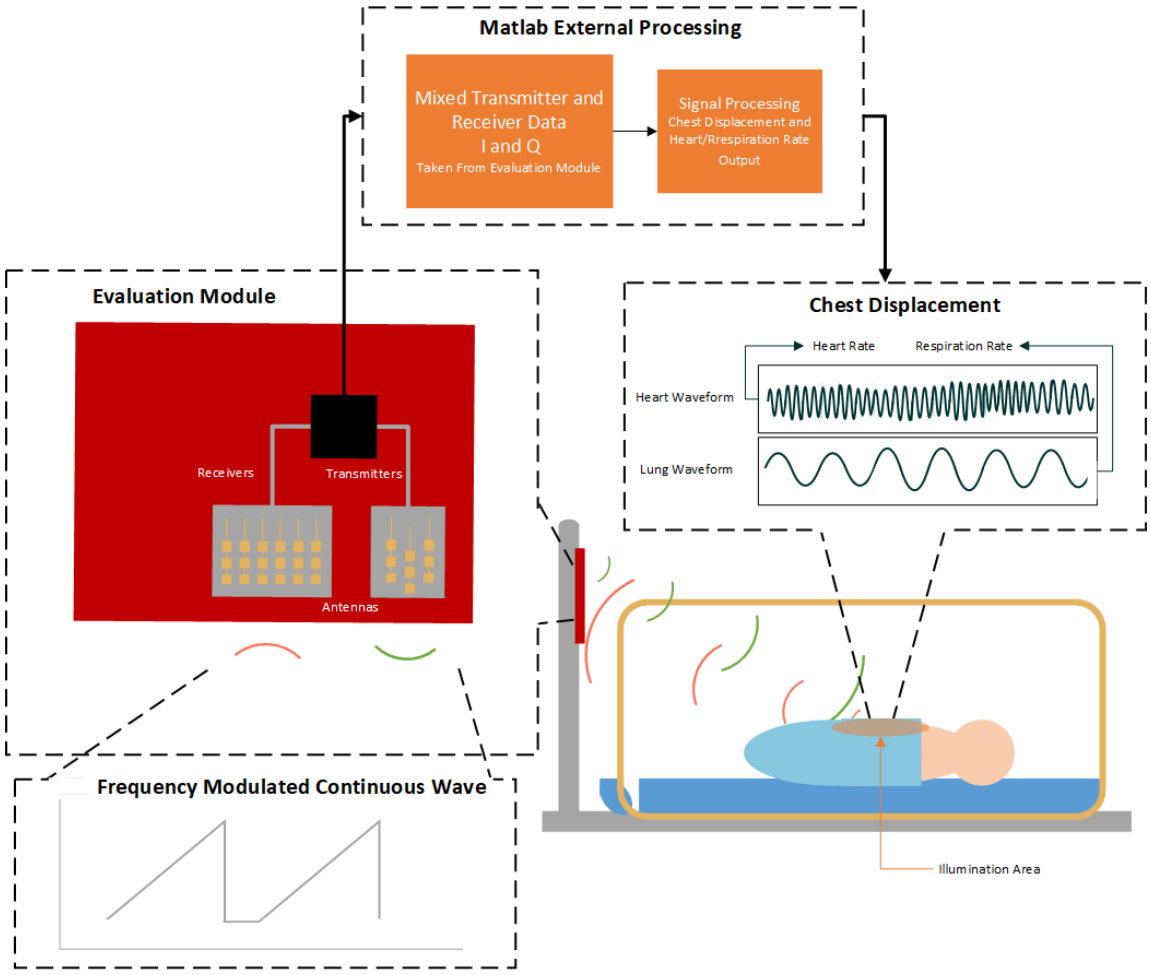

Figure 3.1: Block diagram of the millimeter wave radar system in the neonatal ICU

When the radar IC receives the FMCW radar profile it sent out, there is a time delay between what was transmitted and what was received. The radar IC mixes the receiver and transmitter data together to get the time difference, which contains where the person is located and, with some additional processing, how they are vibrating. This mixed data is first processed using an FFT. In this FFT there will be one main tone that is high above the noise floor, this is where the person is. The tone location is called the range bin. The goal of the first FFT is to find which bin in the entire FFT is the range bin. After finding the range bin, a second FFT is taken of only that bin to find what frequencies are occurring inside that bin. If the first FFT is the location FFT, then the second FFT is the vibration FFT. And the vibration that is most important to this application is the lungs and hearts' vibration. With some bandpass filtering, the frequencies can be distinguished from one another. One additional output from this signal processing is that the chest movement and heart and lung waveforms can be plotted in real time, not only the rate values of the heart and lungs.

The radar module used in the initial proof of concept will have a frequency range of 76GHz to 81GHz. Since this frequency band is mainly reserved for automotive applications, the end goal will be to have a module that uses frequencies around 60GHz, a band designated for non-automotive millimeter wave applications. Millimeter wave frequencies are electromagnetic waves within the 30GHz to 300GHz range. The name comes from the fact its wavelength is measured in millimeters. The benefits of working at these frequencies is the ability to penetrate through different materials with little attenuation. For cars, this includes rain and fog. But, in this application, this accounts for plastic and fabric. The plastic represents the incubator hood and the fabric is the blanket that sometimes covers the neonate. Given this property, the radar module can be placed outside the incubator and out of the way of doctors are nurses. Also, the small wavelength may be helpful in measuring the minuscule displacements the chest of neonate will have due to the heart and lungs. The radar module used in this application investigation has been shown to measure the heart and respiration rate of an adult, but a neonate's heart, lungs and chest are much smaller than an adults. Scaling down the technology from an adult to a neonate can be a challenge, but this may be remedied by the small wavelength of the frequencies that are used.

As previously stated, the radar uses a modulation technique called frequency modulated continuous wave (FMCW). FMCW was chosen because it has a multitude of potential configurations. With numerous options to choose from, the hope is there is potential for a configuration to be found that will give the best resolution for the application. FMCW is a modulation technique where the transmitter output isn't one frequency, continuous wave, but is multiple frequencies that are swept over time. There are many different parameters that can be changed based on this concept. Figure 3.2 contains a diagram of a chirp that shows the variables used to configure it. The slope, start frequency, idle time, ramp end time, when the analog to digital converter (ADC) starts sampling all come together to create the entire chirp cycle time. These variables decide where the stop frequency is and and how long the ADC takes samples.

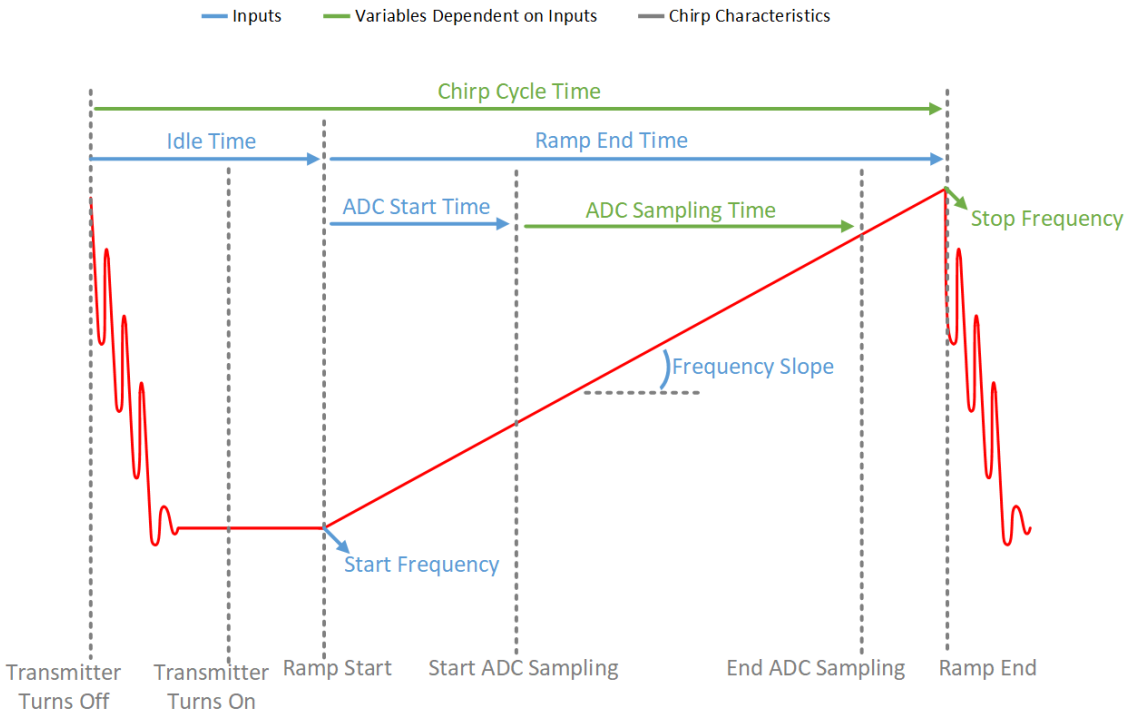

Figure 3.2: The parameters associated with configuring a chirp

Multiple chirps fit into what is called a frame, giving a sawtooth waveform of frequencies over time. A frame may have multiple different configured chirps with different slopes and start stop frequencies and duty cycles. There are a certain number of loops the frame has, which is how many times the chirps within the frame are cycled through. This contributes to the duty cycle, which is the total amount of time taken by all chirps over the frame periodicity, a variable defined by the user. There may be multiple different types of frames within what is called a profile. Table 3.1 has an example of the configurable inputs of the FMCW radar and table 3.2 has the resulting outputs. Due to the multiple chirps and frames and profiles, there are hundreds of thousands of different configurations for FMCW giving it a large amount of flexibility to be manipulated for the intended environment and application.

Table 3.1: Frequency modulated continuous wave parameters inputs

Start Frequency (GHz)	Idle Time (μs)	ADC Start Time (μs)	Ramp End Time (μs)
78	4	7	32
Frequency Slope (MHz/μs)	Sample Rate (ksps)	Number of Loops	Number of Frames
93	5500	128	10
ADC Samples		Frame Periodicity (ms)	
128		5	

Table 3.2: Frequency modulated continuous wave parameters outputs based on parameters in Table 3.1

Stop Frequency (GHz)	ADC Sampling Time (μs)	Chirp Cycle Time (μs)	Bandwidth (MHz)
81	23.3	36	2976
Total Frame Time (ms)		Duty Cycle (%)	
4.608		92.16	

The radar module that is used has three transmitters and four receivers. In the application, only one trans-

mitter will be turned on in order to reduce the output power and subsequently reduce heat production. The radar module will transmit a FMCW profile that contains the distinct frames with unique chirps that is crafted for the neonatal application. The transmitted FMCW profile will be received back by the receiver antennas with the time delay. Using an integrated development environment (IDE) made for the IC, this data can be downloaded to be processed by Matlab (MathWorks, Natick, Massachusetts, USA).

Matlab is a programming language that directly computes matrix and array mathematics. In this application, the programming language was used to take the time data output by the radar IC's IDE and add together the I and Q mixer results. Then, it takes an FFT of the time data. With the FFT, the time data is now plotted over frequency and the FFT has a certain amount of bins. An array is made of M chirps by N bins. Using the maximum search function, the bin is found that contains the person, this is called the range bin. It should be the bin with the maximum tone, outside DC, because the bin itself contains a large object, the patient, causing a substantial amount of the transmitted signal to bounce back. After finding the range bin, a vector of M chirps and range bin is extracted. Then the phase of the range bin vector is taken and unwrapped and a bandpass filter applied at the different frequencies the heart and respiration rate would normally be located. The resulting data over time is the heart waveform and lungs waveform taken from the chest. The two data sets undergo a second FFT and the maximum found for each, which contain the heart and respiration frequency of the neonate. The frequency is converted to beats and breaths per minute instead of seconds. The heart and respiration rate is averaged over a certain amount of chirps to give a better result.

Range-tracking may be applied, though it may not be necessary in this application. Neonates do not have the ability to move due to their low muscle mass, so it is unlikely they will move between bins. In this application, the bin size has been reduced drastically to make it easier to measure amplitude changes within one bin. The bin size is determined by the FMCW parameters. The final result of the system is an output of heart and respiration rate values and the lung and heart waveforms causing chest displacement.

3.2. Evaluation Module Antenna

An important component of the system is the antenna. It defines the illumination area, which in turn defines distribution of the temperature increase and the amount of scattering caused by materials and objects that do not need to be measured but are still within the environment. The antenna can be manipulated based on its design and any optical tools placed in front of it, such as a lens. But, before changing the design or adding onto it, it is important to understand the current system's antenna properties. In order to do this, the radar module's antenna was simulated and characterized, and those results are given in this section. The characterization does not only include the gain pattern but also the millimeter wave's attenuation caused by objects placed in front of it with materials similar to the ones used in the NICU.

3.2.1. Antenna Simulation

The antenna pattern is not a single point but a distribution of power over an area. This means that not only will a point on the chest be radiated but the entire neonate but with different power densities. Understanding the gain pattern distribution on the neonate leads to an understanding of the temperature increase distribution over the neonate's entire body. Knowing the gain pattern also helps with understanding the scattering effects the NICU environment will have. If the highest gain were to reach additional medical devices placed around the neonate, it can caused additional noise in the first FFT reducing the signal to noise ratio (SNR). Since an evaluation radar module will be used for proof of concept testing in the NICU, the antenna utilized by the evaluation module was recreated and modeled. The radar module uses a printed circuit board (PCB) microstrip antenna that is terminated with a patch antenna, see Figure 3.3a for a picture of the antennas on the evaluation module. There are nine antennas. The transmitters are labeled in Figure 3.3 with the remaining antennas being receiving antennas in Figure 3.3a. In Microwave CST (Dassault Systèmes Simulia Corp., Johnston, Rhode Island, United States), a software used for high frequency antenna elements, the transmitting antennas were modeled based on the measurements provided in the hardware design guide for the evaluation module, see Figure 3.3b.

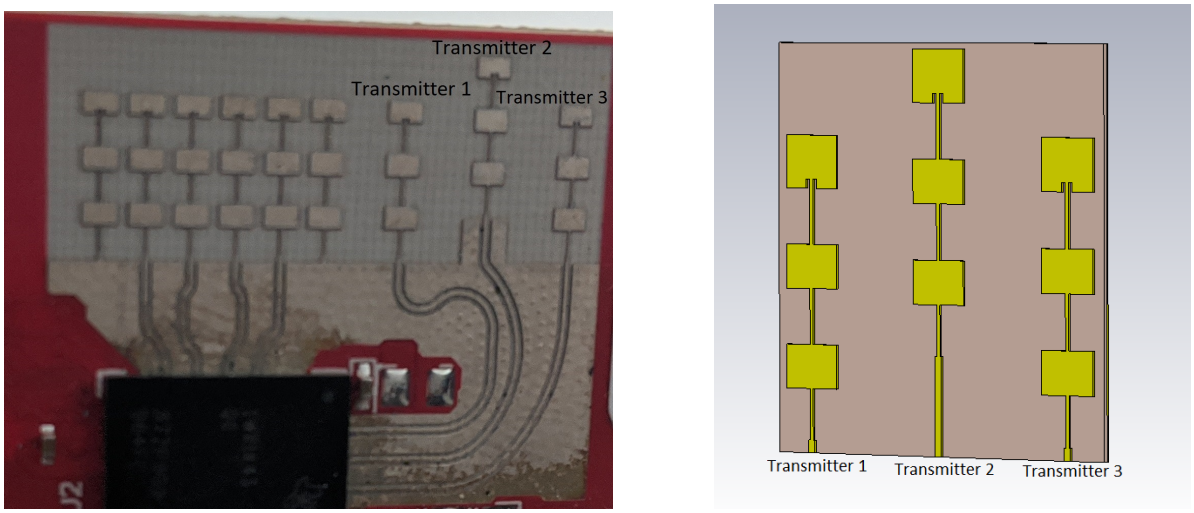

(a) IWR1443Boost Evaluation Module Transmitter Antennas

(b) Microwave CST Modeled Antennas

Figure 3.3: IWR1443Boost Evaluation Module transmitter and receiver antennas and antennas modeled in Microwave CST

Ideally the gain pattern is an even distribution of power across a certain area with very little peaks and valleys and sharp drop offs outside the area i.e. a lobe. In Microwave CST, only the transmitters were recreated for the antenna pattern simulation, and only the second transmitter gain pattern was simulated to recreate the far field radiation pattern. One transmitter was chosen for the final application in order to reduce the output power transmitted and the power usage of the radar module. Figure 3.4 shows an example of gain pattern that was produced with a three dimensional view. In Figure 3.4 the antennas are oriented in the same position as in Figure 3.3b. In order to better understand the pattern of the antenna, the two dimensional plots were also produced. These are more easily compared to the characterization results.

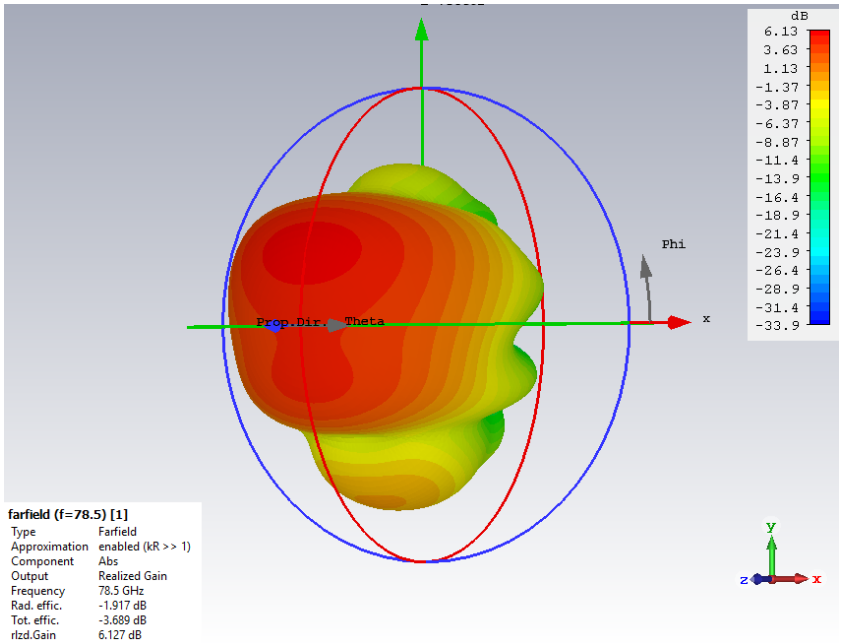

Figure 3.4: Example of 3D plot of the resulting far field gain pattern modeled using Microwave CST of transmitter 2

The resulting gain pattern shows a lobe in front of the antennas that is somewhat evenly spread, see Figure 3.5 for the gain pattern for 78.5GHz for transmitter 2 with a phi cut of 0°with sharp drop offs over theta. This is what was expected as stated previously. There are some peaks and valleys at the lobe, see Figure 3.6. Generally, it looks as though there is a single lobe that radiates from the antenna, which is ideal when trying

to measure the flat chest of the neonate.

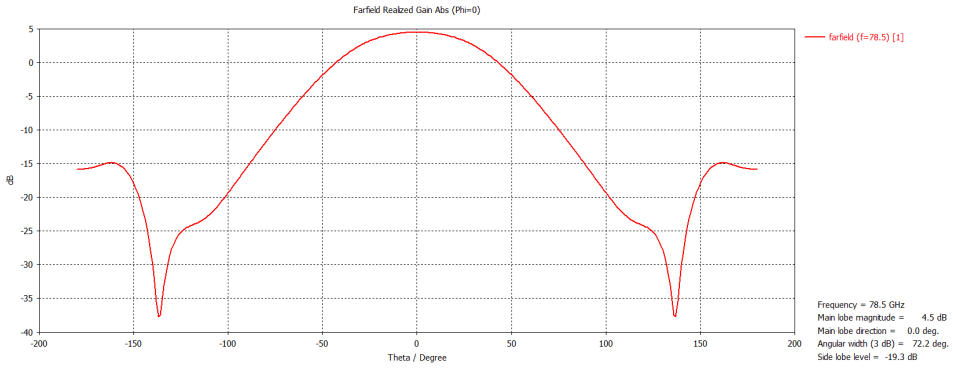

Figure 3.5: Resulting far field gain pattern modeled using Microwave CST of transmitter 2 for phi of 0°

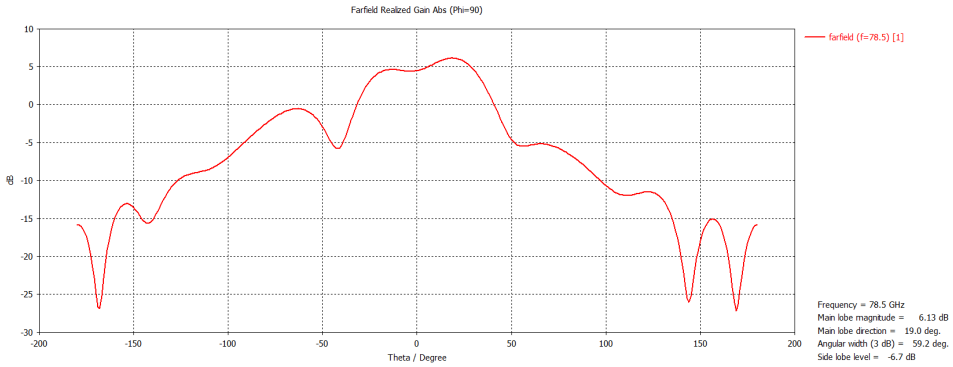

Figure 3.6: Resulting far field gain pattern modeled using Microwave CST of transmitter 2 for phi of 90°

With sharp drop offs at the lobes of the far field pattern, the radar ideally can be positioned so the flat high gain area of the lobe does not reach the face of the neonate. The power that reaches the eyes is significantly smaller than the power that reaches the chest. Now it can be confirmed that a small area is radiated with maximum output power, which will come into consideration when calculating the heat transfer coefficient. Optics may need to be used in the future to better steer the gain pattern and reduce its lobe size even further, which can also be simulated. But first, the simulations results need to be compared against the characterization results and confirmed to be accurate if they are to be used in future antenna modifications.

3.2.2. Antenna Characterization

Due to the structure of the antenna of the radar module, measuring its far field radiation pattern is difficult. Consequently, a set-up was created based on the paper Alonso et. al [49]. A near field measurement was done using two antennas and the near field data was used to create the far field gain pattern. The goal was to get a relative understanding of the radiation pattern and compare it to the simulation results, so the absolute output power was not measured.

Two Antenna Set-Up

It is difficult to measure the far field radiation pattern of embedded PCB antennas[49] because materials surrounding the embedded antenna can affect the far field radiation pattern. These materials include the radar module PCB and the radar IC. In order to remedy this, a near field measurement can be done with the receiving antenna as close to the transmitting antennas as possible. This reduces the scattering effect the surrounding materials have on the measured gain pattern and then the near field data can be used to create a far field gain pattern. The addition of a second receiving antenna can be used to deembedd the phase. This antenna is placed at a 90° orientation to the main receiving antenna.

In the system used to characterize the PCB antenna of the evaluation module, shown in a block diagram in Figure 3.7, a 4 port vector network analyzer (VNA) was used, a PNA-X from Keysight (Santa Rosa, California, United States). Both receiving antennas were WR10 and were connected to mixers that down converted the output frequency of the transmitter antenna to a frequency within the VNA range and output the value to the PNA-X. The output power was measured by the PNA-X as well as the phase and the information was used by a Matlab script to plot the far field radiation pattern. In order to move the receiving antenna in an x-y grid and get it close enough to be in the far-field of the PCB antenna, it was attached to the computer numerical control (CNC) machine arm. The arm of the CNC machine is able to move in x, y, and z directions.

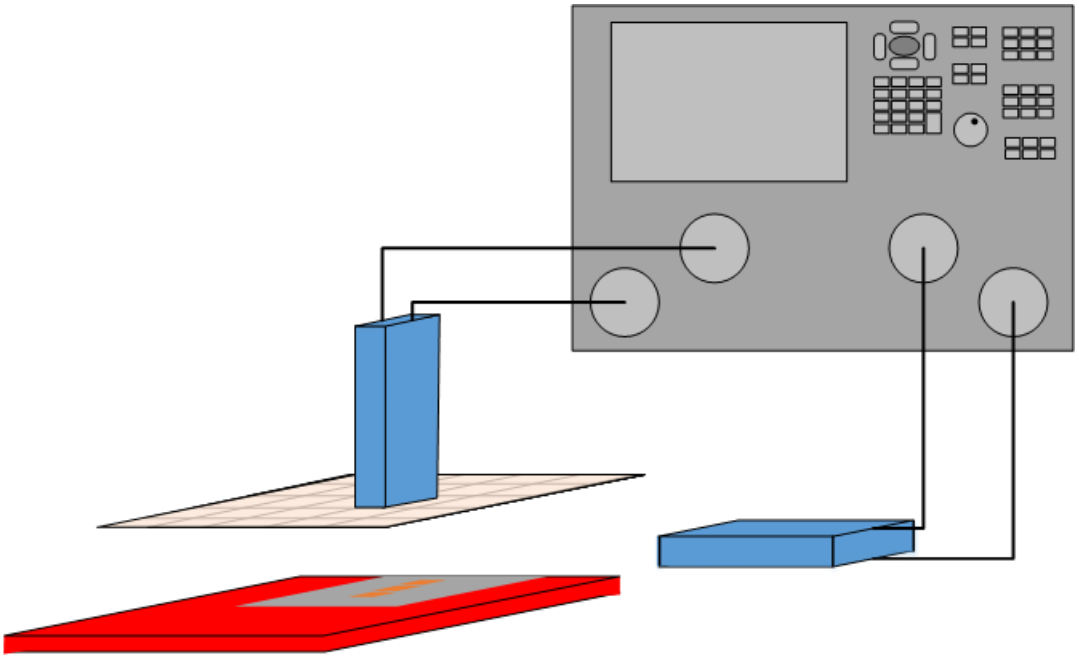

Figure 3.7: Set-up with two antennas and a vector network analyzer

An Agilent E3611A DC power supply was used to provide 5 volts and up to 1.5 amps to the board. The board can take up to 2 amps in current, but, in order to bring down power consumption and thus heat production, only one receiver, Receiver 1, and one transmitter, Transmitter 2, were turned on. This brought down the amperage to 500mA for one transmitter measured and 600mA if two transmitters were measured. The radar module was placed on the bed of the CNC machine by a 3D printed holder and surrounded by absorbent materials in order to reduce scattering. Due to the stacking of the evaluation modules: one used to connect to the millimeter wave IC (IWR1443) and the other used to connect the IWR1443 to the PC (MMWAVE-DEVPACK), there needed to be a holder built that could keep both devices in place and attached to one another. Also, to keep the jumper pins from touching the metal surface of the CNC bed.

In order to connect with the EVM and control the number of transmitters and frequency, the software that comes with the EVM was used. This included mmWave Studio, Uniflash, Matlab Runtime Engine and the EVM's FTDI drivers. Once those were installed, the board can connect to the PC. From there, additional code was used that automated the CNC machine x-y grid connection and the data gathered from the PNA-X. The device was put into continuous wave instead of FMCW mode using the evaluation module's Radar Studio installed on the PC. The PNA-X does not need a large amount of time to measure the output power and can be controlled by Matlab along with the CNC machine, so a sweep of 20mm by 20mm with 0.25mm steps was done using the Matlab GUI provided by Alonso et. al[49]. The given code allows for the user to decide where to set the corner of the grid that will be measured and the size and shape of the x-y grid.

In order to synchronize the network analyzer and the board, the output clock of the evaluation module, 40MHz, was fed into a signal generator with the ability to lock onto a large frequency range of reference signals. Then, the signal generator output a 10MHz signal to the VNA after locking onto the 40MHz crystal

output of the evaluation module. In this way, the PNA-X could be synced with the evaluation board, reducing testing time because the tone should no longer move within a small frequency range.

3.2.3. Simulation and Characterization Comparison

The measurement area was a 20 mm by 20 mm grid with the center of the grid being the middle of the second transmitter of the PCB antenna. The CNC machine was moved in 0.25mm steps in x and y directions and kept at a constant distance of 1cm away from the antenna. Figure 3.8 has an example of a measurement done at 76GHz plotted as a near field two dimensional output. The power is not smooth, it has multiple small peaks and valleys shown as light and dark blue dots. This is suspected to be due to the clock signal from the evaluation module. Though the signal generator did not show any errors of the evaluation module output 40MHz signal from the crystal being unlocked, the power signal measured by the PNA-X was not stable. This could imply the crystal of the evaluation module was not strong enough to drive the sync signal to the signal generator and subsequent VNA.

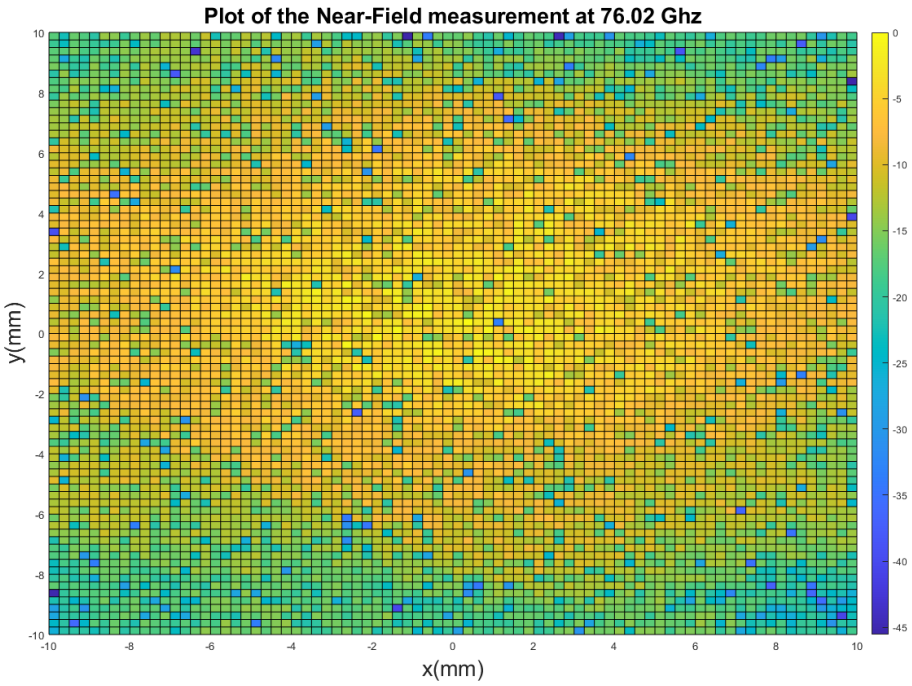

Figure 3.8: The measured gain pattern of the PCB antenna using two antenna near field to far field technique in 2D map

The VNA only looks at one frequency for power measurements instead of finding the frequency that has the maximum power and recording that power value. If the maximum power does not remain in the same frequency location throughout the entire measurement, but instead moves around throughout a small frequency window, then there are points where lower output powers would be measured than the actual output power. The results are points that have a smaller output power than the actual maximum creating this small valleys in Figure 3.8. An unsynchronized signal must be taken into consideration when comparing the resulting plots and will require future signal processing to smooth out the results to make it comparison of the the simulation and characterization results more straightforward.

Simulation and characterization results were plotted together over theta in two dimensional plots of the far field gain pattern for phi cuts of 0°, see Figure 3.9, and 90°, see Figure 3.10, at 76GHz. Due to the measurement set up, the maximum theta that could be measured was calculated to be 40°, so the resulting values above 40° and below -40° are grayed out since they are not viable. The expected output of the characterization plot is for the lobe to be flat at a phi cut of 0°, but the characterization results do not have smooth behavior. Another discrepancy, seen in Figure 3.10, the expected drop in output power at the lobes should occur around -50°and

60°theta, but the characterization results show drop offs at much smaller theta values.

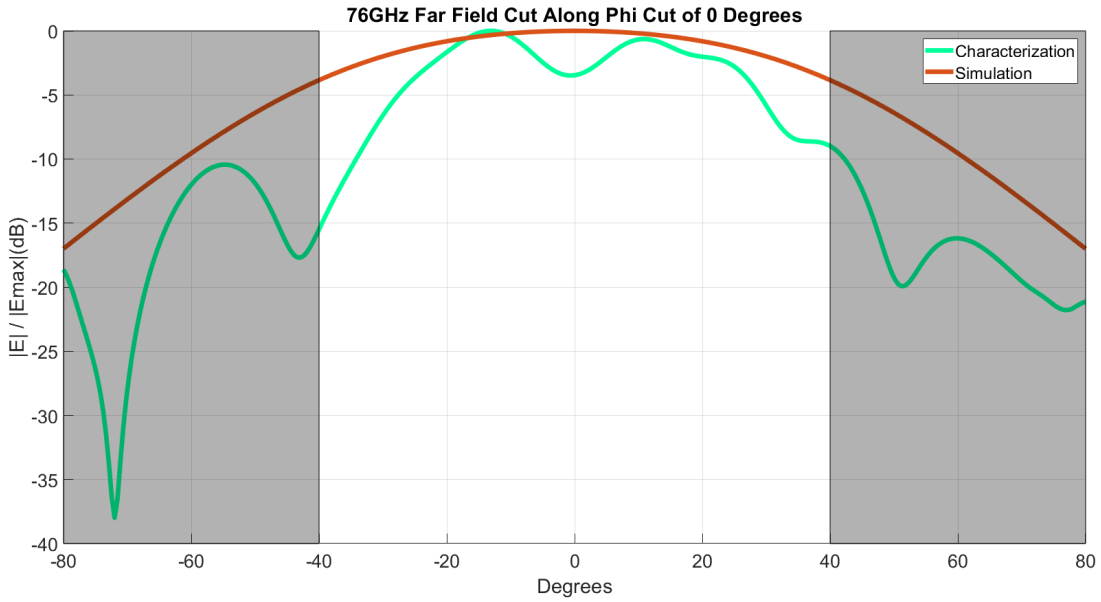

Figure 3.9: Measured far field gain of antenna at 76GHz with phi cut of 0°

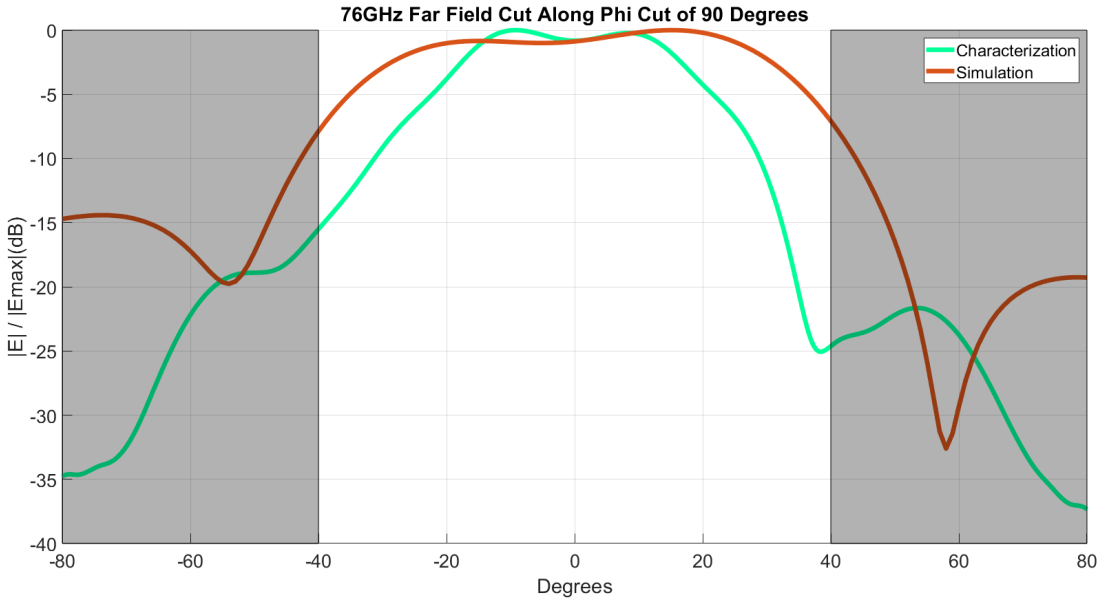

Figure 3.10: Measured far field gain of antenna at 76GHz with phi cut of 90°

The antenna was designed for multiple applications, so it does not have a high directivity. The measurement set up was not designed to measure a non-directive antenna, so it is difficult to get consistent results with the low directivity antenna used by the radar module. This may by a partial cause for the discrepency between the characterization and simulation results. As previously stated, the 40MHz clock intended to synchronize the evaluation module to the VNA was not stable or unable to drive the VNA, meaning the phase and amplitude were not locked most likely negatively affecting the measurements as well. Additional programming could be added to search for the peak output power to remedy the synchronization issue, but these results also point to the need for the antenna design to be taken into more consideration. This could come to designing a new antenna or adding optics to the current radar module antenna to directly illuminate the neonate's chest. The gain pattern affects the location and spread of the temperature increase of the electromagnetic waves on the

neonate and the signal to noise ratio of the data output, so the antenna is an important component in more ways than one.

3.3. Obstructive Materials Measurements

There will by materials placed in between the radar module and the neonate due to the radar module's location outside the incubator. Though the materials are unlikely to cause a significant detriment to power, characterization was done of these materials to show the potential attenuation effects they may have. Two materials that would obstruct the line of sight of the radar module were identified: the plastic of the NICU incubator hood and the fabric of the blanket that sometimes covers the neonate. In order to measure the material's affect on power, the relative power was calculated from the absolute powers measured with and without materials obstructing the line of sight. The materials were oriented in two ways: perpendicular and at a 45° angle to the antenna plane. The second orientation was to mimic the curved hood of the NICU incubator.

3.3.1. Measurement Set-Up

The measurement set-up used a power meter to measure the output power with and without materials obstructing the radar module's line of sight. The measurements were done with a continuous wave output from 76GHz to 81GHz in 1GHz steps. The power meter cannot measure FMCW output power and the continuous wave can be more easily correlated to the thermal model, which also depends on a continuous wave signal. The power meter was placed around 21cm away from the radar module in order to be able to fit the incubator plastic and blanket while keeping the resulting output power signal out of the power meter's noise floor. Since many items that were around the set-up were placed in the far field, the absorbent materials were left only for the desk the radar module was placed on. Absorbent materials were placed on the desk in between the power meter and the radar module, see Figure 3.11. The power meter was set up to be directly in line with the second transmitter to get as close to the highest output power as possible. Since there is not a guarantee the highest output power was measured, the relative output power was calculated of the materials output power in respect to no obstructive materials output power.

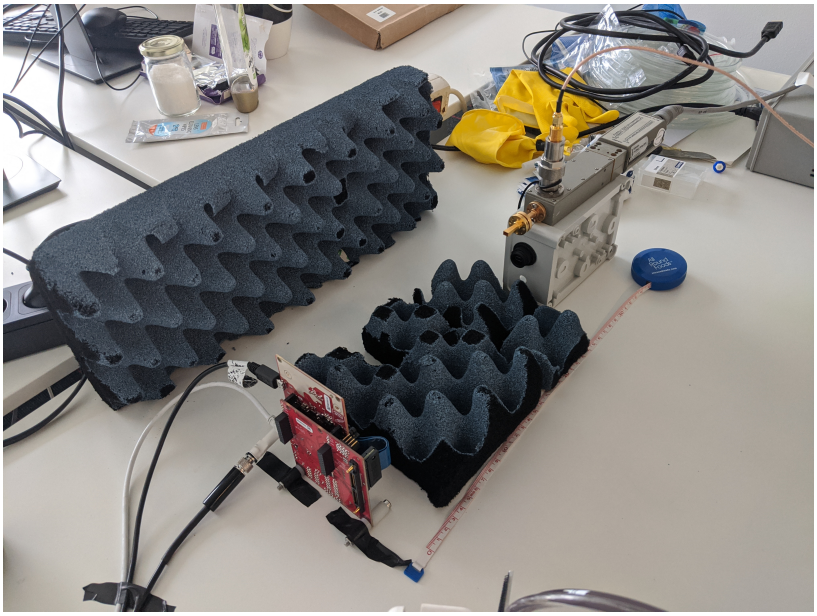

Figure 3.11: Set-up without any blocking materials to measure initial power of the antenna

An incubator door was used in replacement of the hood because of its smaller size. It more easily fit into the measurement set-up, see Figure 3.12a. The blanket was hung on a clothes line put in front of the radar module, see Figure 3.12b. The goal was to create only one layer of fabric between the power meter and radar module instead of multiple layers caused by the blanket being folded on itself. One note, it is unlikely that

only the blanket will be used when monitoring the neonate since the final application will be with a NICU incubator, but confirming the fabric also has little effect on its own may be helpful in future applications. The incubator door and blanket were also combined together, see Figure 3.12c. The blanket was placed directly behind the incubator door in order to keep the output power from the radar module higher than the power meter noise floor. The configuration of the incubator plastic and blanket in Figure 3.12c is not realistic, but it would yield the worst case scenario which can help determine if a more realistic scenario is safe.

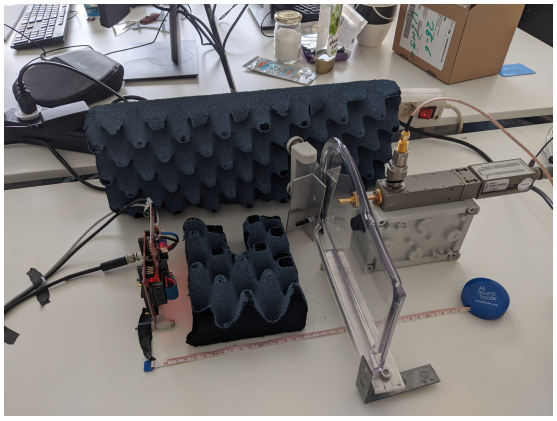

(a) Incubator Door

(b) Blanket

(c) Blanket and Incubator Door

Figure 3.12: Set-up with different materials used in real life application blocking the power meter antenna determine change in output power

One frequency was measured at a time with and without materials. The power meter was calibrated at every frequency without any blocking materials. Then, the output power of the radar module was measured. Next, the incubator door was placed in front of the power meter and the power measured, then the blanket, then both. The process was restarted for the next frequency and repeated, so there was no change in the power meter calibration between frequencies and the transmitter was constantly transmitting at one frequency as to not change the radar settings while testing different materials.

An assembly was put together that could move the incubator door at different angles, see Figure 3.13, so the additional measurements at 45° could be done.

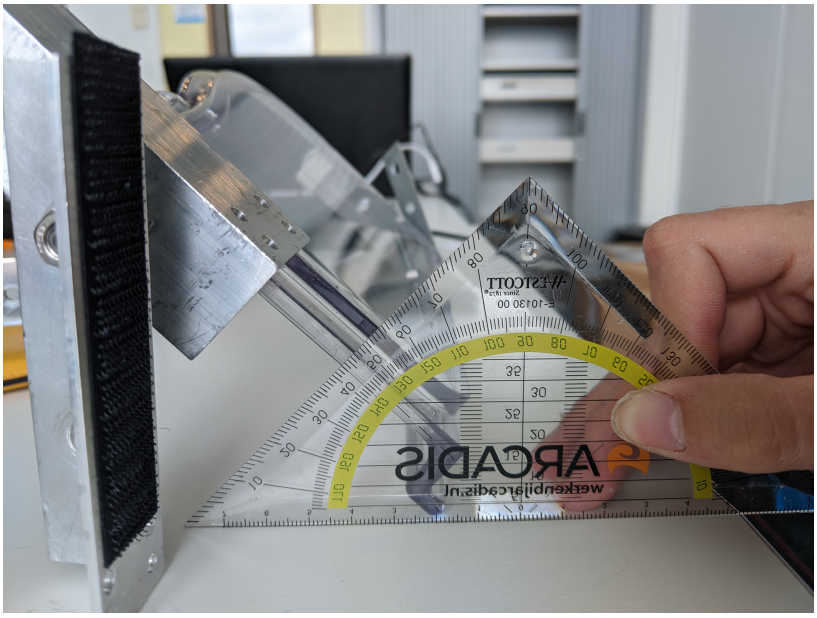

Figure 3.13: Incubator door set-up so that it is oriented at 45°

The blanket was placed at 45° angle along with the incubator door to remain consistent with the 0° orientation with the blanket directly behind the door, see Figure 3.14.

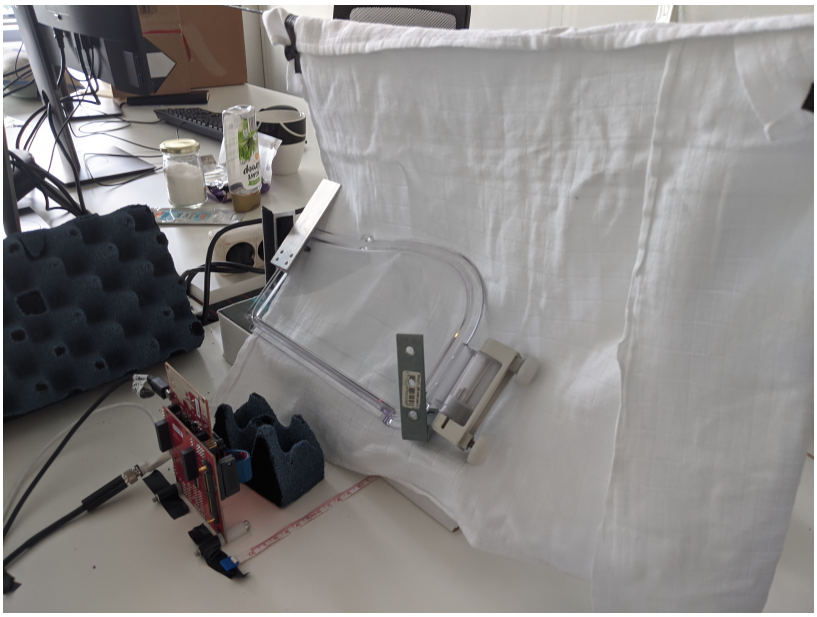

Figure 3.14: Incubator door and blanket with set-up so that it is oriented at 45°

3.3.2. Test Plan and Results

As expected the plastic and fabric had little effect on output power. At least 90% of the power was maintained, see Table 3.3 for the results at perpendicular orientation. Two tests were run for each iteration in order to average out any inconsistencies. From the results, it can be seen the blanket had little to no effect while the incubator door caused a slight detriment to the output power, about a loss of 5%. Also, it looks as though a 45° orientation, see Table 3.4, actually caused less of a detriment to the signal than a 0° orientation. Consequently, the conclusion is the materials will have little effect except for the blanket because it will trap heat caused by the millimeter wave radar.

Table 3.3: Orientation of incubator door and blanket at 0°

Input Frequency (GHz)	Relative Output Power (%)		
	Incubator Door	Blanket	Incubator Door + Blanket
76	97.32	97.45	87.29
77	95.30	97.62	91.50
78	94.16	96.93	93.43
79	97.03	98.81	93.78
80	93.37	96.32	91.96
81	98.13	98.30	96.16

Table 3.4: Orientation of incubator door and blanket at 45°

Input Frequency (GHz)	Relative Output Power (%)		
	Incubator Door	Blanket	Incubator Door + Blanket
76	96.55	98.23	97.23
77	97.12	98.96	95.73
78	96.79	98.41	98.80
79	97.55	99.21	99.78
80	95.12	98.63	98.76
81	94.09	98.04	95.92

As it can be seen, the 45° orientation of the incubator hood had higher relative power results than the 0° orientation of the incubator plastic. This could potentially point to the ability of the plastic incubator hood to work as a lens that concentrates the output power causing less loss than expected. Though having less loss is not an issue, if the output power is higher and the radiation pattern different than expected with an incubator hood placed between the radar module and the neonate, the most likely application case, then more research needs to be done onto the potential lens properties of the incubator plastic could have on electromagnetic waves.

4

System and Environment Validation

The system described in Chapter 3 is influenced by the environment and needs to be validated to work within it. In this chapter the system's operation within the NICU environment is addressed by the signal processing and FMCW configuration validation to read small amplitude changes of a neonate's chest. The need for validation also holds in the reverse. The environment is influenced by the system operation, which was modelled with the thermal model described in Chapter 2. The thermal model must be validated to guide the final application of the system. Both validation scenarios are addressed in their own sections. The goal of this chapter is the comprehension of how the system and environment interact, so that the radar module may be successfully operated in a NICU clinical setting.

4.1. Thermal Model

In this section, the thermal model is addressed. The set-up will be described and an overview of the results of the measurements will be given with an analysis and the impact this has on the thermal model explained in Chapter 2. In order to validate the thermal model, an infrared (IR) camera (VarioCam HD, InfraTec GmbH, Dresden, Germany) was used. Since the thermal model was done with continuous wave assumptions, the evaluation module was also set to continuous wave output in the near field and far field. Continuous wave and near field implementation is a non-realistic scenario, but it brings the validation set up as close to the model as possible giving a better ability to correlate the results. The module was put outside and inside the incubator, which was used to create a hot environment similar to a neonate's. A piece of bovine tissue was used to represent a piece of tissue that did not have blood perfusion, simulating sepsis, and an adult arm was used to mimic the model's assumed scenario, an ideal scenario. Both were given enough time to reach the equilibrium temperature inside the incubator. In order to place the meat steak and adult arm within the near field, the radar module was put inside the incubator, which will not occur in the final application of the system.

4.1.1. Infrared Camera Set-Up

The set-up used an IR camera that, when pointed at an object, could measure the temperature change over time. The IR camera was placed behind the evaluation module for outside the incubator measurements and next to the evaluation module pointing through an incubator door opening to be able to measure hot environment measurements. Plastic reflects infrared light, so the incubator door had to be open to so the camera could view the change in temperature of the device under test. The incubator is built to adjust for any changes in temperature, so, giving it enough time to reach equilibrium, the temperature remained at 35C needed to recreate the hot environment. The camera measures temperature over time by using different areas that are defined within the user interface by the user. The location can be circles or ellipses or points that the thermal camera must measure. If it is a shape, such as a circle or ellipse, the average temperature and maximum and minimum temperature are recorded. If it is a point, only the point temperature is measured. In the section, for each plotted temperature over time result, a figure containing a picture of the locations that were being measured by the thermal camera are shown. For example, in order to show the localized heating of the radar module, different areas were measured that were considered outside the radar antenna's gain pattern and

those within. It can be seen some areas have a temperature increase and others do not.

The radar module was set at 77GHz continuous wave output and the near field and far field were distinguished by changing the distance the radar module was from the heated area. The radar module output power stayed at maximum, so the only change in power density would come from the distance change. The humidity of the incubator was set to 20% and the temperature was set to 35C. After beginning temperature recording, a few seconds of equilibrium temperature were recorded then the radar module was turned on. This can be seen in the plots as there is a delay before the temperature increases. The arm inside the incubator was there for an hour to stabilize its temperature with the incubator temperature. The piece of meat was placed in the incubator for 15 hours, but it stayed at a maximum of 28C after 15 hours of heating. Due to this temperature disparity and in order to confirm any temperature increase caused by the radar module wasn't the meat tissue heating to 35C, the meat steak was monitored without any heating done to it by the radar module to show the stability of the temperature at 28C within the 35C incubator.

Near field and far field were measured inside and outside the incubator. First, outside the incubator was measured. That means the adult arm was placed within the near field and far field, about 16cm away, from the radar module without any additional heating components. So, the ambient temperature was kept at 23C and the heat transfer coefficient was relatively high as the humidity was low in the room as well. Once initial temperature calculations were made, the arm and meat were placed inside the incubator with an opening for the thermal camera, see Figure 4.1. The evaluation module was used as the signal generator, since it was the only device that was available to transmit in the tens of gigahertz range and fit within the incubator for near field measurements.

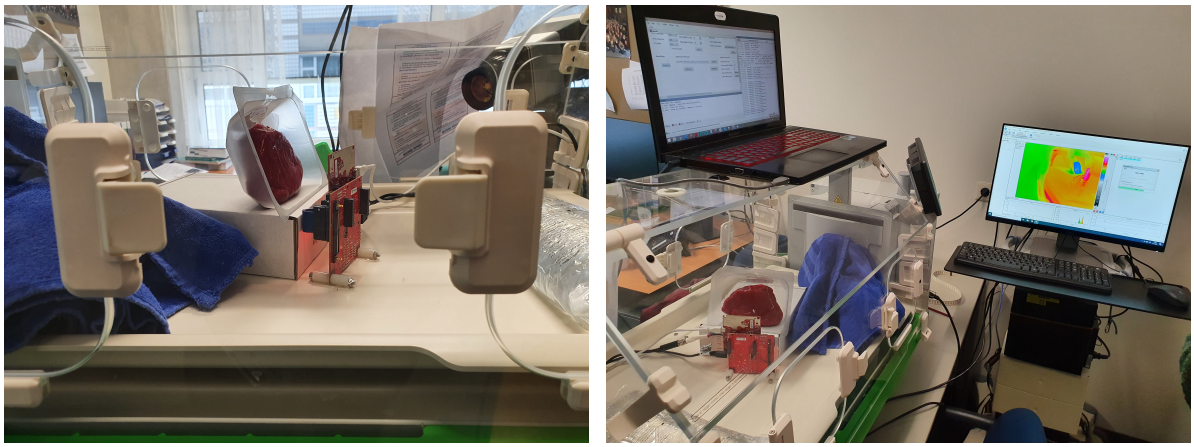

(a) View of set-up with thermal camera

(b) View of setup with thermal camera user interface

Figure 4.1: Infrared camera set-up for validation of heat increase inside neonatal ICU incubator

In Figure 4.1, the arm and meat steak were placed on a box to reach the height of the transmitter antennas which were at the upper end of the evaluation module. The Millimeter Wave Studio software used to control the output of the radar module was connected to the radar module using the laptop seen in Figure 4.1b with cable connections that ran through the incubator door that was opened for the IR camera. The user interface used by the thermal camera can also be seen in Figure 4.1b where the user defines the areas that need to be measured by the thermal camera. The meat steak was kept in its box, so that it could remain upright during heating, see Figure 4.1a. An attempt was made to increase the humidity of the incubator in order to show that the evaporation heat loss of the meat steak was the cause of the stability at 28C of the meat tissue. But the incubator could not maintain humidity above 50% without additional help, i.e. placing cups of water inside the incubator.

4.1.2. Interpretation of Validation Results

In this section, the validation measurements are given. There were a few conclusions that were made based on the results, and they are explained accordingly along with their influence on the thermal model and the understanding of the system operation within the NICU environment. When using the IR camera, an area

of measurement must be defined. In order to get measurements over time of temperature, the user must highlight an area or point that is the focus of the measurement. If it is an area, the average, minimum and maximum area recorded and, if it is a point, only the temperature is measured.

Heat Transfer Coefficient Recalculation

In Figure 4.2, the near field measurement of an adult arm inside an incubator set up is shown with the different areas that were measured by the thermal camera. The set up in Figure 4.2 is intended to recreate the parameters of the thermal model with the addition of a hot environment. So, the blood perfusion is the same, the power density remains around the same, the output is continuous wave and the radar module is in the near field. Overall, the only variable that should change is the heat transfer coefficient of the environment. The different locations of the circles and ellipses in the set up are dependent on where the radar module is radiating at. Circle 1 and Ellipse 5 are intended to be within the area of illumination and Circle 2 and Ellipse 4 are intended to be outside the area of illumination. The goal was to show the temperature increase of a near field measurement but also to show the radar module's localized heating.

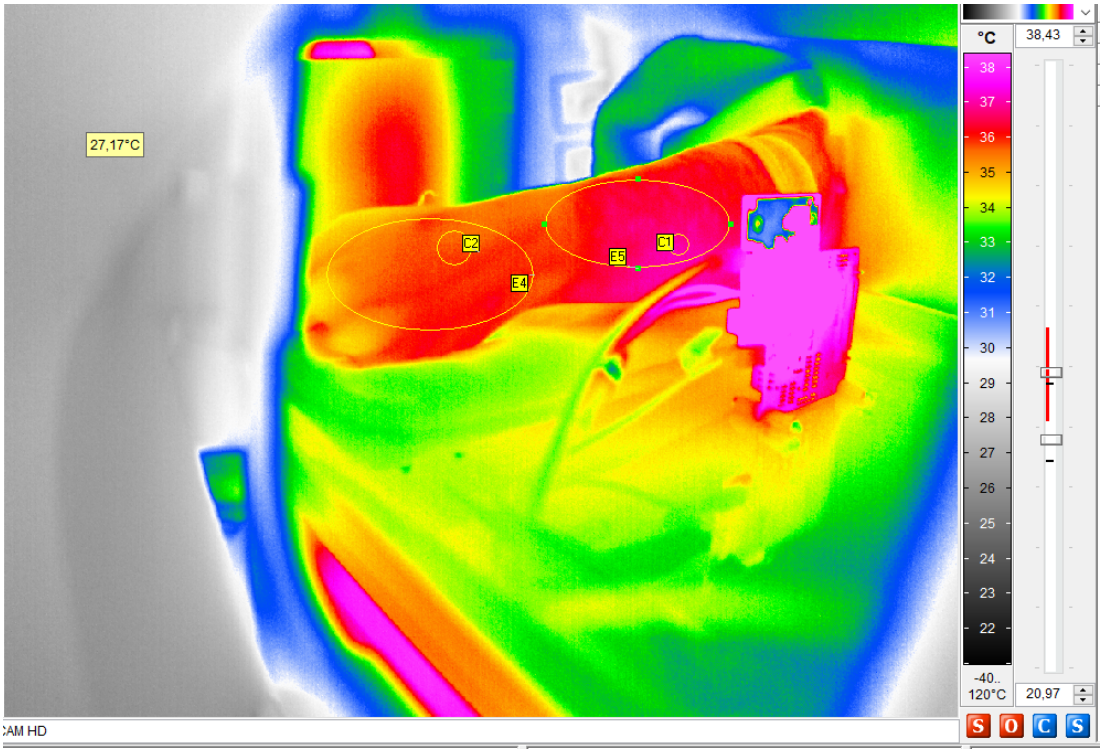

Figure 4.2: Areas measured by the thermal camera for near field measurement with adult arm inside incubator at 35C, 20% humidity

Figure 4.3 contains the plots of the temperature increase in the area of illumination for Circle 1 labelled in 4.2. The results in Figure 4.3 show Circle 1 an increase in temperature of 340mC was measured. The temperature increase and subsequent stabilization after 20 seconds can easily be seen in the average and maximum and minimum temperature measurements. The 340mC comes from the average temperature measured before the radar module is turned on subtracted from the average temperature measured after the radar module is turned on. Circle 1 was placed on the hottest section of Ellipse 5, see Figure 4.2. Ellipse 5 was defined to represent the area in front of the radar module, which theoretically would be the only heated area. Ellipse 5, see Figure 4.4, has large deviations throughout the minimum temperature increase, so it was taken out of the measurement plot and only the maximum temperature recorded in Ellipse 5 was analyzed. The minimum temperature increase had erratic behavior because the arm moved inside and outside the area of the ellipse. Ellipse 5 records a 360mC temperature increase for its maximum temperature recordings, which stabilizes after 25 seconds similar to Circle 1.

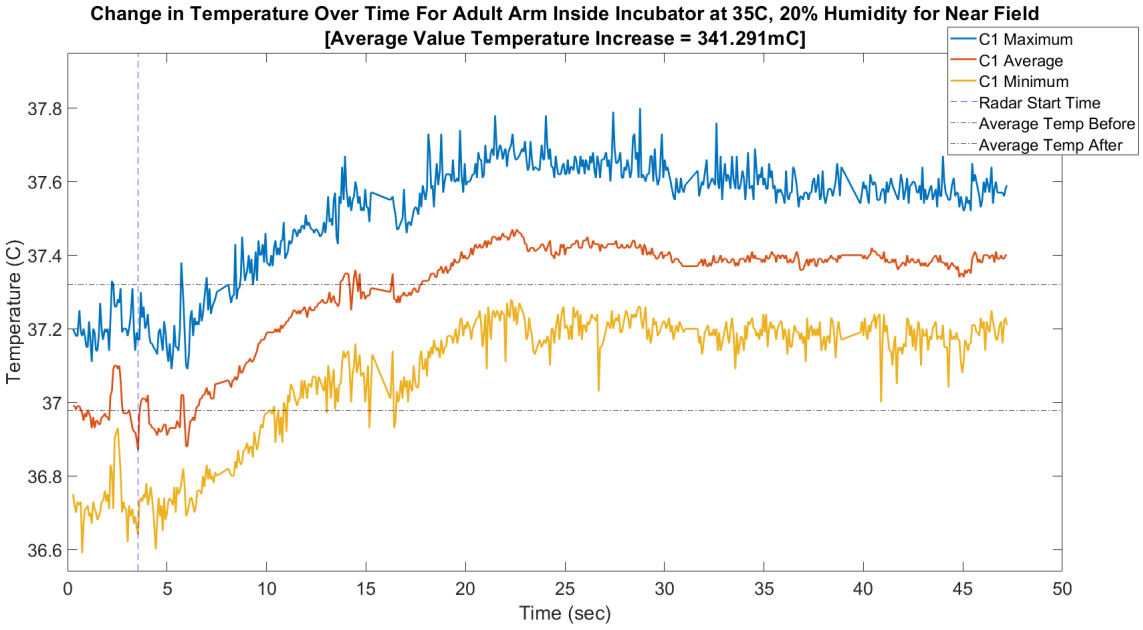

Figure 4.3: Results for near field measurements inside incubator with adult arm inside illumination area for Circle 1

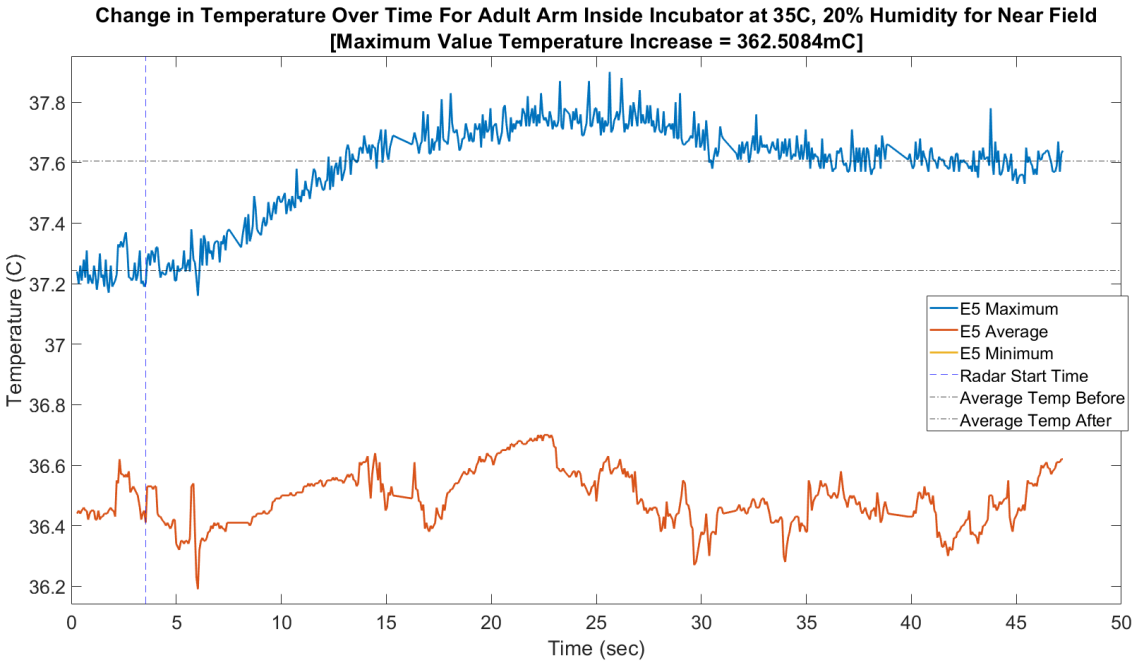

Figure 4.4: Results for near field measurements inside incubator with adult arm inside illumination area for Ellipse 5

Figures 4.5 and 4.6 contain plots of temperature measurement areas outside the area of illumination. Both Circle 2, see Figure 4.5, and Ellipse 4, see Figure 4.6, don't show a large temperature change, but a small temperature increase. Ellipse 4 records an 80mC temperature increase compared to the Ellipse 5 temperature increase of 360mC. Ellipse 4 has a slow temperature increase that seems to start after the temperature increase in Circle 1 and Ellipse 5 have stabilized. Circle 2 has a temperature increase that occurs quite rapidly towards the end of the measurement. It is difficult to understand what caused this sudden change in Circle 2 and gradual change in Ellipse 4 considering both occur after the area of illumination temperature change has stabilized.

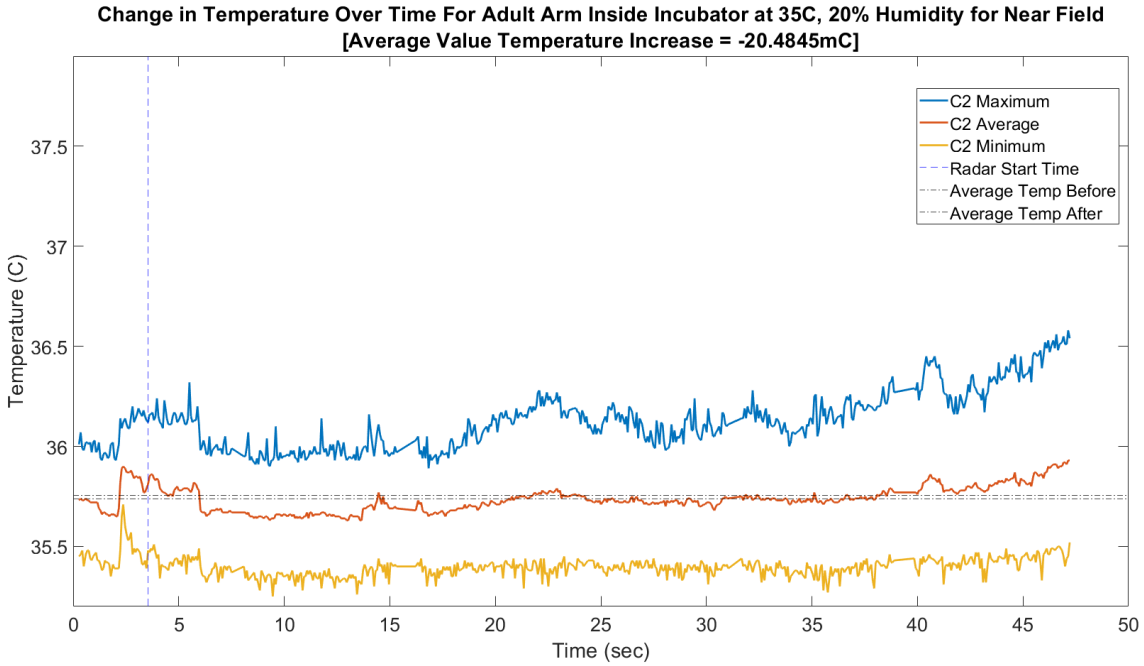

Figure 4.5: Results for near field measurements inside incubator with adult arm outside illumination area for Circle 2

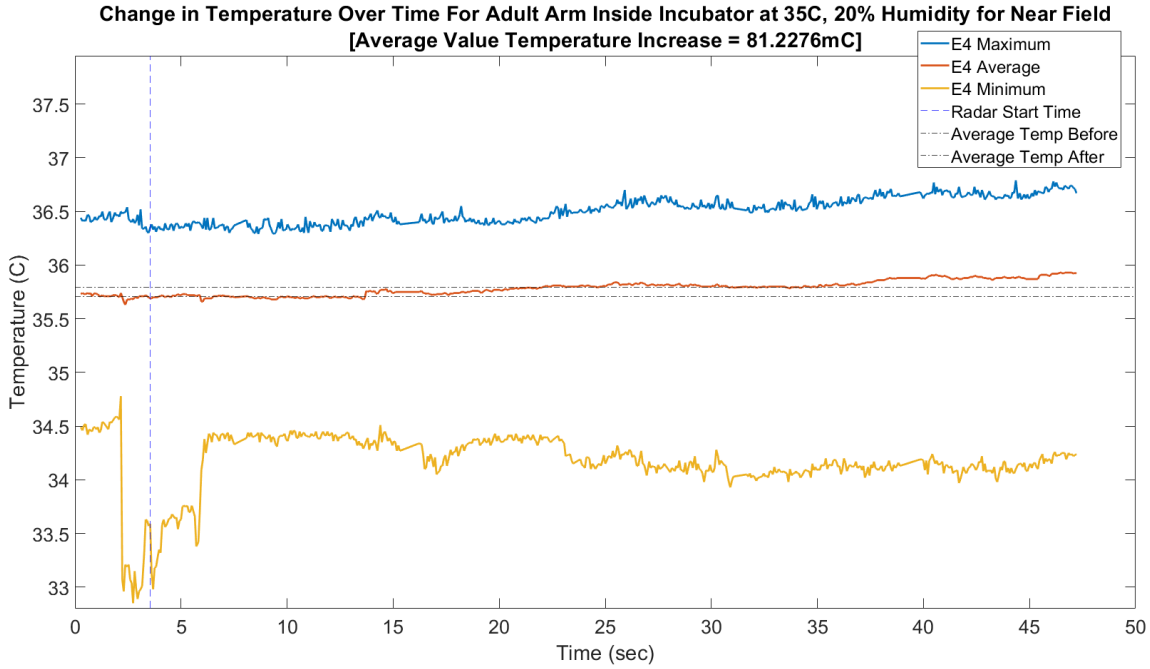

Figure 4.6: Results for near field measurements inside incubator with adult arm outside illumination area for Ellipse 4

The temperature increase stabilized at around 360mC instead of the 1.5C that was calculated for a 35C, 20% relative humidity environment. So, an investigation went into what would cause this discrepancy. The calculation of the heat transfer coefficient was the starting point seeing as it is what incorporates the hot environment. It was seen that if the heat transfer coefficient went from 1.2W/m^{2}C, the original heat transfer coefficient calculation, to 6W/m^{2}C the temperature increase recalculated to around 400mC. Seeing as the larger heat transfer coefficient led to a temperature increase much closer to measured, the next step was to understand how the calculation of the heat transfer coefficient would create such a disparity.

The area the combined heat transfer coefficient was associated with, $A_{combined}$ in Equation 2.7, was scrutinized. In the initial combined heat transfer coefficient calculation, $A_{combined}$ was taken as the entire BSA of the arm in the validation scenario. When computing heat transfer coefficients, they must only be applied to only the areas that will have the heat loss. So, radiative, evaporative and convective heat losses only are a applied to half of the BSA of the neonate because the other half of the BSA is on a heated mattress and unavailable for direct contact with these heat transfer coefficients. As shown in the adult arm in the incubator near field validation measurement, the entire BSA of the arm does not get illuminated by the radar. Consequently, the area of the combined heat transfer coefficient, $A_{combined}$, was reduced to an estimated one-fifth of the BSA of the arm instead of the entire BSA. The decrease in $A_{combined}$ caused an increase in heat transfer coefficient, and the new value for the combined heat transfer coefficient was around 6W/m^{2}C for the validation scenario.

Figure 4.7 shows the thermal model used to recreate the test measurement done during validation: 35C at 20% relative humidity. It can be seen that the increase in temperature of the thermal model, 380mC, is closer to the actual temperature measured, 360mC, with the validation set-up as compared to Figure 4.8 that contains the measurement with the initial heat transfer coefficient of 1W/m^{2}C.

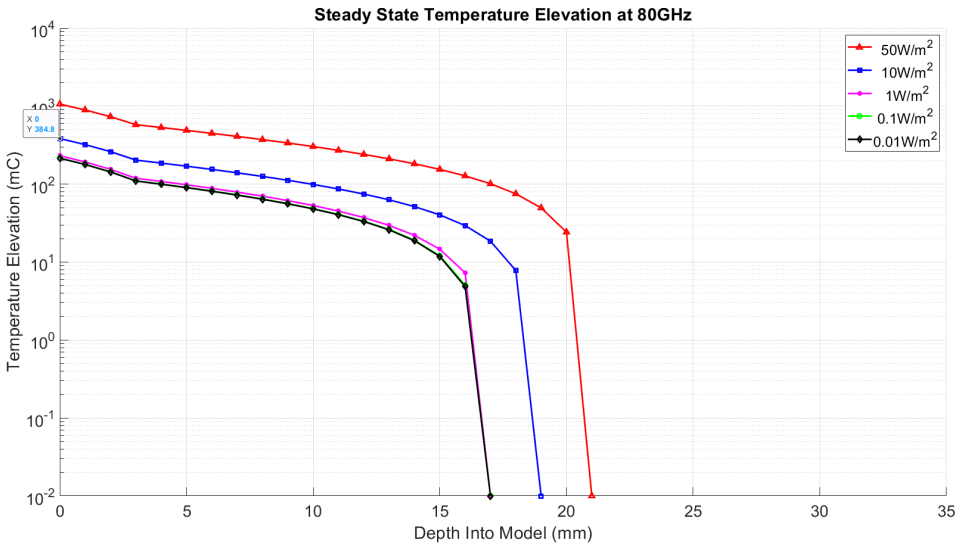

Figure 4.7: Recreation of measurement with incubator set up at 35C, 20% humidity with thermal model created in Chapter 2

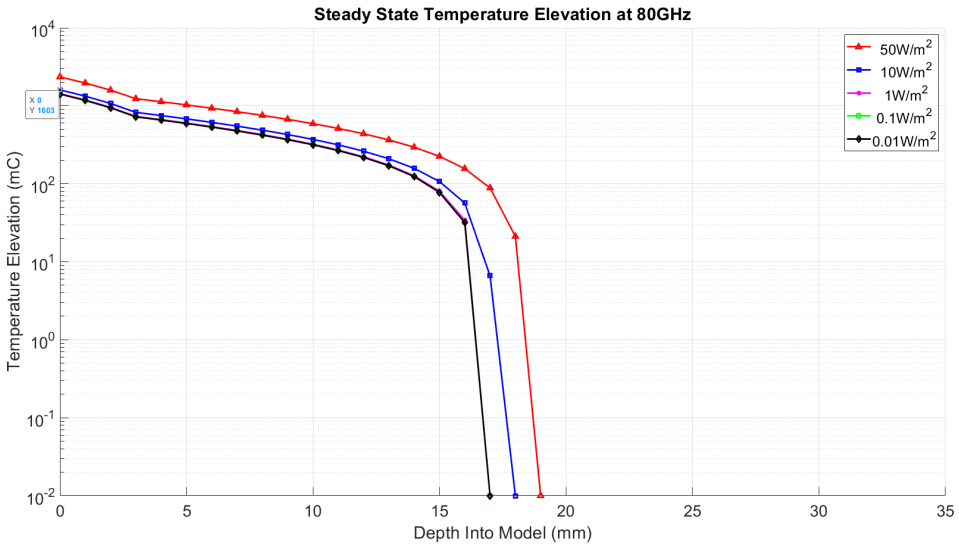

Figure 4.8: Recreation of measurement with incubator set up at 35C, 20% humidity with thermal model created in Chapter 2

Low Power Density Misrepresentation

In Figure 4.9, the far field arm in incubator is measured. The areas that were previously measured for the near field arm in incubator measurement are still used but now the radar module is moved at a distance of 16cm away from the arm. This represents far field and lower power densities.

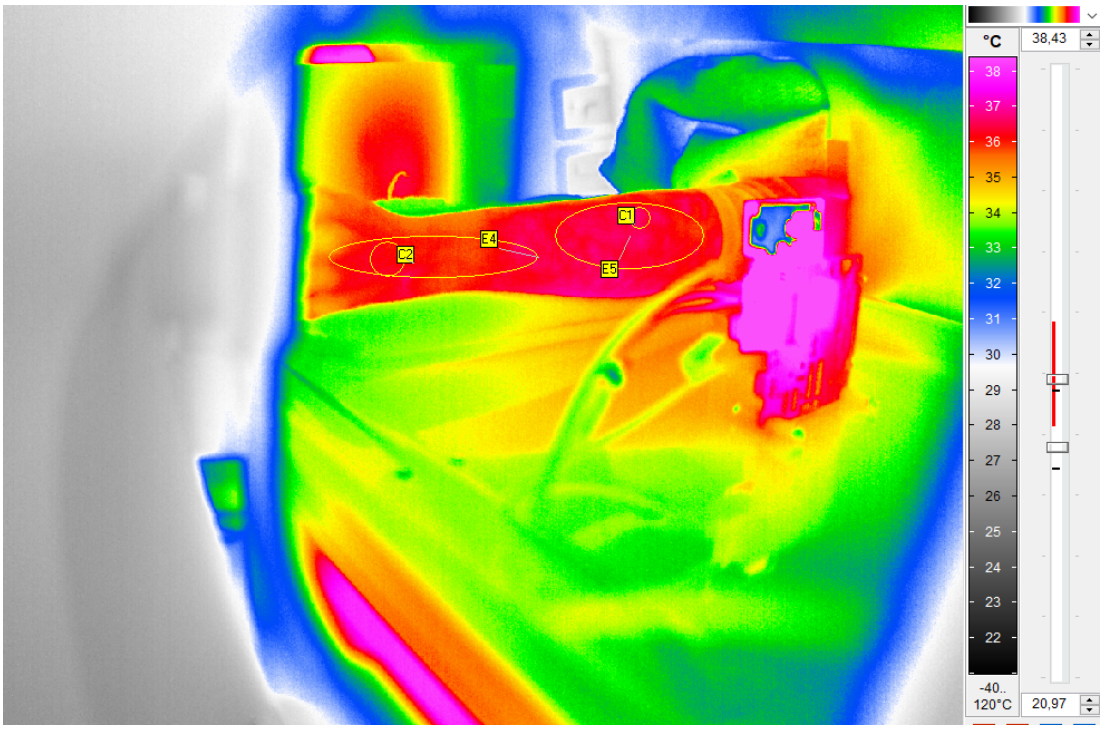

Figure 4.9: Areas measured by the thermal camera for far field measurement with adult arm inside incubator at 35C, 20% humidity

Figure 4.10 contains the measurement for Circle 1, the same area in Figure 4.3 for the near field. The temperature increase recorded by the IR camera for Circle 1 is 136mC and 142mC for Ellipse 5, see Figure 4.11. Both plots show a temperature increase that stabilizes around 20 seconds, similar to the plots for the near field measurement, see Figures 4.2 and 4.4, so it looks as though the temperature increase does occur due to the radar module.

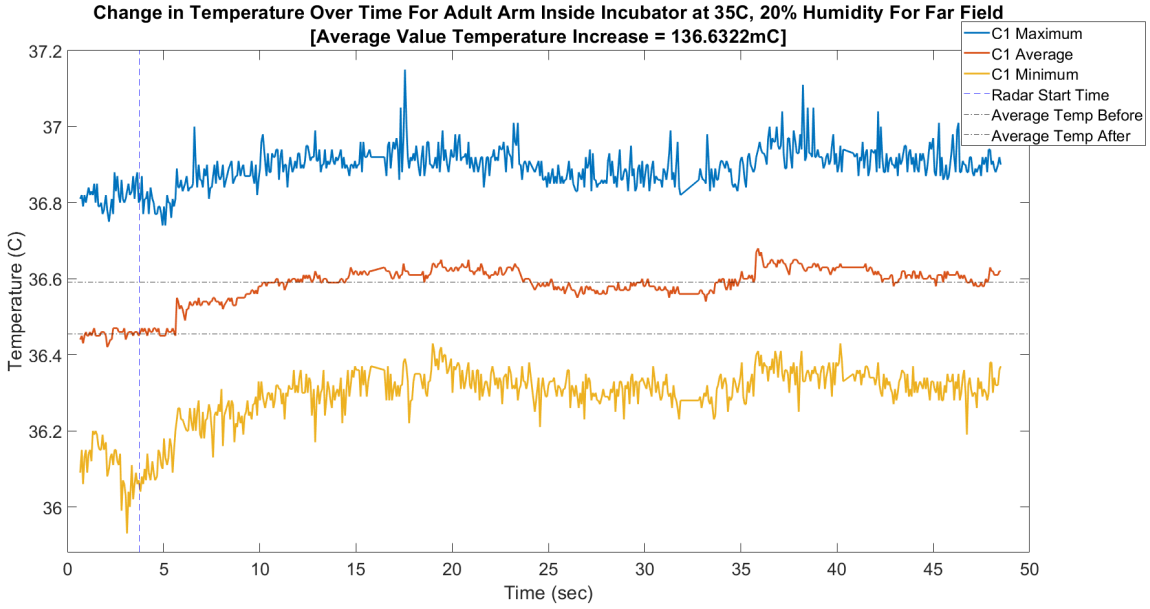

Figure 4.10: Results for far field measurements with adult arm inside incubator inside illumination area for Circle 1

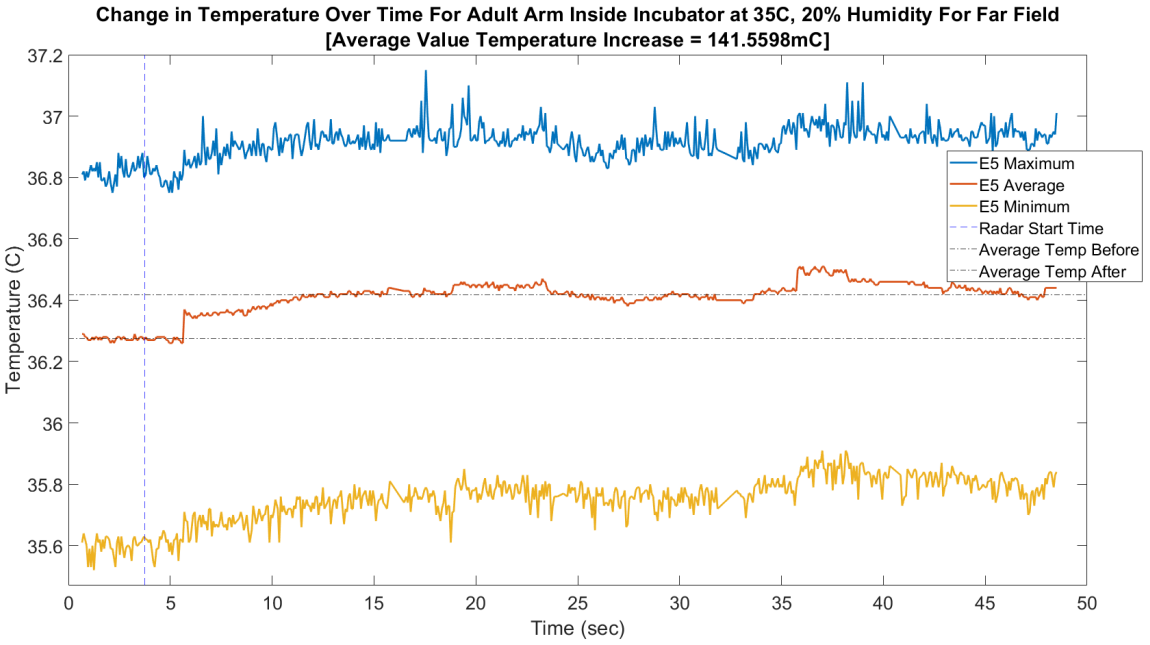

Figure 4.11: Results for far field measurements with adult arm inside incubator inside illumination area for Ellipse 5

With the recalculation of the heat transfer coefficient to 6W/m^{2}C, the thermal model showed a temperature increase for 10W/m^2 that was around the validation measurements. But the lower power densities did not reflect a change in order of magnitude in temperature when the power density changed in order of magnitude, see Figure 4.7. The lower power densities seem to stabilize around 340mC. In the measurements of Circle 1, see Figure 4.10 and Ellipse 4, see Figure 4.11, the temperature increase does not reflect the stabilization behavior. Instead the temperature drops below 340mC to around 150mC. The conclusion from this information is the thermal model created seems only to be able to predict higher power density temperature increases when using lower heat transfer coefficients.

Blood Perfusion Influence

A piece of meat tissue was used in additional experimentation to simulate no blood perfusion, see Figure 4.17. This would be a situation when the neonate has sepsis and the tissue in the area where sepsis is oc-

curring is dying. In this situation, the temperature would theoretically continuously increase as the only way the human body dissipates heat is through the use of blood to disperse the heat throughout the body. The blood brings the heat to other parts of the body to give more area to release the heat to the environment. In Figure 4.17, the radar module was placed in the near field of the meat steak. Circle 1 represents the highest gain area the antenna would have and Point 1 is meant to be farther outside the higher gain area to see how the temperature distributes.

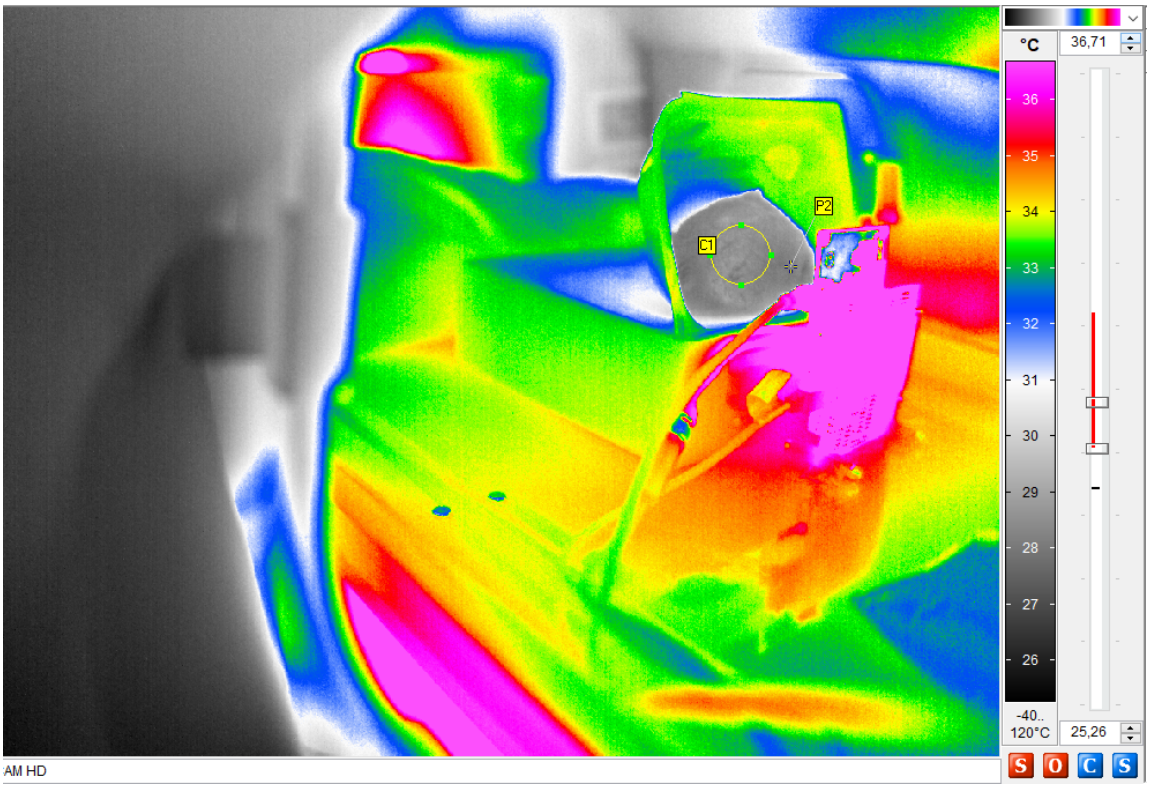

Figure 4.12: Areas measured by the thermal camera for near field measurement with meat steak inside incubator at 35C, 20% humidity

Figures 4.13 and 4.14 show the resulting temperature increases caused by the radar module placed directly in front of the piece of meat tissue. Both plots show a continuous temperature increase with no stabilization reached after 8 minutes of testing. It looks as though the temperature would continue to increase if more time was given to measure, which aligns with the theory that no blood perfusion causes a continual temperature increase as there is no blood to dissipate the heat. In order to calculate the maximum temperature change of both Circle 1 and Point 2, the minimum temperature before the radar module was turned on was subtracted from the maximum temperature taken after the radar module was turned on. Circle 1, see Figure 4.13, has a temperature increase of 810mC and Point 2, see Figure 4.14, has a temperature increase of 1.1C.

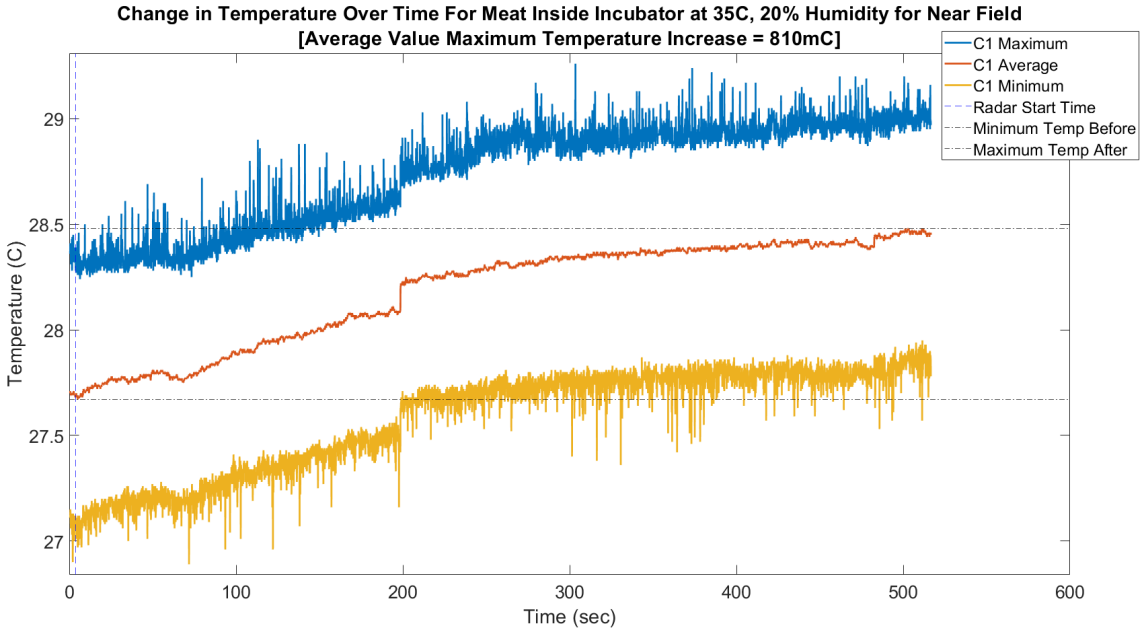

Figure 4.13: Results for near field measurements inside incubator with meat steak for Circle 1

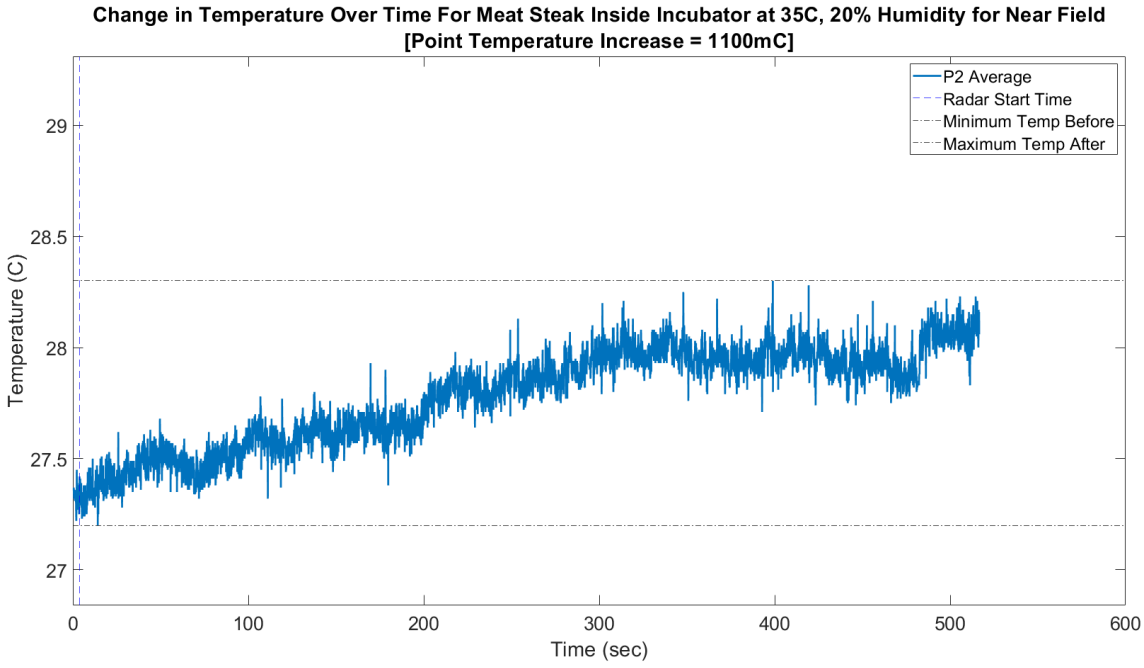

Figure 4.14: Results for near field measurements inside incubator with meat steak for Point 2

The assumption originally made was the temperature increase outside the area of illumination will be less than the area inside illumination as the heat cannot travel outside of the area of illumination because of lack of blood perfusion. Since the measurements are taken of the absolute maximum and minimum instead of an average, this may explain the 300mC temperature disparity between the temperature increase calculated for Circle 1 and Point 2. But the conclusion from these measurements is the assumption may be incorrect and the area outside the illumination area could have the same temperature as the area within and this should be accounted for if sepsis does occur.

It can be seen in Figure 4.17, the piece of tissue does not have the same temperature as the incubator. The temperature of the meat steak stabilized around 28C after 15 hours of heating inside the 35C incubator. So,

during testing, the temperature of the piece of meat tissue was well below its expected value of 35C. Both the inside and outside of the piece of meat was measured, a temperature probe was inserted in the meat steak before continuous wave testing, to be 28C. The assumption could be made that the heat increase seen in Figure 4.13 was caused by the meat steak being heating by the incubator rather than the radar module. Consequently, some research was done into what would cause the potential stabilization around 28C, and it was theorized the liquids within the meat steak created a huge evaporation heat loss that caused the heating rate to decrease significantly. The result being that 15 hour heating time was barely enough to reach 35C. If this were true, then the meat steak was potentially still heating just at a much slower rate than expected and not visible to the IR camera. In order to investigate this theory, the radar module was turned off and the temperature of the meat steak was measured without any heating occurring for 10 minutes.

As seen in Figure 4.16, there is a 7.9mC increase recorded and in 4.15, there is 10mC decrease recorded. This points to the theory the temperature has stabilized around 28C though this seems unlikely. Most likely the temperature increase is so slow that it is not visible by the IR camera. But what was taken from this information is most, if not all, of the temperature increase recorded of the meat steak can be attributed to the radar module. So, for example, the 1C increase in temperature in under 10 minutes measured in Figure 4.14 is mainly caused by the radar module.

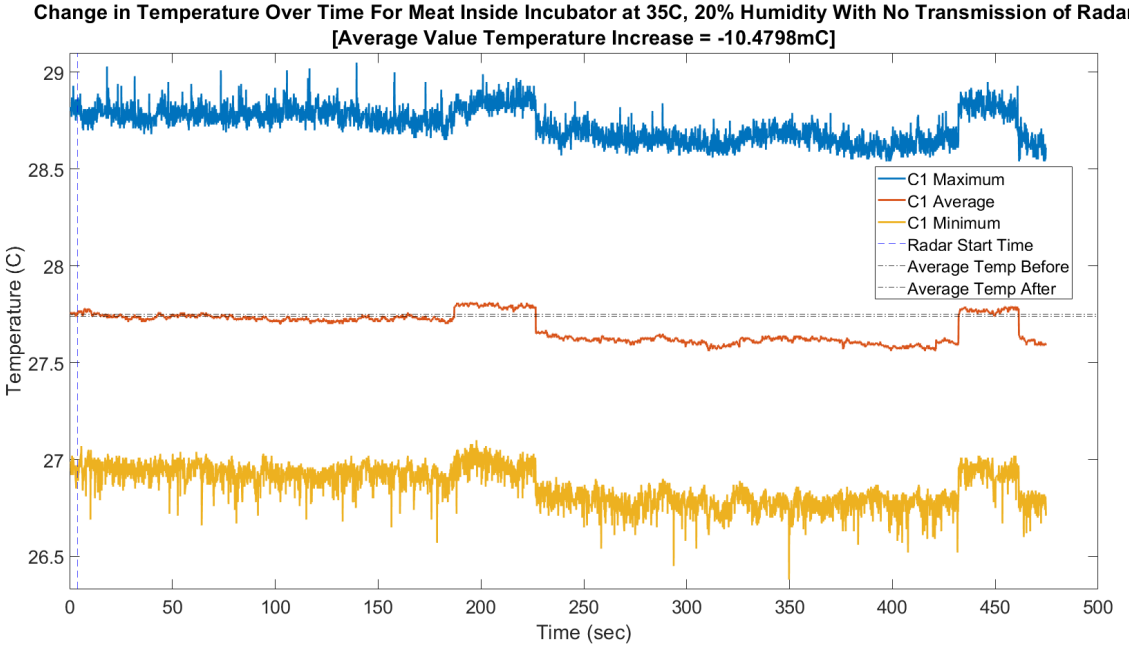

Figure 4.15: Results for measurements of the meat steak while it is not being heated for Circle 1

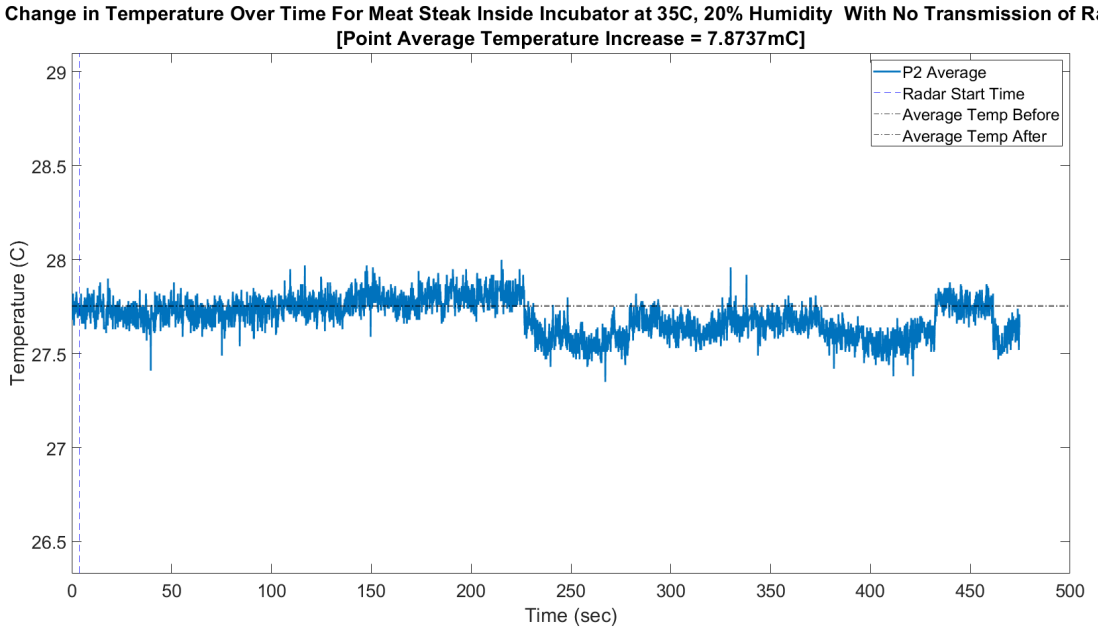

Figure 4.16: Results for measurements of the meat steak while it is not being heated for Point 2

Figure 4.17 shows the same set up with the radar module and the meat steak inside the incubator but the radar module is placed farther from the meat tissue to represent far field. The area and point that were measured are the same as those measured in the near field meat inside the incubator set up.

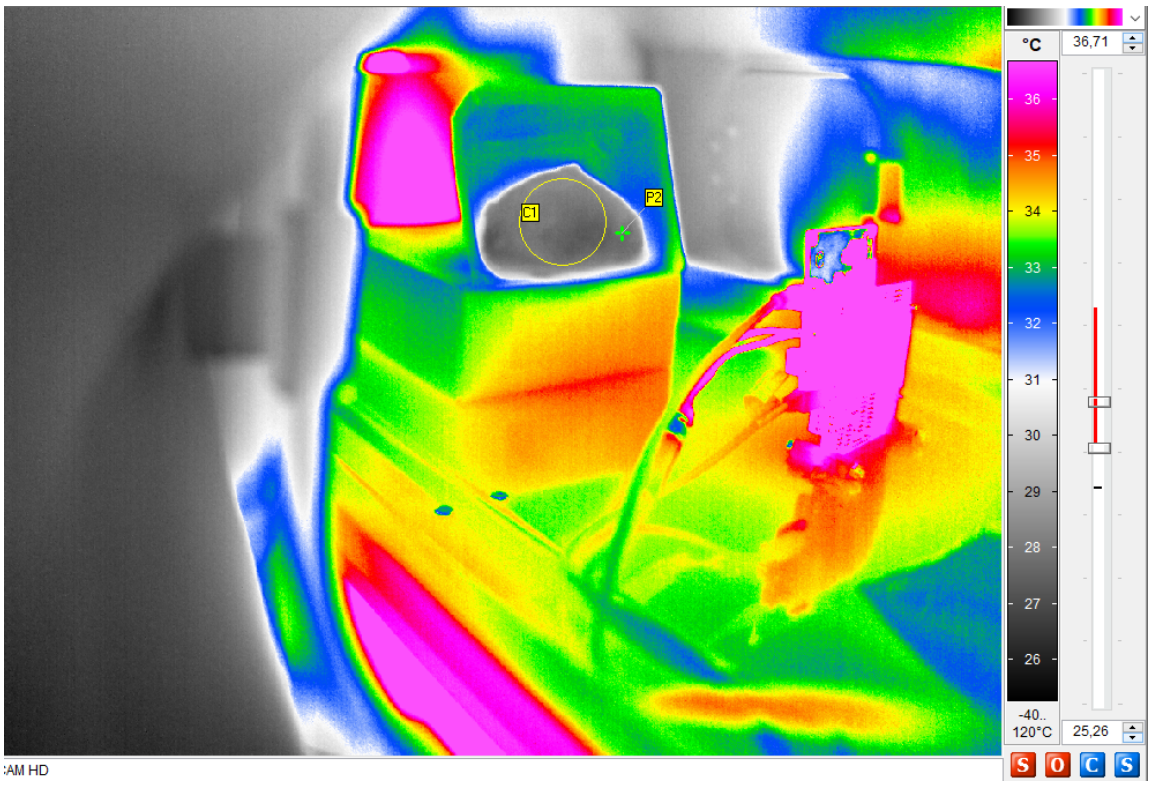

Figure 4.17: Areas measured by the thermal camera for near field measurement with meat steak inside incubator at 35C, 20% humidity

In the near field, there is easily seen an increase in temperature, see Figures 4.13 and 4.14. But, when meat

steak is put outside the near field into the far field, it is difficult to see such a steep temperature increase, see Figures 4.18 and 4.19. But the change in average temperature for both Circle 1 and Point 2 show an increase. Circle 1 has a average temperature increase of 29mC and Point 2 has an average temperature increase of 60mC.

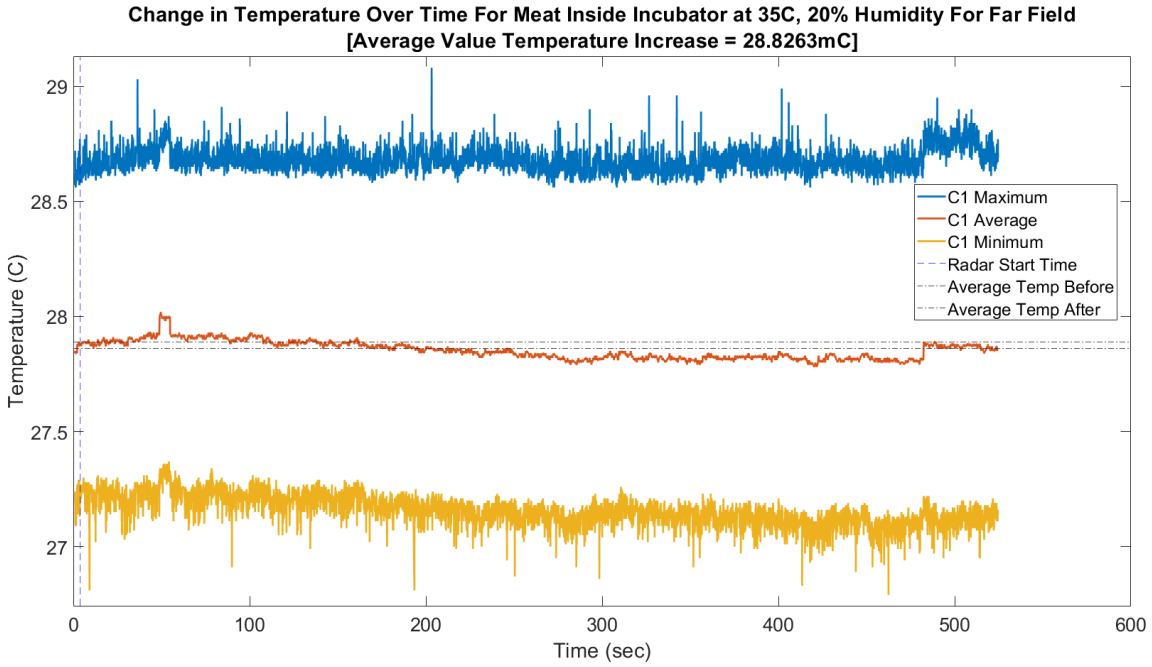

Figure 4.18: Results for far field measurements inside incubator with meat steak for Circle 1

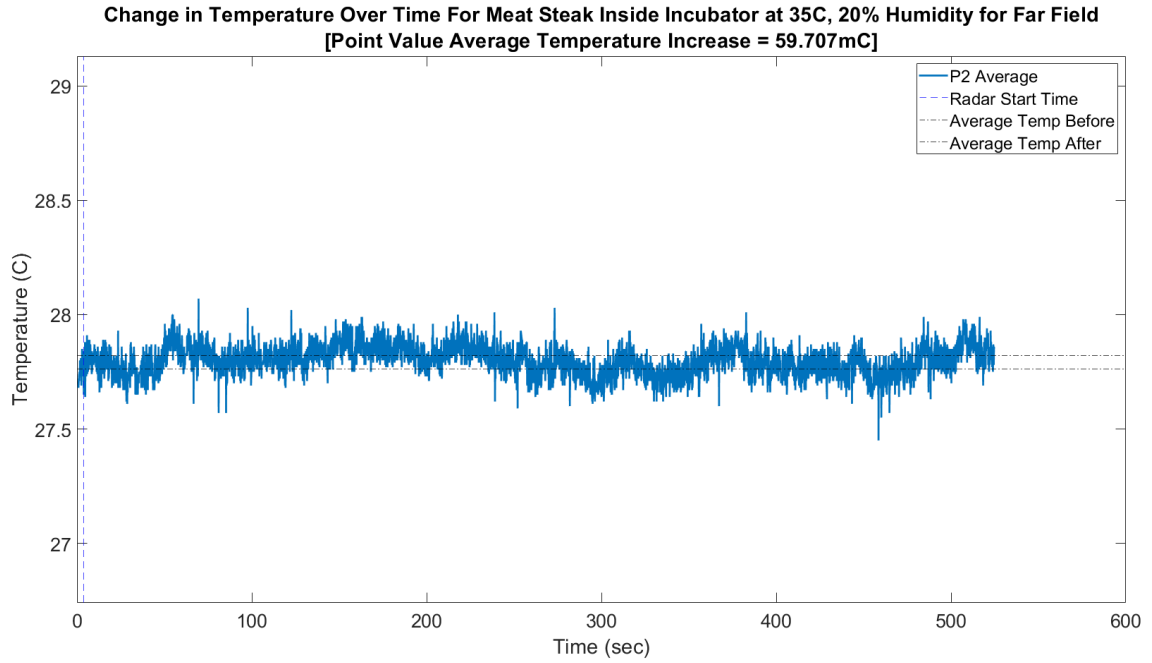

Figure 4.19: Results for far field measurements inside incubator with meat steak for Point 2

It is difficult to discern if the temperature increase measured in the far field is variability in the measurement or if it points to lower power densities also causing a continuous temperature increase when no blood perfusion is present. But the assumption that it is the latter seems more logical as it aligns with the current understanding of heat distribution in the body. The conclusion then becomes lower power densities cause

a slower rate in temperature increase. How this information will translate into the NICU application is addressed in the next section.

How blood perfusion translates into the thermal model is more difficult to discern from the validation results. Since there are only two different types of blood perfusion measured, ideal and none, there isn't much to correlate with. Especially since the thermal model cannot account for no blood perfusion. Consequently, the decision was to remain with an ideal blood perfusion with the model for further estimations of temperature. More research needs to be done with the validation set up to try different amounts of blood perfusion if a correlation is going to be made.

Translation to Application Environment

Using the results from the heat transfer coefficient calculation, it was then concluded that the entire BSA of the neonate should not be used in the heat transfer coefficient equation but only the radiated area. In that case, the general estimation was the radiated area was one fifth of the neonatal BSA. Using this assumption, the heat transfer coefficient of the neonate went from around 1W/m^{2}C to 5.3W/m^{2}C. And the estimated temperature increase caused by 10W/m^2 went from 1.6C to 542mC, see Figure 4.20 for a thermal model for 80GHz with a heat transfer coefficient of 5.3W/m^2. This is within the variable temperature of the neonate's skin throughout the day, which is around 3C.

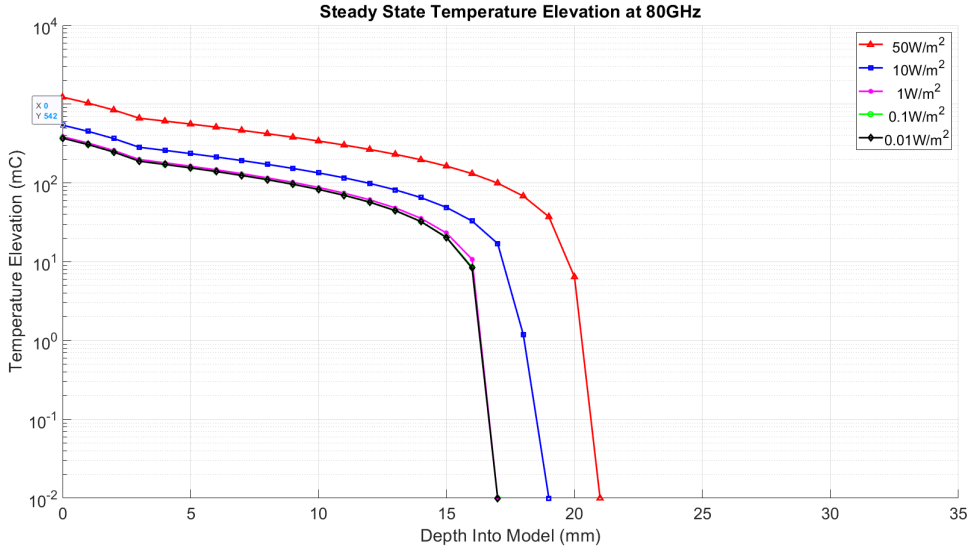

Figure 4.20: Results of the temperature elevation into the tissue caused by 80GHz with a heat transfer coefficient of 5.3W/m^{2}C

Comparing the adult arm plots in Figures 4.3 and 4.10 and Figures 4.4 and 4.11, a conclusion was made that lower power densities are not as easily modeled in hot environments using the thermal model. According to Figure 4.7, which recreates the validation environment using the thermal model, the lower power densities should have a temperature increase that remains around 340mC instead 150mC was measured. The reason for this misalignment is most likely the inability to correctly simulate the skin's response to hot temperatures. Thus the thermal model will not be adjusted with new skin parameters and the worst case scenario will be taken from the plots.

Since the validation results mainly focused on two types of blood perfusion, one of them not able to be modeled in the thermal model, looking at the effect of blood perfusion comes down to only looking at the thermal model itself. A change in order of magnitude of blood perfusion seems to double the temperature increase. With a blood perfusion from 1 mL/kg/min to 10 mL/kg/min at a heat transfer coefficient of 7W/m^{2}C, the temperature increased from 433mC to 820mC, see Figure 4.21. A change in heat transfer coefficient of 6, for blood perfusion at the skin of 1 mL/kg/min and 10 mL/kg/min, the temperature increase from 1C to 2C, see Figure 4.22. With a change in 1 of heat transfer coefficient, the temperature seems to double as well.

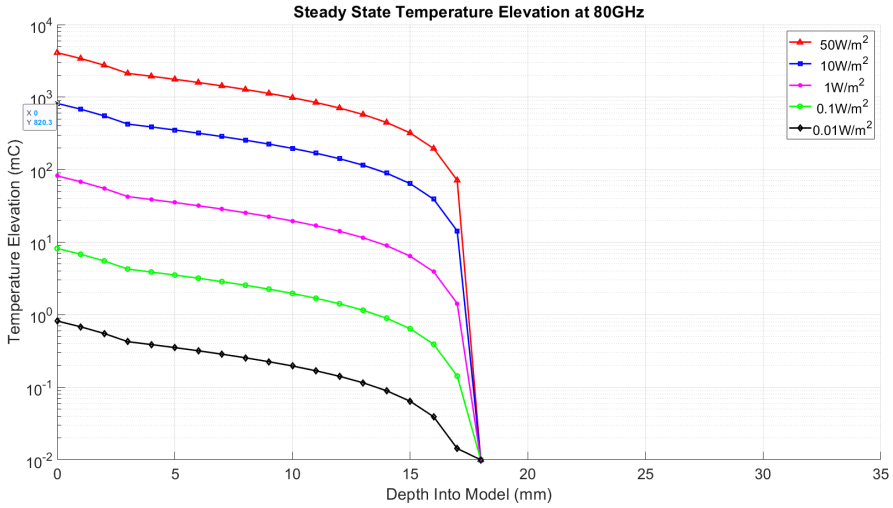

(a) Blood perfusion 1 mL/kg/min for skin with heat transfer coefficient of 7

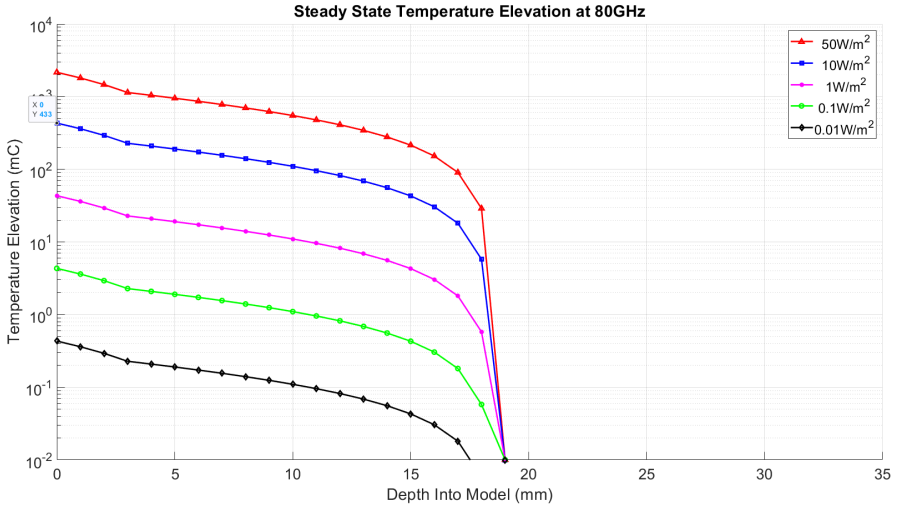

(b) Blood perfusion 10 mL/kg/min for skin with heat transfer coefficient of 7

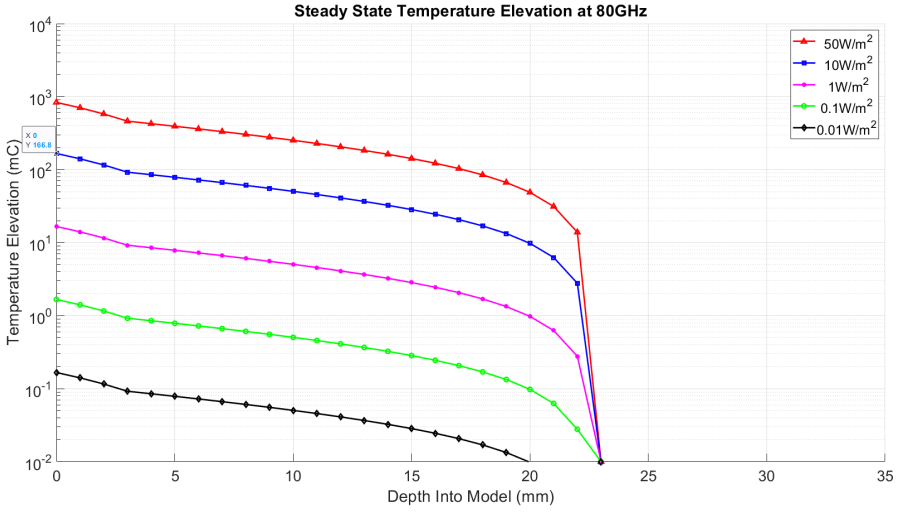

(c) Blood perfusion 100 mL/kg/min for skin with heat transfer coefficient of 7

Figure 4.21: Thermal model changes based on blood perfusion for a heat transfer coefficient of 7

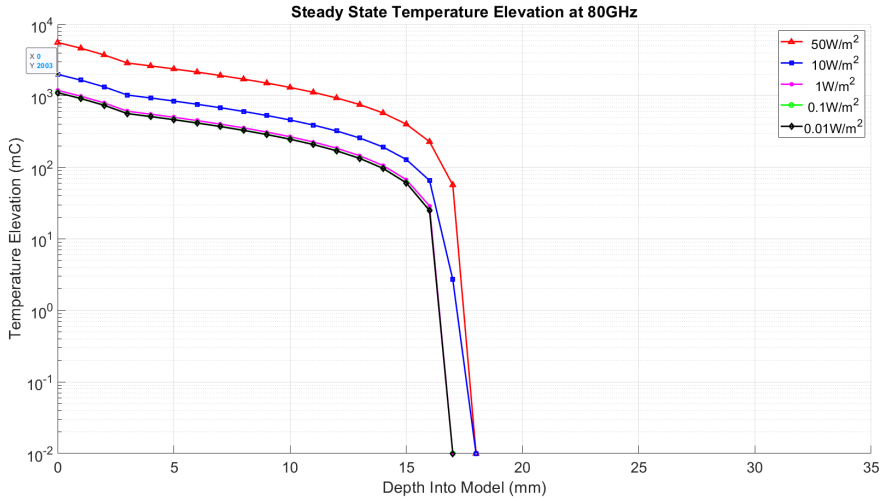

(a) Blood perfusion 1 mL/kg/min for skin with heat transfer coefficient of 6

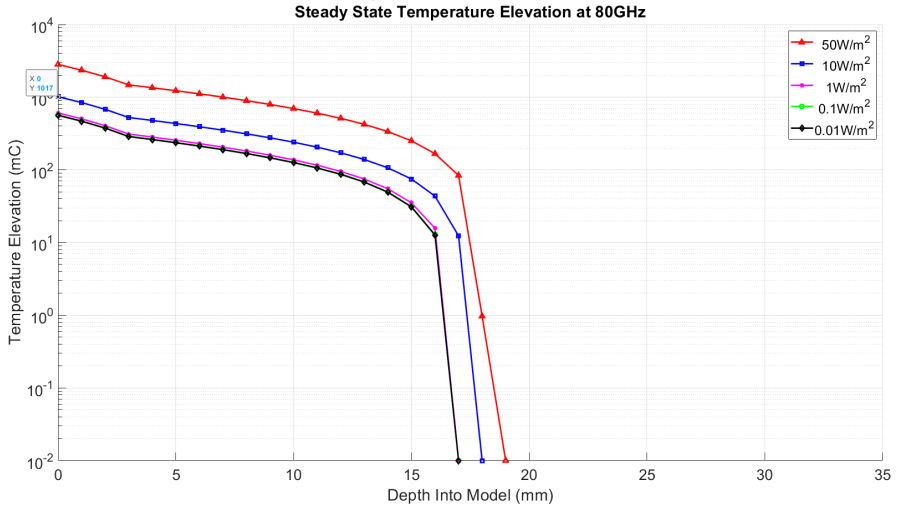

(b) Blood perfusion 10 mL/kg/min for skin with heat transfer coefficient of 6

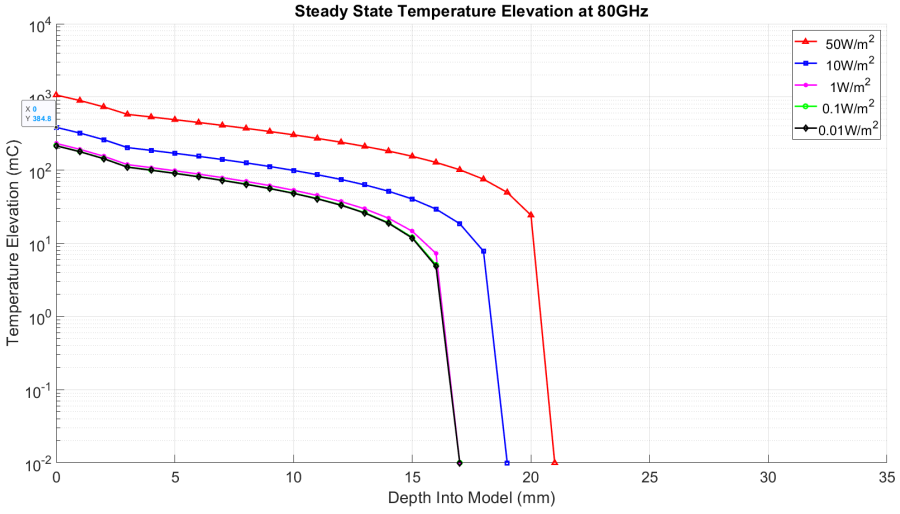

(c) Blood perfusion 100 mL/kg/min for skin with heat transfer coefficient of 6

Figure 4.22: Thermal model changes based on blood perfusion for a heat transfer coefficient of 6

These results point to an issue of temperature increase as a neonate goes into sepsis. As blood flow gets weaker and weaker with the hot environment of the neonate, the temperature increase could be substantial. But the increase may be exceedingly slow as seen in Figures 4.18 and 4.19 where a lower power density caused a temperature increase in the tens of milli-Celsius after 10 minutes. This may be beneficial as sepsis can be identified without any substantial damage being done from radar module heating or it may be detrimental because the gradual temperature increase is harder to detect. A safety monitoring system will need to be designed with neonatologists to determine when a heat increase is unsafe, potentially using a temperature sensor on the top of the skin. This system may be beneficial in detecting sepsis if it is used to detect a continuous temperature increase over time. At the very least, a consultation with neonatologists should be done to understand at what point the issue of very low blood perfusion takes priority over treatment of substantial heat increase.

4.2. Signal Processing and Amplitude Detection

The potential of the system to scale down to measure extremely small neonates comes down to quantifying the smallest amplitude displacement that can be measured by the system. This section gives a deeper explanation of what needs to be quantified and how and points out two potential methods to do so. First, it explains how the heart and respiration rate will be measured in the final application, and it gives a few patient measurements. This gives better insight into what needs to be quantified. Then, it the two methods for this quantification process are layed out and evaluated with real-life measurements. Their result give insight into the system's capabilities for measuring neonates.

4.2.1. Heart Rate and Respiration Rate

The basic premise of reading the hart and respiration rate with radar is to take two fast Fourier transforms (FFT). The first finds the range bin where the person is and the second finds how the person in that bin is vibrating. The vibration is a representation of the movement of the heart and lungs and, in this case, the displacement of the chest they cause. Figure 4.23 shows the signal processing steps of getting the heart and respiration rate from the radar information.

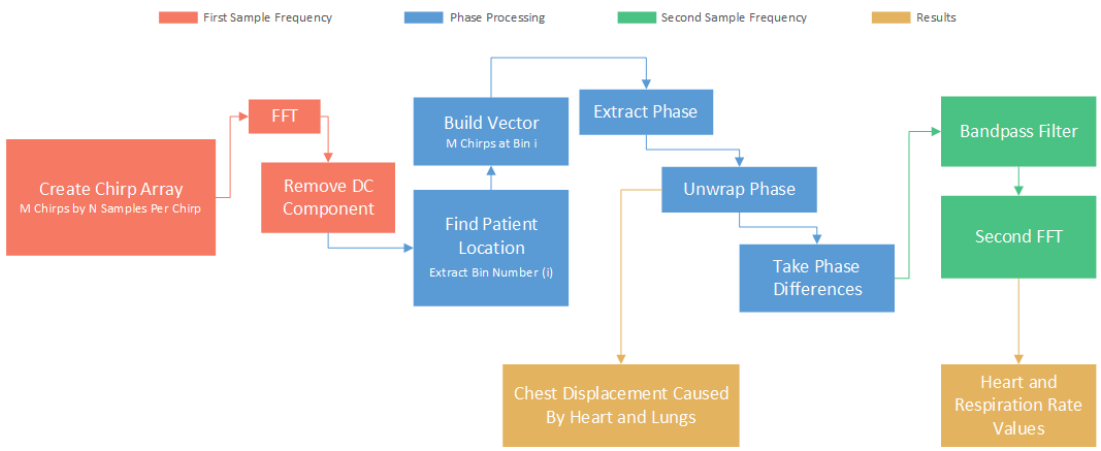

Figure 4.23: Block diagram of the signal processing steps in order to extract the heart and respiration rate

Starting with the first FFT, the position FFT. First, the radar module finds the bin that contains the person. When measuring a received RF signal, the analog to digital converter (ADC) does not have an infinite number of points. That means there are gaps between the points that are measured which result in steps in the FFT that are a certain amount of hertz in size. These gaps are called bins. In one of these bins is the location of the person and that bin is called the range bin. After finding the range bin, an array is made of M number of chirps and N number of bins, and the vector containing M chirps of the range bin number is extracted. In the signal processing written for this application, the assumption is the subject is in the same range bin during entire measurement time. So, once the range bin is found, it remains static.

In order to pull the heart and respiration rate out of the noise of the range bin, there are additional signal processing steps done. This is where the phase of the signal is unwrapped. After finding the range bin, the phase is extracted from it. The result is a vector of the phase values of the range bin over time.

After extracting the phase from the range bin and creating a vector of the phase values, the phase is unwrapped. Phase values are between [-π, π] and need to be unwrapped to obtain the chest displacement waveform over time. Phase unwrapping is performed by adding or subtracting 2π from the phase whenever the phase difference between consecutive values is greater or less than $\pm\pi$. The unwrapped phase can be shown as chest displacement with both the heart and lungs pushing on the chest being visible. There is another phase operation performed, the phase difference calculation. It is performed on the unwrapped phase by subtracting successive phase values. This helps in bringing the heart and respiration rate out of the noise.

After unwrapping and taking the phase difference, the values of the phase are passed through two band-pass filters with varying bandwidths and starting and stopping frequencies dependent on the heart and respiration rate value that is expected. The data after bandpass filtering of the phase can be displayed as a breathing waveform and heart waveform, see Figure 4.24 for examples of heart and lungs pushing on the chest. The second FFT is performed with this information. From here, the maxima can be found for each data set and the result displayed as the heart and respiration rate frequency.

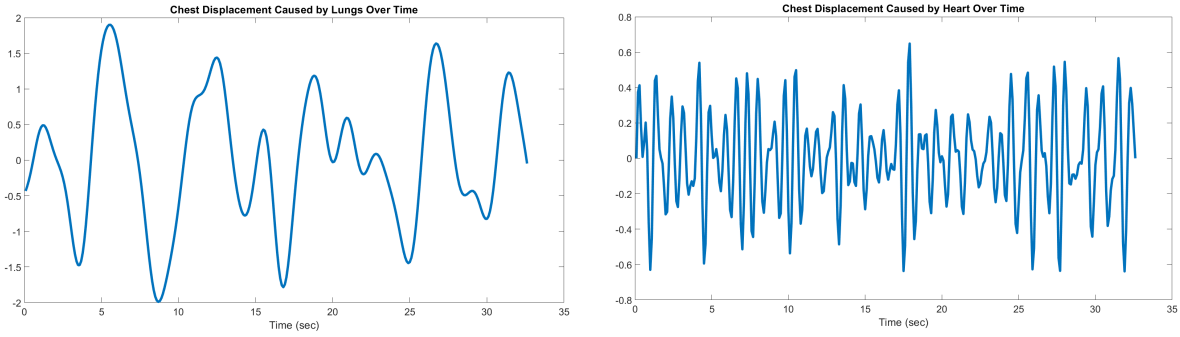

(a) Chest displacement caused by lungs

(b) Chest displacement caused by heart

Figure 4.24: Chest displacements measured with FMCW radar module on adult that show heart and lungs affect on the chest

It is important to note that the EKG is not measured. It is how the heart and lungs push on the chest. Consequently, the result is that the heart and respiration rate values are given, but also how the chest is moving. The measurements plotted in Figure 4.24 are of a patient sitting in front of the radar module that will be used in the final application. In order to check the accuracy of the measurement of the heart rate, a heart measurement watch was worn by the user while the measurement of the radar was done. The average values that were given by the radar were almost equal to the results of the watch.

This leads to what needs to be quantified to understand the capability of the system to measure a neonate's heart and respiration rate. The capability does not come from the accuracy of the system, which is the ability of the system to differentiate between two distances between two people using the first FFT. As seen in Figure 4.23, in order to successfully measure a neonate, the smallest amplitude change detectable by the second FFT or, in other words, the smallest amplitude detectable within the range bin of the first FFT must be found. This is a bit more complicated than measuring the accuracy of the system because the set-up available is made for accuracy measurements. It cannot vibrate, it can only move at small steps between distances. Consequently, only two distinct distances can be measured during different data collection sessions leaving two data sets of two distances. How to combine these two data sets in a way that gives an understanding of the system's smallest amplitude detection capabilities is addressed in the next section.

4.2.2. Smallest Amplitude Detection

Seeing as the goal of the system is not to better see the location of the neonate but see how much their chest moves, the challenge isn't to see the accuracy of the first FFT but of the second. This leads to a difficult problem because only a computer numerical control (CNC) arm is available for measurements, and it does

not have the ability to vibrate. So, this leaves the challenge of finding the smallest amplitude detectable by the system using unique data sets associated with its own distance. Two proposals were given to process these data sets and provide a number for the smallest amplitude detectable. The first proposal uses the first FFT to see how the different distances spread across multiple bins. The second proposal is to see if distortion of two distances can be seen with the second FFT by mixing them together. Consequently, in this section, both proposals will be described with their associated conclusions. The description of the set-up for using the CNC machine is explained. The CNC machine was constrained to a 10μm step, so that is the smallest position delta that was plotted for each measurement.

First FFT Amplitude Difference

When a large object is measured at a certain position, the resulting energy received from the transmitted signal bouncing back from said object is spread across multiple bins. The main bin is normally processed and associated with how far away the object is from the radar module. In this proposal, in order to measure the smallest amplitude, the main bin and the bins left and right of the main bin are examined. The spreading of the energy across these three bins will be exploited for the smallest amplitude detection measurement in one bin measurement.

Looking at the main bin and the amplitude differences in the different distances in the bin and the surrounding bins showed how the distance was distributed across the FFT. If the different amplitudes of the distances were seen and still in the same bin, then theoretically the FMCW parameters were enough to see the small change in amplitude. If the change in amplitude relative to the starting distance is visible, then theoretically the small change in amplitude can be measured with the second FFT. If the amplitude of the delta distance is not visible from the starting distance in the first FFT amplitude, then the opposite is true and the distance is not measurable by the second FFT.

In Figure 4.25, the center bin that contains the main tones can be seen with the left and right bins next to the center bins. The bins are zoomed in to reduce the noise and show only the main tone. The way the measurement works is that it finds the bin that the main tone is located. Then, it plots the left and right bins next to it to see the distribution of the tone over the three bins. The main tone serves as the reference tone. If the delta tone is below the reference tone in one bin then it should be higher in the next bin. Including the other bins shows that if the amplitude difference at one bin then it can be included in another bin.

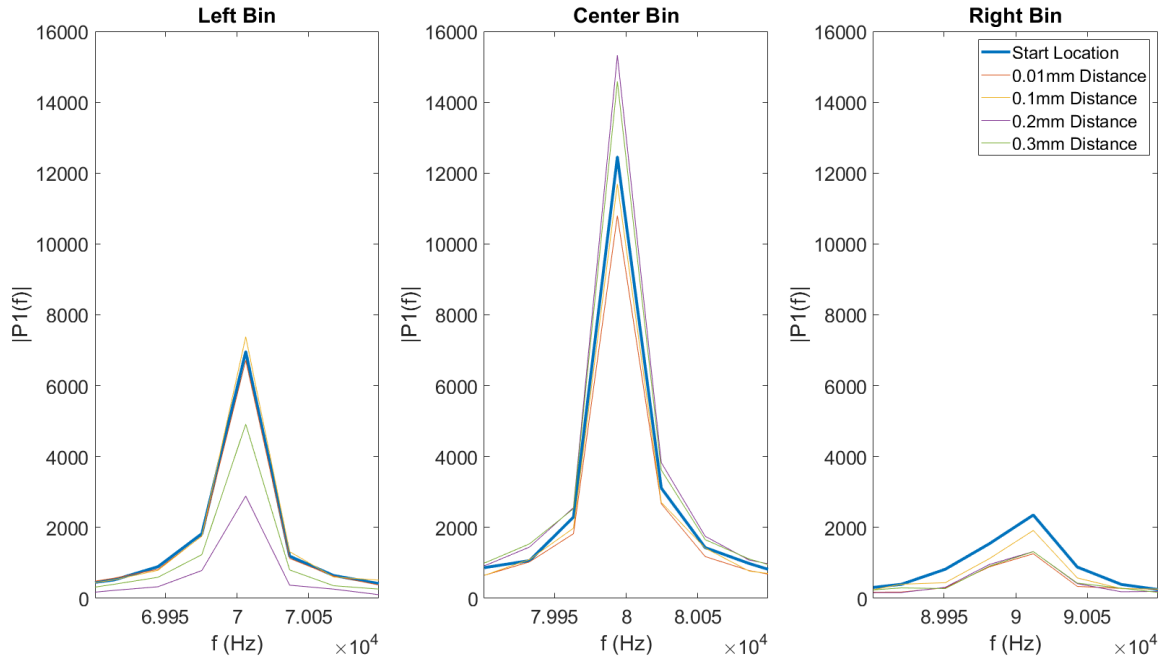

Figure 4.25: The changes in amplitude of the first FFT for each distance from the start location

As it can be seen the signal is distributed between the three bins. But, with every distance from the start loca-

tion, there is a difference in amplitude that can easily be seen. Except for 0.01mm, which has odd behavior. If the tone is above the start location tone in the left bin, then it should be below the start location tone in the center bin. This is because the tone is spread across bins and each tone should have an equal amount of energy, just spread different across bins. The 0.01mm tone has a lower amplitude than the start location throughout the bins. Consequently, further investigation into if a 10μm step can be measured was done.

Second FFT Signal Processing

There are some signal processing techniques put in place to bring the heart and respiration rate signal out of the noise as stated in the previous section. This includes the phase unwrapping and taking the phase differences. If the FMCW chirp parameters are not enough to distinguish the small amplitudes of the neonate's chest, then the implementation of these steps could potentially help. In order to show if those can help increase the ability to see smaller amplitudes in the second FFT, a second test was created that incorporated distortion into its measurements.

The processing of the output data is similar to the heart and respiration signal processing flow. The new flow involves taking only two of the independent data sets for different distances that are transmitted for instead of plotting all of them together as in Figure 4.25. The range bin is found similar to finding the center bin in the first FFT measurement. The goal is to have the two different distances in the same bin to simulate the vibration of the person within the range bin. Once the center bin is found for the independent data sets, they are multiplied together to replicate them mixing and to create one data set. This is the new range profile that will be put into the signal processing flow described in Figure 4.23. Figure 4.26 shows where the mixed bins will fit in the original flow diagram.

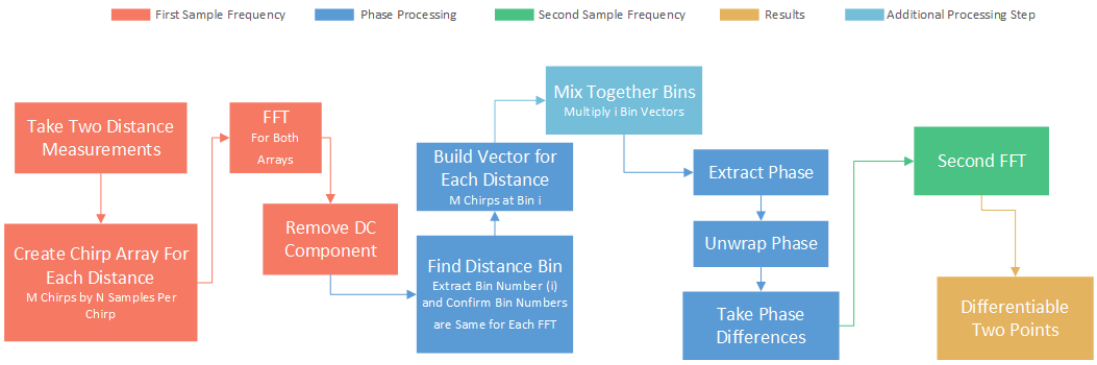

Figure 4.26: Block diagram of the signal processing steps in order to extract the OPI3

The goal is to use intermodulation distortion to determine if the two positions are measured at different locations on the spectrum. If two frequencies are multiplied together, then they are added and subtracted against one another and their harmonics. For example, if 2.2Hz and 2.3Hz are multiplied together then 0.1Hz and 5.5Hz, see Figure 4.27 for a spectrum with multiple distortions relating to intermodulation of two tones. If the frequency of the tones are the same, then the power distortion is non-existent. The two tones are added onto one another in the same frequency location. If the frequencies have enough distance between one another, then the distortion can be seen throughout the FFT. In Figure 4.27 the distortion that will be plotted using the signal processing flow shown in Figure 4.26 is highlighted. Consequently, the goal, after going through the signal processing chain, is to see two tones distinct from one another in the FFT produced. If there is no difference seen between these signals, then the change in amplitude is not detectable by the radar module. In the first FFT, it mainly focuses on the capabilities of the FMCW parameters. The intermodulation distortion measurement tries to incorporate the signal processing that is employed in heart and respiration measurements. Adding signal processing can help determine if it adds anything to the smallest amplitude detection capabilities. If the second FFT process cannot distinguish different tones, then it most likely means the combination of FMCW parameters and signal processing will not be able to detect such a small amplitude. The next step would most likely be to modify the FMCW parameters and measure again.

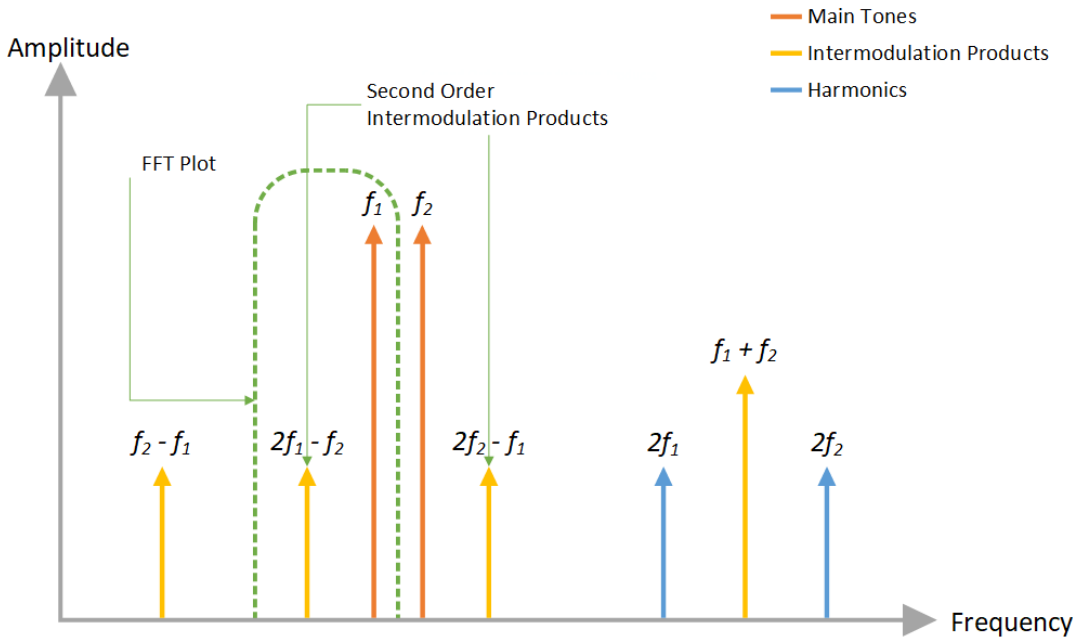

Figure 4.27: Third order intercept point example

Since the bins are multiplied together, the change in position is seen as simultaneous. Thus, the location of the distortion will be at the highest frequency the FFT. In the Matlab processing, the FFT plots are shifted from the end of the FFT to the middle to better see the two tones. Figure 4.28 contains multiple figures that show continuously larger displacements to the original position. Figure 4.28a contains the measurement of a displacement of 0.01mm. The distortion is still slightly within the main tone, but is partially visible. Figure 4.28b contains the measurement of a displacement of 0.1mm. Here the tone is more easily visible, yet still part of the main tone. Not until Figure 4.28d can the tone be seen as two separate tones independent of one another and multiple distortion tones seen.

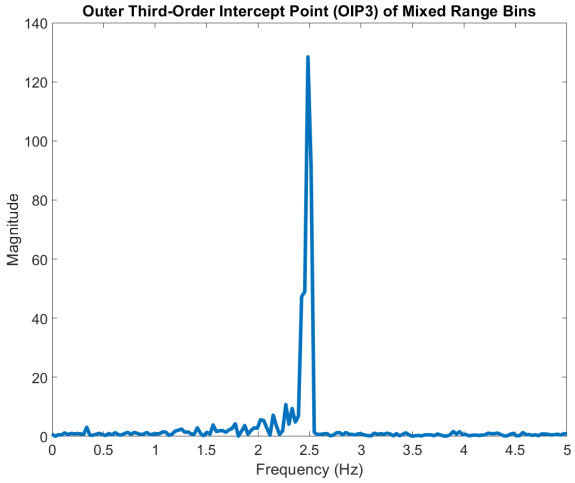

(a) Distance displacement of 0.01mm

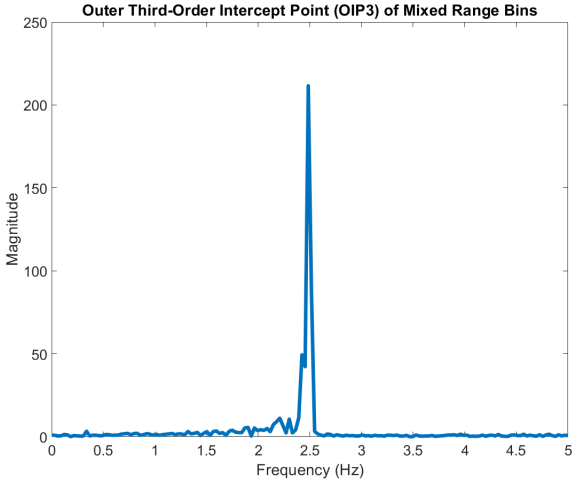

(b) Distance displacement of 0.1mm

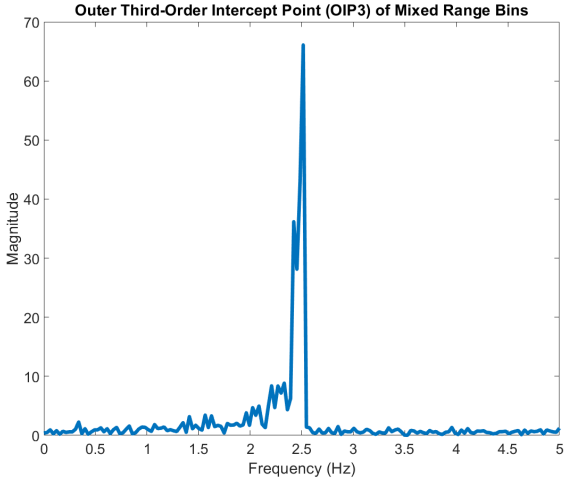

(c) Distance displacement of 0.2mm

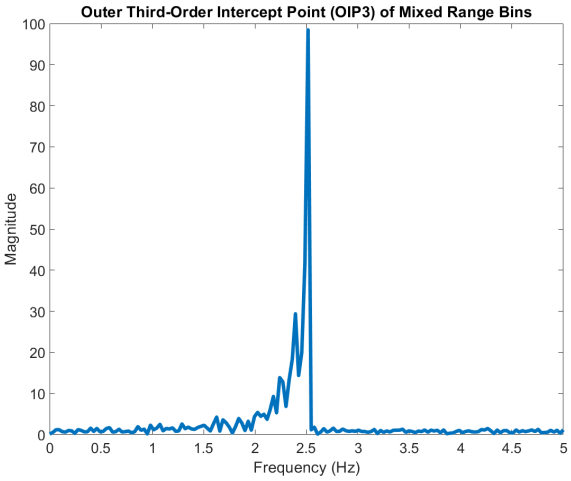

(d) Distance displacement of 0.3mm

Figure 4.28: Difference in OIP3 dependent on distance from starting point

The set up was created using a CNC machine with an arm that is controllable in x, y, and z directions. A metal plate was attached to the arm and maneuvered in the x and y direction to be in front of transmitter two, see Figure 4.29. Then it was placed 16 cm away from the antenna. A CNC machine was used to make sure that the changes in distance from the radar module were exact, the smallest step the CNC machine has is 10μm. An inital starting point measurement was taken. Then, the CNC machine as stepped up 0.01-0.1mm distances away from the starting point. At each point, a series of FMCW chirps were initiated and the subsequent ADC data that was stored in a downloaded memory data set taken from the integrated development environment (IDA) associated with the radar integrated circuit (IC). Two Matlab scripts were written for the different measurement types to compute the smallest amplitude detection.

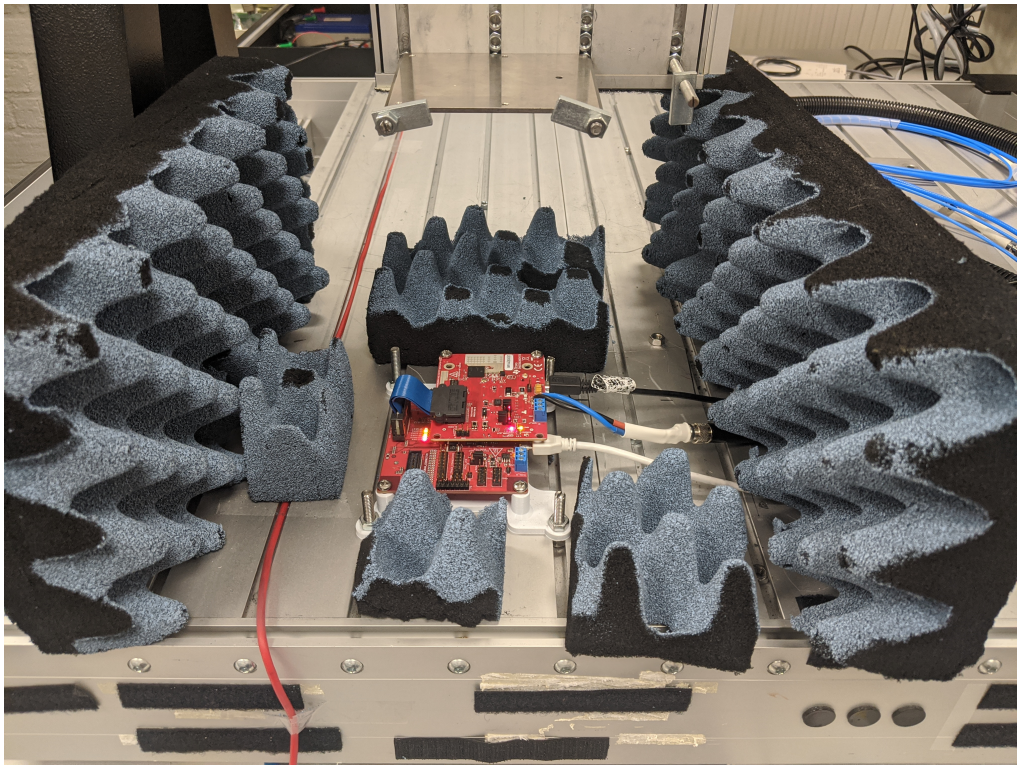

Figure 4.29: Set-up of the accuracy measurement done with the CNC machine

4.2.3. Results

Using the first FFT, the FMCW radar parameters were shown to be able to detect a distance delta of 0.1mm. The displacement amplitude was able to be distinguished within the amplitudes of the left and center bin when compared to the amplitude of the initial position. But the results for a 0.01mm delta were unclear. When seeing an amplitude change that is higher at one bin, then it should be lower in the other bin as compared to the amplitude of the original position. This is because the same energy spreads throughout the bins, just with varying amplitudes across bins. In the first FFT results, the amplitude of the 0.01mm delta was consistently below the amplitude of the starting position. It is unclear what caused this, so more investigation into how to measure the smallest delta of the second FFT was done.

Potentially, the FMCW radar parameters on their own cannot detect a small amplitude change of 0.01mm. But, as stated previously, there are additional signal processing techniques employed to get the heart and respiration rate out of the noise floor that the signal processing chain uses. The second FFT proposal would incorporate those techniques by adding in the entire signal processing chain of the heart and respiration rate measurement into the calculation. Using the second FFT would require mixing the bins together and measuring their resulting distortion. Using this technique, the distortion of 0.1mm delta was seen, see Figure 4.28b, but also 0.01mm delta was visible, see Figure 4.30a though both were still a part of the main tone. The conclusion was that a 0.01mm delta can be detected with both the FMCW radar parameters and the signal processing, but more work may need to be done to craft a FMCW configuration set that brings the 0.01mm

delta further away from the starting point as seen by the Matlab post processing.

A second conclusion is the second FFT process is not as consistent as the first FFT signal process, as seen in Figure 4.30. Figure 4.30a shows one measurement of the 0.01mm delta, Figure 4.30b shows a second subsequent measurement and Figure 4.30c shows a third. As it can be seen, the distortion is different for both and sometimes the distortion tone cannot be seen. The resulting deuction from this is the measurement of the second FFT should be used more as a subsidiary of the first FFT measurement and potentially could be improved upon as more time is taken to understand what intermodulation is being represented by the FFTs in Figures 4.28 and 4.30.

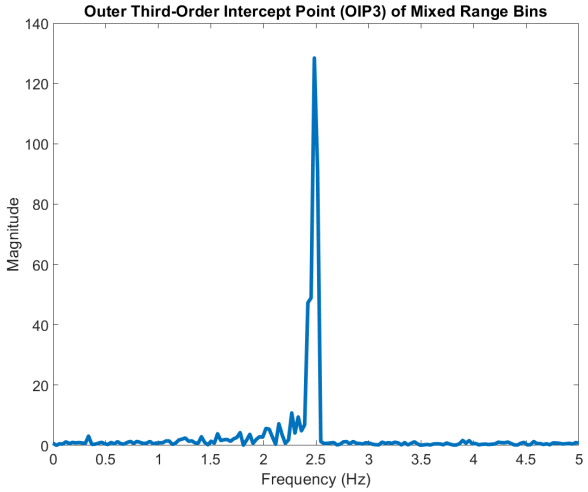

(a) Distance displacement of 0.01mm for first measurement

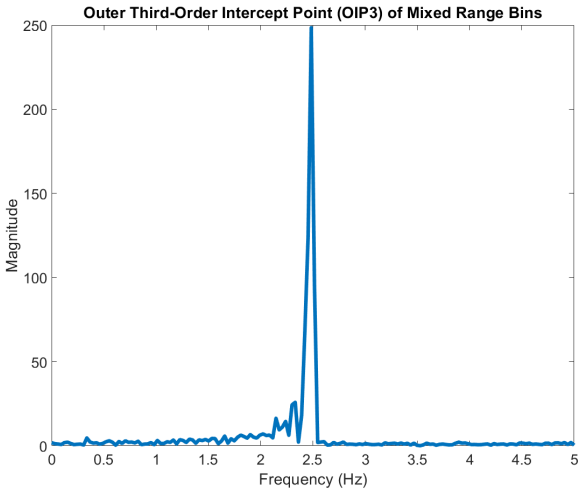

(b) Distance displacement of 0.01mm for second measurement

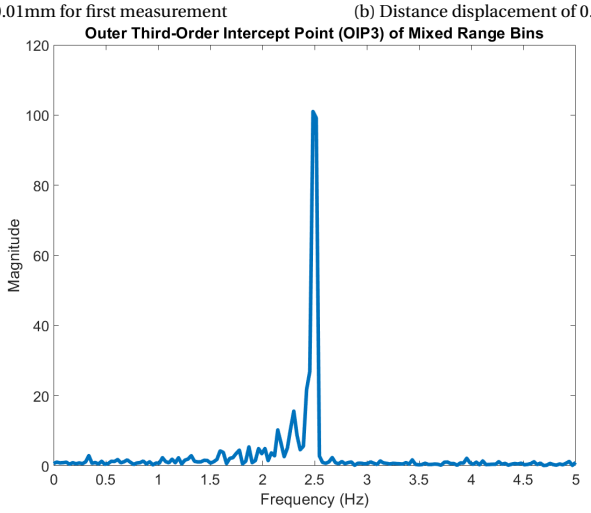

(c) Distance displacement of 0.01mm for third measurement

Figure 4.30: Difference in IIP3 at same distance dependent for different measurement runs

Another interesting result of these measurements is the set up allows for the bin size to be correlated to amplitude detection. It was theorized that reducing the bin size increases distribution of return energy along bins meaning the main bin will have larger amplitude changes for smaller distance displacements. Thus, smaller distance displacements will be easier to detect. But the direct relation of bin size to changes in amplitude has not been previously found. Using the measurement set up, a larger amount of data can be gathered to quantify the correlation between bin size and amplitude displacement.

The FMCW parameters given in Table 4.1 are the ones used to create the heart and lung waveforms plotted in Figure 4.24 and used in the amplitude displacement measurements. The parameters in Table 4.1 were chosen based on the configuration of FMCW used in the original heart and respiration rate measurement of the radar module's manufacturer example. Additional time was put between chirps in order to decrease the bin

size and thus increase the ability to measure small distance displacements. These parameter will most likely form the basis of the FMCW configuration for the final application.

Table 4.1: Frequency modulated continuous wave parameters used for smallest amplitude detection measurements

Start Frequency (GHz)	Idle Time (μs)	ADC Start Time (μs)	Ramp End Time (μs)
77	7	6	107
Frequency Slope (MHz/μs)	Sample Rate (ksps)	Number of Loops	Number of Frames
30	2000	7	200
ADC Samples		Frame Periodicity (ms)	
200		100	

5

Conclusion and Future Work

In this chapter, there will be a conclusion drawn from the radar system operation in the neonatal environment. The conclusion is broken down into three sections. The first section is based on the safety of the application of this system. It focuses on how the modelled environment can be used to implement the system in a safe manner. Next the amplitude detection will be addressed. This is focused on how the characterized operation of the system will translate for a neonatal patient. Both sections focus on how the environment and system influence one another and will be addressed together in the last section of the conclusion where the proof of concept capability is discussed. The final section of this chapter will focus on the recommendations for future work. It will propose additional safety measurements that could be done, potential additions to the amplitude measurement set-up and the upcoming challenges that will be faced in a clinical application.

5.1. Safe Implementation

There are multiple conclusions that can be drawn from the results of the safety aspect of the system focusing on temperature increase caused by millimeter wave radar. The first conclusion is that the maximum temperature increase anticipated is 542mC. This is with a naked skin model that has normal blood perfusion and a power density of 10W/m^2. The maximum output power the radar module is able to produce is 10W/m^2, though a lower power density will most likely reach the neonate due to implications of the Friis Transmission Equation, which details the attenuation of electromagnetic waves from transmitter to receiver based on distance and wavelength.

Another conclusion in regards to the thermal that was built is the change in temperature increase for lower heat transfer coefficients may not translate well with power densities lower than 10W/m^2. The general assumption is that a power density an order of magnitude lower than the initial power density would produce a temperature increase that is an order of magnitude lower than the initial temperature increase. This does not hold for lower heat transfer coefficients. This may be due to the limitations of the model to replicate the skin surface temperature once it comes into contact with hot environments. Usually skin responds by increasing blood flow and sweating to get the heat transfer coefficient higher. Since a neonate does not have these capabilities, the temperature increase results for lower power densities may still be correct. But the final conclusion was to use the 10W/m^2 temperature increase as the limit of the potential temperature increase caused by the radar module.

Another conclusion from the thermal model comes from the heat transfer coefficient calculation. Before validation of the thermal model was completed, the initial heat transfer coefficient calculations did not take into consideration the amount of BSA the maximum output power would cover and assumed it to be the entire neonate's BSA. This caused a heat transfer coefficient to be extremely low, around 1-2W/m^{2}C. After inputting an area for the thermal model heat transfer coefficient that more accurately reflected the antenna radiation pattern, the new heat transfer coefficient resulted in a temperature increased. In the NICU environment, the heat transfer coefficient changed to 5.3W/m^{2}C, so the maximum temperature increase became 0.5C instead of 1.6C.

Lastly, the influence of blood perfusion was shown to match assumptions. With lower blood perfusion, the temperature will increase. With no blood perfusion, the temperature will continuously increase. This is due to the blood's ability to distribute the heat throughout the body to dissipate it. In this case, future research must be done into what actions a doctor would take if lower blood perfusion occurs. If lower blood perfusion means the neonate has sepsis, then it may be more important to a neonatalogist to respond to that issue rather than the temperature increase the radar causes. Still, it may be worth implementing a system that can detect the sepsis and turn off the radar accordingly, which may be beneficial for the doctors and nurses as it could alert them of the sepsis issue as well. As to what counts as low blood perfusion, it may be relative to the radar. If the blood perfusion becomes low enough that the temperature increases rapidly within a few minutes, similarly to the increase in 1C after 10 minutes seen in Figure 4.14, then the amount of blood perfusion that causes this to occur can be considered the baseline for setting an alert.

5.2. Smallest Amplitude Detection

The research done to understand the smallest amplitude change within one bin that a millimeter wave radar module can measure led to a few conclusions. The first was that the radar module and associated FMCW parameters, seen in Table 3.1, have the ability to detect a displacement of 0.01mm within one bin, which may or may not be enough to measure the chest of a neonate. What may be more helpful is the set-up that was created in order to show what displacement measurements are possible. The measurement set-up can show how FMCW parameters manipulate the detection of minuscule amplitude displacements.Using the set-up, more research can be done into what parameters need to be configured and how. Also, it is flexible enough to add different materials and change the materials surrounding the radar module to add more scattering for a more realistic application scenario. Lastly, it can reduce testing time on neonates by predefining FMCW configuration parameters that should yield the best results.

The results also show the influence bin size has on the detection of change in amplitude in one bin. As hypothesized, the smaller the bin size, the easier it is to see small changes in amplitude in one bin because the energy received from the reflections of the object placed in front of the radar module is spread out over multiple bins. The smaller the bin size, the more bins the energy spreads over and the lower amplitude it has in each bin. Using this concept, it is easier to determine what FMCW parameters should be changed and how. Since there are hundreds of thousands of different configurations, there needs to be a place to start. Starting with bin size is a good way to understand what the chirp and frame size should be, from here the slope and start and stop frequencies can be varied in order to produce the best signal to noise ratio for the final application.

5.3. Proof of Concept

The ultimate conclusion of the investigation is that the application of millimeter wave radar can be realized in a NCIU clinical environment in a safe manner. With temperature increase being the only identified hazard, investigation into what the temperature would be in the clinical application has been done. The maximum temperature has been shown to be within temperature variability of a neonate's temperature throughout the day and the lower power density of the actual application has been measured with infrared camera to show it has little effect. The results of these measurements show the lower power densities do little to increase temperature of an adult arm and even a large piece of meat tissue with no blood perfusion. As for the ability of the radar to measure the small changes in amplitude caused by the neonate's heart and lungs on its chest, the conclusion is the potential to measure such small displacements are possible. With an ideal scenario, the radar module could measure the a displacement of 10μm. Further improvements on the current FMCW profile configuration can be done if this is insufficient for measuring neonates due to the already created set-up, but the current FMCW parameters may be enough already. In conclusion, the investigation has shown the radar module used, and millimeter wave radar in general, can be implemented safely to measure neonates without any contact with the patient with the goal to improve their care.

Table 5.1 contains a comparison between the millimeter wave RF sensor proposed in this thesis, represented by the Texas Instrument's IWR1443 (https://www.ti.com/product/IWR1443) that was used in initial thesis

testing, and another on the market sensor that uses sub-millimeter wave frequencies and impulse modulation: Novelda's X4 RF sensor (https://novelda.com/x4-soc.html). Both sensors have benefits for different applications. The FMCW millimeter wave sensor has benefits in having a more complex modulation technique with more flexibility in programming and a higher frequency for smaller amplitude detection. Both the millimeter wave sensor and ultra-wideband sensor are not attenuated by many materials despite metal. The millimeter wave RF sensor requires more operating power and transmits more output power, though that can be brought down in 1dB increments compared to the X4 which can only back off output power in 3dB increments, but the module will be plugged into a wall source instead of being battery operated, so this is not a large drawback. The millimeter wave RF sensor is also larger and most likely more expensive, but the application is within the medical space and both the size and cost are still significantly smaller and more cost effective than most medical devices.

Table 5.1: Defining elements of FMCW Millimeter Wave RF Sensor (TI-IWR1443) versus an Ultra-Wideband RF sensor (Novelda-X4)

Feature	**TI-IWR1443**	**Novelda-X4**
Operating Frequency	76GHz & 60GHz (Millimeter Wave)	sub 10GHz (Ultra-Wideband)
Operating Bandwidth	5GHz	1.5GHz
Modulation Technique	Frequency Modulated Continuous Wave	Impulse Modulation
Maximum Output Power	12dBm	6dBm
Power Consumption	3W	<120mW
Materials Cannot Penetrate	Metal	Metal
Size	108 mm^2 (10.4mm x 10.4mm)	8.58 mm^2 (2.6 mm x 3.3 mm)
Cost	€11.80/1ku	Unspecified

5.4. Contributions

In this section, individual contributions of the author to the thesis work are listed.

- Wrote thermal model code including calculation for heat transfer coefficient and temperature elevation due to millimeter wave radio frequencies
- Simulated and characterized the evaluation module antenna using Microwave CST and characterization code and method cited in Alonso et. al[49]
- Built obstructive materials measurement set up and ran multiple test iterations to characterize NICU application materials attenuation properties
- Helped build validation set up of thermal model and run validation measurements
- Analyzed validation of thermal model results for modification of thermal model code
- Built set up for measuring heart and respiration rate of adults and used trail and error to configure an FMCW configuration for neonatal measurements
- Wrote signal processing code in Matlab to analyze heart and respiration rate data measured from multiple adults
- Built set up for measuring smallest amplitude detection and measured multiple amplitudes
- Proposed distortion measurement for smallest amplitude detection and wrote Matlab code to demonstrate potential
- Discussed second measurement option, amplitude of first FFT, for measurement of smallest amplitude detection and wrote Matlab code to demonstrate potential
- Analyzed both smallest amplitude potential proposal for conclusion on smallest amplitude detection

5.5. Recommendations for Future Work

In this section, the conclusion is continued upon. Multiple improvements are identified that could provide more information on the application safety and how to achieve a higher signal to noise ratio in the clinical environment. Then it also identifies potential problems and pitfalls of the application in the clinical space, the next step in the medical device creation stage, and their associated proposed solutions.

5.5.1. Further Steps to Show Safe Implementation

It is shown the maximum limit that the temperature increase could potentially have, but there are two things that must be addressed before completely proving the application of FMCW millimeter wave by the radar module is safe. First, the potential focal properties of the curved incubator hood must be addressed. The obstructive materials measurement points to the potential of the plastic to affect the gain pattern and thus the temperature distribution and increase on the neonate inside the incubator. The proposal is to measure the continuous wave temperature increase again with the set-up described in Chapter 4 outside the incubator with and without the hood and at different hood angles. The relative output power and temperature increase change can be calculated. Knowing the affect the hood curvature has on the relative output power and temperature increase can give the model a compensation number to be built in.

Another issue is it is still unknown whether FMCW millimeter wave would cause the maximum temperature increase calculated. The proposed solution to solve this unknown is to find the ideal configuration of the FMCW radar in the neonatal application. Then, re-create the measurement of temperature increase using the same infrared thermal camera used in the Chapter 4, but, instead of using continuous wave, use the FMCW parameters decided upon for the final application. In order to gather the ideal FMCW configuration, the initial measurements done on the neonate will involve a temperature sensor placed on the skin to confirm the safe application modelled. Once the FMCW parameters are found and the temperature increase is shown to be within safe limits, then the temperature sensor can be removed for further testing.

5.5.2. Realistic Amplitude Detection Set-Up

One flaw in the measurement of the amplitude difference within one bin is the current measurement set-up. It is the most ideal scenario: absorbent materials surround the radar module and a metal plate is placed in front of it in a close range. Measuring the smallest amplitude detected by the radar module in the most ideal scenario most likely does not translate well in a NICU setting. In a clinical scenario, there are more disturbances and scattering materials placed around the radar module and the neonate is not a metal plate but a lossy substance. That is why a proposal for a measurement set-up that is more realistic is added into future work. The current measurement system can be improved upon to better build a FMCW profile that will work within a NICU scenario.

Improvements to the current smallest amplitude detection set-up can be done in a multitude of ways. First, the material measured can be a lossy one. The point would be to replace the metal plate with materials that have worse reflective properties. Another improvement would be to place less absorbent material around the radar module to increase scattering. Also, placing incubator plastic in between the radar module and the material being measured. This would give more scattering effects and make the measurement set-up reflect the application better. Finally, the material to be measured could be placed farther away more similar to the distance the radar module will have between it and the neonate. Once these improvements are done, the investigation into bin size and its influence on the small amplitude changes can be continued.

One recommendation would be to turn the measurement around on itself and try to measure, quantitatively, the smallest displacement a neonate's chest has. It would require a way to map the results of measuring the neonate's chest with the results of the amplitude detection set-up. For example, if a neonate's chest FFT results are similar to the amplitude detection FFT results of 0.1mm, then it could be said the neonate's chest moves 0.1mm. This would be helpful information going into the future because it could potentially provide a table of chest displacement mapped to neonatal size. That could be used to determine if the radar module will be successful in measuring heart and respiration rate dependent on the neonate's weight and length.

5.5.3. Clinical Application Challenges

These findings, validation and analysis of results point to the conclusion that this system is safe and capable. So, the next step will be to implement the system in a NICU environment. First, the FMCW parameters must be chosen for the ideal measurement. This will be based on heat increase and amplitude measurement. Once that is done, then the proof of concept can be shown to work. Next, the application environment must be addressed. In a clinical application, many different people will be within the radar measurement space. This includes parents and nurses. One potential problem could be nurses and/or parents blocking the signal. This will have to come down to the signal processing system determining what is the difference between the signal being blocked by a closer object or the neonate not breathing or their heart not beating. One proposed solution would be to have the system, once it has detected that the current range bin is not vibrating, it searches the rest of the array of chirps and bins to see if there is a bin with a large amplitude. This would indicate that an object is at a different position and thus it is being blocked. If the range bin seems to not have changed, then there is something wrong and an alarm will sound.

Another issue is whether the nurse or parents' heart rate will be measured instead of the neonate's because the amplitude is higher. The proposed solution for this is to reduce the bin size. Since the neonate will not be moving around, since its muscles are still growing, the bin size can be very small with the confidence that the neonate will not move between bins. Since the nurse and parents will probably move between bins, their heart and respiration rates will not be continuously measured meaning they will get lost in the noise. Another important note is that neonate's heart and respiration rate is much higher than an adult's. And there is bandpass filter at these frequencies. Thus, the heart and respiration rate frequencies of an adult will be filtered out.

Lastly, the goal will be to create a device that can be used within a clinical space. It will require a qualitative and quantitative method because input from doctors and nurses on the best implementation they would perceive the medical device to be is paramount. And so, this goal will be broken into two parts. First, it starts with a qualitative approach then moves to a quantitative one. In order to understand what is most important to a nurse or doctor when caring for a neonate, a survey and discussion with them must be done. Putting together a list of what is necessary and what would be ideal can help make the plan for the next part: quantitative. There are many pieces that need to be put together along with the radar to get it to work in the NICU and even within those pieces are many different options of which to choose. The qualitative approach will help guide those decisions, but the quantitative approach will require additional understanding on the engineer's part to choose the best configuration. For example, a device that has a screen with real-time information on the neonate's vital signs may be requested. This will require a large amount of work into creating a new system that can output data in real time and display it on a screen. There are many recommendations for creating this system, but the first and foremost will be to move on from the evaluation module since that is beyond its capabilities if the goal is to have a compact and unobtrusive shape and size.

A

Matlab Code

Appendix A contains the Matlab code for all chapters.

A.1. Chapter 2 Matlab Code

Listing A.1: Heat transfer coefficient calculation

```
%Calculate the heat transfer coefficients of neonates in the NICU by
% using the paper 'Effect of posture on the thermal efficiency of a
% plastic bag wrapping in neonate: Assessment using a thermal
%   sweating    mannequin' written by Belghazi

clear
%clc

%Definitions
%hE = [W/m^2/mb] evaporative heat transfer coefficient, dependent on
    air velocity
%hC = [W/m^2/C] convective heat transfer coefficient

%Inputs
neonateWeight = 0.9; %[kg] weight of neonate
neonateLength = 0.1; %[m] length (height) of neonate

%Variables
neonateWidth = 0.07; %[m] width of neonate, taken as constant
neonateDepth = 0.01; %[m] depth of neonate, taken as constant
ambientTemp = 33; %[C] incubator air temperature
skinTemp = 35.7; %[C] mean surface temperature from different local
    surface temps
ambientTempAct = 35;
skinTempAct = 37;
v = 19.017e-6; %[kg/m*s] kinematic viscosity of air/water:
    Thermophysical and transport properties of humid air at temperature
     range between 0 and 100 C
g = 9.81;%[m/s^2] gravitational acceleration
totalHeatLoss = 13.8; %[W] taken from results of paper
radiantTemp = 1.43+0.761*ambientTemp+0.169*23; %[C] radiant temperature
     of neonate, taken from Energy balance in the newborn baby
radiantTempAct = 1.43+0.761*ambientTempAct+0.169*23;
mattressTemp = ambientTemp; %[C] temperature of mattress
```

```
relativeHumidity = 80; %[%]
dryHeatLoss = 7.8; %[W] heat loss due to non-evaporative values
convecPercent = 2; %[%] percentage of heat loss due to convective,
    between 1-3%
k = 0.37; %[W/m/C]thermal conductivity of skin
skinThickness = 1;%[mm] thickness of skin

%Calculate characteristic dimension, depends on geometrical form
BSA = 0.2157*(neonateWeight^0.425)*(neonateLength^0.725); %[m^2] body
    surface area of neonate
%BSA = (0.16*0.25);
%Calculate areas for different heat transfer coefficients
areaK = neonateLength*neonateWidth; %conductive heat transfer area,
    cross sectional area of neonate
areaC = BSA/2; %convective heat transfer area, half of body surface
    area (part facing upwards)
areaR = (BSA/2)*1.5; %radiative heat transfer area, entire body is
    radiating
areaW = (BSA/2)*1.5;

syms hCsolve
%Calculate convective heat coefficient
% D = 4*((neonateLength*neonateWidth*neonateDepth)/areaW); %[
    dimensionless] taken from: Thermal Dosimetry and Treatment Planning
    , page 12
% Nu = hCsolve*(D/k);
% Gr = g/(v^2*ambientTemp);
% eqn1 = Nu == a*Gr^b;
% hC = solve (eqn1, hCsolve);
%Calculate convective heat exchange
C = (convecPercent/100)*dryHeatLoss;
eqn1 = C == hCsolve*areaC*(skinTemp-ambientTemp);
hC = round(double(vpa(solve(eqn1, hCsolve),5))*1e3)/1e3; %[W/(m^2*C)]

%Calculate evaporative heat transfer coefficient using convective heat
%transfer coefficient based on Lewis equation
hE = 1.67*hC; %[W/(m^2*mb)] (mb == millibar)

syms hKsolve hRsolve

%Calculate conductive heat exchange
% Due to the small body surface area in contact with the mattress, heat
% conduction is considered insignificant
K = hKsolve*areaK*(mattressTemp-skinTemp);

%Calculate evaporative heat loss
syms VaporDiff hcMix
eqn3 = 6.09 == hE*areaW*VaporDiff;
solveVaporDiff = double(vpa(solve (eqn3, VaporDiff),5));
initialRH = 0.5;
satAirVapor = 65.6; %taken from database
airVapor = initialRH*satAirVapor;
skinVapor = solveVaporDiff + airVapor;
totalVaporSkin = skinVapor/0.3; %wettedness of 30% in study
%Calculate water vapor difference
```

```
ratio = satAirVapor/totalVaporSkin; %ratio of saturated air and skin
    vapor
skinVaporNew = (1/ratio)*skinVapor;
waterVaporDifference = skinVaporNew-(satAirVapor*(relativeHumidity/100)
    );

%E = 6.09*(0.4/(relativeHumidity/100));

skinThickness = skinThickness/1e3;

difference = skinTemp-ambientTemp;
ratioC = difference/(skinTempAct-ambientTempAct);
hCnew = hC/ratioC;
newC = hCnew*areaC*(skinTempAct-ambientTempAct);
hE = 1.67*hCnew; %[W/(m^2*mb)] (mb == millibar)
E = hE*areaW*waterVaporDifference;
hC = hCnew;
hE = E/(areaW*solveVaporDiff);
heatLossR = (newC/(convecPercent/100))*(1-(convecPercent/100));
%Calculate convective heat coefficient
eqn4 = heatLossR == hRsolve*areaR*(skinTempAct-radiantTempAct);
hR = double(vpa(solve (eqn4, hRsolve),5));

%hArray = [hC hE hR]

h = (1/((1/(hC*areaC)) + (skinThickness/(k*areaC)) + (1/(hR*areaR)) + (
    skinThickness/(k*areaR)) + (1/(hE*areaW))+ (skinThickness/(k*areaW)
    )))/(BSA/5.5)
```

Listing A.2: Thermal model based on Ting[29]

```
%RF Thermal Modeling based on the paper by Ting Wu (2015) that takes
% into consideration the effect of clothing on heating as well as the
% distribution of heat inside the bone, is able to include heat
% transfer coefficient.

clear
%clc
figure
%Variables
%inputs
theta = 0; % [degrees] incident angle, highest output power at 78.5
frequency = 80E9; %[Hz], frequency that is being studied
radiatedPD = [50 10 1 0.1 0.01]; %[W/m^2]
tissueThickness = [1 3 31]/1e3;% take out bone 0]; %[mm] tissue
    thickness [skin, fat, muscle, bone]
hamb = 7; %[W/m^2/C] heat transfer coefficient from outer skin to air
airTemp = 23; %[C]
w = [106 33 37];%[mL/kg/min] blood perfusion

%tissue properties: skin, SAT, muscle, bone, blood
bloodTemp = 37; %[C], generally taken as body temp in calculation
k = [0.37 0.21 0.49];%[W/m/C]thermal conductivity, 0.52 blood
p = [1109 911 1090 1908 1050]; %[kg/m^3] mass density
c = [3391 2348 3421 1313 3617]; %[J/kg/C] specific heat capacity
z = [tissueThickness(1)...
    tissueThickness(1)+tissueThickness(2)...
```

```
    tissueThickness(1)+tissueThickness(2)+tissueThickness(3)]; %[mm]
       distance into tissue
tissueDepth = (0:1:35)/1e3; %[mm] tissue depth

%signal properties
speedLight = 3e8;
wavelength = speedLight/frequency;
e = [6.40 3.95 10.17]; %60GHz = [7.98 4.40 12.86]; %[F/m]
sigma = [38.38 9.66 58.58];%60GHz = [36.38 8.39 52.80]; %[Siemens/meter
   ]
omega = 2*pi*frequency;%[rad/s] angular frequency

%given constants
e0 = 8.85E-12; %[F/m] permittivity of free space
k0 = omega/speedLight;%omega/3e8; %propogation constant of free space
u = 12.57E-7;%[H/m] magnetic permeability (assume equal to vacuum)

%arrays
TempElevAtTissue = ones(length(tissueThickness),length(tissueDepth));

%Calculate complex permitivty
eImag = sigma./omega;
eComplex = (e.*e0-1i.*eImag); %given from 2013 paper

%Calculations for complex numbers (for calculating reflection coeff)
eImag = sigma./(omega.*e0);
eComplexAdj = (e-1i.*eImag); %given from 2015 paper

%calculate intrinsic impedance of tissue
eta0 = 120*pi; %intrinsic impedance of free space
eta = sqrt(u./eComplex);

%Extend arrays based on tissue type (for future use)
zDepthSkin = find(abs((tissueDepth-z(1)))<0.0001);
zDepthFat = find(abs((tissueDepth-z(2)))<0.00001);
zDepthMuscle = find(abs((tissueDepth-z(3)))<0.00001);
sigmaOverArea = [repmat(sigma(1),1,1)...
    repmat(sigma(2),1,zDepthFat-zDepthSkin)...
    repmat(sigma(3),1,zDepthMuscle-zDepthFat+1)];
kOverArea = [repmat(k(1),1,1)...
    repmat(k(2),1,zDepthFat-zDepthSkin)...
    repmat(k(3),1,zDepthMuscle-zDepthFat+1)];

%Calculate k for electric and magnetic field calculations (not thermal
%conductivity)
kEM = omega.*sqrt(u.*eComplex);
% extend kEM array
kEMOverArea = [repmat(kEM(1),1,1)...
     repmat(kEM(2),1,zDepthFat-zDepthSkin)...
     repmat(kEM(3),1,zDepthMuscle-zDepthFat+1)];
% use kEM to calculate beta and alpha
beta = real(kEMOverArea);
alpha = -imag(kEMOverArea);

%Power reflection and transmission coefficient calculation
parallelR = abs((-eComplexAdj.*cosd(theta)+sqrt(eComplexAdj-sind(theta)
```

```
    ^2))...
     ./(eComplexAdj.*cosd(theta)+sqrt(eComplexAdj-sind(theta)^2)));
reflecCoeffpara = parallelR.^2;
transCoeffpara = 1-parallelR.^2;

%Calculate electric and magnetic field
%calculate power transmitted into tissue
for counter =1:length(radiatedPD)
    transmittedPow = transCoeffpara(1)*radiatedPD(counter);
    %calculate incident wave
    syms E0
    E0Rep = [E0 0 0];
    H0Rep = [0 E0/eta0 0];
    CrossResult0 = cross(E0Rep,conj(H0Rep)');
    eqn1 = transmittedPow == CrossResult0(3);
    E_naught = vpa(solve(eqn1,E0(1)),3);
    %calculate subsequent electric fields by setting magnetic and
       electric
    %fields equal to each other
    syms Epos1 Epos2 Epos3 Eneg1 Eneg2 Eneg3
    E1AtZ1 = Epos1*exp(-1i*kEM(1)*z(1))+Eneg1*exp(1i*kEM(1)*z(1));
    E2AtZ1 = Epos2*exp(-1i*kEM(2)*z(1))+Eneg2*exp(1i*kEM(2)*z(1));
    H1AtZ1 = Epos1*exp(-1i*kEM(1)*z(1))/eta(1)-Eneg1*exp(1i*kEM(1)*z(1)
       )/eta(1);
    H2AtZ1 = Epos2*exp(-1i*kEM(2)*z(1))/eta(2)-Eneg2*exp(1i*kEM(2)*z(1)
       )/eta(2);

    E2AtZ2 = Epos2*exp(-1i*kEM(2)*z(2))+Eneg2*exp(1i*kEM(2)*z(2));
    E3AtZ2 = Epos3*exp(-1i*kEM(3)*z(2))+Eneg3*exp(1i*kEM(3)*z(2));
    H2AtZ2 = Epos2*exp(-1i*kEM(2)*z(2))/eta(2)-Eneg2*exp(1i*kEM(2)*z(2)
       )/eta(2);
    H3AtZ2 = Epos3*exp(-1i*kEM(3)*z(2))/eta(3)-Eneg3*exp(1i*kEM(3)*z(2)
       )/eta(3);

    eqn2 = Epos1 == E_naught(1);
    eqn3 = H1AtZ1 == H2AtZ1;
    eqn4 = E1AtZ1 == E2AtZ1;
    eqn5 = H2AtZ2 == H3AtZ2;
    eqn6 = E2AtZ2 == E3AtZ2;
    eqn7 = Eneg3 == 0; %set to be equal to 0 (from 2015 paper)

    solution = solve([eqn2 eqn3 eqn4 eqn5 eqn6 eqn7], [Epos1 Epos2
       Epos3 Eneg1 Eneg2 Eneg3]);

    Epos(1) = double(vpa(solution.Epos1(1),5));
    Eneg(1) = double(vpa(solution.Eneg1(1),5));
    Epos(2) = double(vpa(solution.Epos2(1),5));
    Eneg(2) = double(vpa(solution.Eneg2(1),5));
    Epos(3) = double(vpa(solution.Epos3(1),5));
    Eneg(3) = 0;
    %extend electric field array
    EposNew = [repmat(Epos(1),1,1)...
        repmat(Epos(2),1,zDepthFat-zDepthSkin)...
        repmat(Epos(3),1,zDepthMuscle-zDepthFat+1)];
    EnegNew = [repmat(Eneg(1),1,1)...
        repmat(Eneg(2),1,zDepthFat-zDepthSkin)...
```

```
    repmat(Eneg(3),1,zDepthMuscle-zDepthFat+1)];
Epos = EposNew;
Eneg = EnegNew;
%calculate complex conjudate
Ecomplex = Epos.*conj(Eneg);
% use complex conjugate to find ui and vi
ui = real(Ecomplex);
vi = imag(Ecomplex);

%Calculate the heat transfer coefficient based on blood
hb = ((p(5)*w(1:end)*c(5)/1e3)/60);
%extend array
hbOverArea = [repmat(hb(1),1,1)...
    repmat(hb(2),1,zDepthFat-zDepthSkin)...
    repmat(hb(3),1,zDepthMuscle-zDepthFat+1)];

%Calculate Ca and Cb at the skin by first building the boundary
   equation
% calculation done once for the initial skin layer
syms Ca Cb phi(x) zeta(x) xi(x) psi(x) x
%create body temperature equation
An = [1620 300 480]; %metabolic heat production
bn = [9100 1700 2700]; %blood flow [W/m3C]
BodyTemp0 = 35;%[C]
bodyDiff0 = 227.027;
BodyTempEq = BodyTemp0*cosh(sqrt(bn./k)*x)...
    + bodyDiff0*(1./(sqrt(bn./k))).*sinh(sqrt(bn./k)*x)...
    + (bloodTemp + (An./bn)).*(1-cosh(sqrt(bn./k)*x));
BodyTemp = BodyTempEq(1);
% set-up different equations given in 2015 paper based on x (tissue
    depth)
phi(x) = Ca*exp(-sqrt(hbOverArea(1)/kOverArea(1))*x)+...
    Cb*exp(sqrt(hbOverArea(1)/kOverArea(1))*x);
zeta(x) = -(sigmaOverArea(1)/(2*(4*alpha(1)^2*kOverArea(1)-
   hbOverArea(1))))*...
    abs(Epos(1))^2*exp(-2*alpha(1)*x);
xi(x) = -(sigmaOverArea(1)/(2*(4*alpha(1)^2*kOverArea(1)-hbOverArea
   (1))))*...
    abs(Eneg(1))^2*exp(2*alpha(1)*x);
psi(x) = (sigmaOverArea(1)/(2*(4*beta(1)^2*kOverArea(1)+hbOverArea
   (1))))*...
    (ui(1)*cos(2*beta(1)*x)+vi(1)*sin(2*beta(1)*x));
tempElev = phi(x) + zeta(x) + xi(x) + psi(x); %add together
% get differential for the boundary equation
diffTempElevz0 = diff(BodyTemp+tempElev,x);
% plug in the blood temperature as the body temperature with a
   temperature
% elevation decrease, then subtract the air temperature
diffTempElevz0 = subs(diffTempElevz0,x,0);
tempElevz0 = subs(tempElev,x,0);
eqn8 = k(1)*diffTempElevz0 == hamb*((subs(BodyTemp,x,0)+tempElevz0)
   -airTemp); %solve first boundary equation
% extract the Ca and Cb values
solution = solve(eqn8, [Ca Cb]);
solCa = double(vpa(solution.Ca,5));
solCb = double(vpa(solution.Cb,5));
```

```
% temperature gradient at the surface (of the order of hundreds of
    C  per
% meter) (sanity check)
TemperatureGradientAtSurface = vpa(subs(subs(diffTempElevz0,Ca,
    solCa),Cb,solCb),5);
TempIncreaseAtSurface = (((TemperatureGradientAtSurface*k(1))/hamb)
    +airTemp)-subs(BodyTemp,x,0);
%Calculate dissipation of heat into the tissue for rest of body
TempElevAtZ1 = subs(vpa(subs(subs(tempElev,Ca,solCa),Cb,solCb),5),x
    ,z(1));
syms x CaPos CbPos phiPos zetaPos xiPos psiPos
iterate = 2;
for count = 2:length(tissueDepth)-2
    % divide tissue depth into boundary and non-boundary sections
    boundaryLayerLoc = [tissueThickness(1)*1e3 + 1 tissueThickness
        (1)*1e3 + tissueThickness(2)*1e3 + 1];

    if tissueThickness(end) ~= 0
        boundaryLayerLoc = [boundaryLayerLoc tissueThickness(1)*1e3
            + tissueThickness(2)*1e3 + tissueThickness(3)*1e3 +
           1];
    end

    if boundaryLayerLoc(1) ~= 2
        boundaryLayerLoc = [2 boundaryLayerLoc];
    end
    %boundaryLayerLoc = [2 3];

    if ismember(count,boundaryLayerLoc)%only apply boundary
        conditions at interface
        % symbols divided into positive (current count) and
            negative
        % (previous tissue), creating symbols again clears them of
            previous
        % value

        % seperate counts based on current or previous layer
        countp = count;
        countn = count-1;
        % create delta temperature equations for both interfaces (
            previous
        % and current tissue layer)

        phiPos = CaPos*exp(-sqrt(hbOverArea(countp)/kOverArea(
            countp))*x)+...
            CbPos*exp(sqrt(hbOverArea(countp)/kOverArea(countp))*x)
                ;
        zetaPos = -(sigmaOverArea(countp)/(2*(4*alpha(countp)^2*
            kOverArea(countp)-hbOverArea(countp))))*...
            abs(Epos(countp))^2*exp(-2*alpha(countp)*x);
        xiPos = -(sigmaOverArea(countp)/(2*(4*alpha(countp)^2*
            kOverArea(countp)-hbOverArea(countp))))*...
            abs(Eneg(countp))^2*exp(2*alpha(countp)*x);
        psiPos = (sigmaOverArea(countp)/(2*(4*beta(countp)^2*
            kOverArea(countp)+hbOverArea(countp))))*...
            (ui(countp)*cos(2*beta(countp)*x)+vi(countp)*sin(2*beta
```

```
                (countp)*x));
            tempElevPos = phiPos + zetaPos + xiPos + psiPos;

            diffTempElevzPos = diff(tempElevPos,x); %get positive
                differential

            if count == 2
                tempElevNeg1 = TempIncreaseAtSurface;
                diffTempElevzNeg = vpa(subs(subs(subs(diff(tempElevPos,
                    x),CaPos,solCa),CbPos,solCb),x,tissueDepth(countn))
                    ,5);
            else
                tempElevNeg1 = TempElevAtTissue2(countp);
                diffTempElevzNeg = vpa(subs(subs(subs(diff(tempElevPos,
                    x),CaPos,solCaPos),CbPos,solCbPos),x,tissueDepth(
                    countp)),5);
            end
            % apply two boundary conditions
            eqn9 = kOverArea(countn)*diffTempElevzNeg == kOverArea(
                countp)*diffTempElevzPos;
            eqn10 = tempElevPos == tempElevNeg1; %remove previous
                temperature increase
            % get Ca and Cb values for current and previous layer with
                both
            % equations
            solution = solve ([eqn9 eqn10], [CaPos CbPos]);
            % only use current count values for calculating temp
                increase
            % recalculate the multiple equations with Ca and Cb solved
            % only solve for current temperature increase at current
                tissue
            % level
            solCaPos = double(vpa(subs(solution.CaPos,x,tissueDepth(
                countp)),5));
            solCbPos = double(vpa(subs(solution.CbPos,x,tissueDepth(
                countp)),5));

            if count == 2
                TempElevAtTissue2 = subs(vpa(subs(subs(tempElevPos,
                    CaPos,solCaPos),CbPos,solCbPos),5),x,tissueDepth);
                TempElevAtTissue(iterate,:) = subs(vpa(subs(subs(
                    tempElevPos,CaPos,solCaPos),CbPos,solCbPos),5),x,
                    tissueDepth);
            else
                TempElevAtTissue3 = subs(vpa(subs(subs(tempElevPos,
                    CaPos,solCaPos),CbPos,solCbPos),5),x,tissueDepth);
                TempElevAtTissue(iterate,:) = subs(vpa(subs(subs(
                    tempElevPos,CaPos,solCaPos),CbPos,solCbPos),5),x,
                    tissueDepth);
            end
            iterate = iterate + 1;
        end
    end

    %Plot
    color = {'r','b','m','g','k'};
```

```
    mark = {'^','s','*','o','d'};
    TemperatureArray = [TempIncreaseAtSurface TempElevAtTissue(2,3:5)
       TempElevAtTissue(3,6:end) 10^-5];
    [row, col] = find(TemperatureArray<0);
    if ~isempty(col)
        TemperatureArray(TemperatureArray<0) = 0;
        TemperatureArray(end) = 0;
        firstNeg = min(col);
        TemperatureArray(row,firstNeg) = 10^-5;
    end
    hold on
    plot(tissueDepth*1e3,TemperatureArray*1e3,'Color',color{counter},'
       Marker',mark{counter},'LineWidth',2);

end
title('Steady State Temperature Elevation at 80GHz');
xlabel('Depth Into Model (mm)')
ylabel('Temperature Elevation (mC)')
set(gca, 'YScale', 'log')
set(gca,'Fontsize',20);
ylim([10^-2 10^4])
xlim([0 35]);
legendCell = cellstr(num2str(radiatedPD', '%gW/m^2'));
legend(legendCell);
grid on
```

Listing A.3: Thermal model based on Ziskin[24]

```
%Thermal model based on Ziskin paper
clear
clc
% Variables
%
%table of skin penetration of each frequency
bandwidth = 3840; %bandwidth (MHz)
frequencySlope = 120; %slope (MHz/us)
frequencyStart = 42; %starting frequency (GHz)
frequencyStop = 80.84; %ending frequency (GHz)
distanceSource = 1; %distance from source (m)
currDutyCycle = 0.9216; %duty cycle currently used in chirp
   configuration
timeArray = 0:1:0.1; %array to plot the tau constant against
omega = 2*pi*frequencyStart*1E9;
naughtEpsilon = 8.85E-12;
iEpsilonInfi = [2.96 4.0 2.5 4.0]; %SC E+D Fat Muscle
iDeltaEpsilon = [1.5 32.4 4.0 50]; %SC E+D Fat Muscle
iSigma = [0 1.4 0.01 0.1]; %SC E+D Fat Muscle
tau = [6.9 6.9 7.96 7.23]*1E-12; %SC E+D Fat Muscle, in seconds
distance = [0.015 1.45 1 1]; %thickness of layer (mm), fat ranges from
   1-6
bloodTemp = [37 39 37.9 38.6]; %blood temperature in C
bloodFlow = [0 1.4E-3 3E-4 5.33E-4]; %blood flow for dermis ranges from
    0.3to12E-3 (1.4E-3 for abdomen)
bloodDensity = 1060; %density of blood (kg/m^3), taken from Cutnell,
   John & Johnson, Kenneth. Physics, Fourth Edition. Wiley, 1998: 308.
bloodSpecificHeat = 3617; %specific heat of blood (J/kg/ C ), taken
   from https://itis.swiss/virtual-population/tissue-properties/
```

```
    database/heat-capacity/
ambientTemp = 22; %ambient temperature in celsius
skinTemp = 35.2; %starting temp for fat thickness of 2mm
tissueTemp = [skinTemp skinTemp-1.4 skinTemp-2.6 skinTemp-4.2];
pC = [4.18E6 3.76E6 1.95E6 3.95E6]; %volumetric heat capacity of tissue
delta = 0.00062182; %0.00041289 for 77GHz, penetration energy depth
    into skin (m), taken from: http://niremf.ifac.cnr.it/tissprop/
    htmlclie/htmlclie.php
transmitPowerdBm = 12; %output power in dBm
transmitPowerW = 1*(10^(transmitPowerdBm/10))/1000; %output power in
    watts
surfaceArea = 0.107; %illuminated area in cm^2
naughtI = transmitPowerW/(surfaceArea/10000);  %incident power density
    (W/m^2)
naughtI = 200;
R = 0.4; %power reflection coefficient, taken from: The Human Body and
    Millimeter-Wave Wireless Communication Systems: Interactions and
    Implications
tissueThickness = [0.1 1.5 8 25]; %tissue thickness (mm)
z = [tissueThickness(1) tissueThickness(1)+tissueThickness(2)
    tissueThickness(1)+tissueThickness(2)+tissueThickness(3)
    tissueThickness(4)]; %distance into tissue(mm)
k = [0.32 0.32 0.18 0.43]; %Thermal conductivity of the tissue,
    dependent of blood flow
tissueDepth = 0:0.1:tissueThickness(4); %tissue depth in mm
beta = 975; %proportionality constant for blood flow, (ml/(s*ml))^-1
h = 8.48; %environmental heat transfer coefficient [W/(m^2 * K)]
%1 layer model variables
q = [114 114 84 80]; %(W/m^2), power into top surface of layer
R1 = [7.8 7.8 16.7 14.7]; %(mm) characteristic distance over which
    blood perfusion smooths out the temperature increase
muscleTemp = [4.1 4.1 3.6 2.7]; %(C) temperature into the top of the
    tissue layer,

%Permitivity of each tissue layer (Debye equation)
iEpsilonS = iDeltaEpsilon + iEpsilonInfi;
iEpsilon = iEpsilonInfi + (iDeltaEpsilon/(1+1i*omega*tau))...
    + (iSigma/(1i*omega*naughtEpsilon));

%Heat transfer of each tissue layer to predict temperature increase
zDepthSC = find(abs((tissueDepth-z(1)))<0.01);
zDepthSkin = find(abs((tissueDepth-z(2)))<0.001);
zDepthFat = find(abs((tissueDepth-z(3)))<0.001);
zDepthMuscle = length(tissueDepth);
kOverArea = [repmat(k(1),1,zDepthSC) repmat(k(2),1,zDepthSkin-zDepthSC)
    ...
    repmat(k(3),1,zDepthFat-zDepthSkin)...
    repmat(k(4),1,zDepthMuscle-zDepthFat)];
tissueTempOverArea = [repmat(tissueTemp(1),1,zDepthSC)...
    repmat(tissueTemp(2),1,zDepthSkin-zDepthSC)...
    repmat(tissueTemp(3),1,zDepthFat-zDepthSkin)...
    repmat(tissueTemp(4),1,zDepthMuscle-zDepthFat)];
bloodFlowOverArea = [repmat(bloodFlow(1),1,zDepthSC)...
    repmat(bloodFlow(2),1,zDepthSkin-zDepthSC)...
    repmat(bloodFlow(3),1,zDepthFat-zDepthSkin)...
    repmat(bloodFlow(4),1,zDepthMuscle-zDepthFat)];
```

```
bloodTempOverArea = [repmat(bloodTemp(1),1,zDepthSC)...
    repmat(bloodTemp(2),1,zDepthSkin-zDepthSC)...
    repmat(bloodTemp(3),1,zDepthFat-zDepthSkin)...
    repmat(bloodTemp(4),1,zDepthMuscle-zDepthFat)];
pCOverArea = [repmat(pC(1),1,zDepthSC)...
    repmat(pC(2),1,zDepthSkin-zDepthSC)...
    repmat(pC(3),1,zDepthFat-zDepthSkin)...
    repmat(pC(4),1,zDepthMuscle-zDepthFat)];
qOverArea = [repmat(q(1),1,zDepthSC)...
    repmat(q(2),1,zDepthSkin-zDepthSC)...
    repmat(q(3),1,zDepthFat-zDepthSkin)...
    repmat(q(4),1,zDepthMuscle-zDepthFat)];
R1OverArea = [repmat(R1(1),1,zDepthSC)...
    repmat(R1(2),1,zDepthSkin-zDepthSC)...
    repmat(R1(3),1,zDepthFat-zDepthSkin)...
    repmat(R1(4),1,zDepthMuscle-zDepthFat)];
muscleTempOverArea = [repmat(muscleTemp(1),1,zDepthSC)...
    repmat(muscleTemp(2),1,zDepthSkin-zDepthSC)...
    repmat(muscleTemp(3),1,zDepthFat-zDepthSkin)...
    repmat(muscleTemp(4),1,zDepthMuscle-zDepthFat)];

%1 layer model, epidermis and dermis are combined together (to find
   skin
%temperature increase for 4 layer model)
%R1 = sqrt(k)/sqrt(p*Ct*BF);
thermalResistance = tissueThickness/k;
netThermalResistance = sum(thermalResistance);
effThermalResistance = [0.005 0.005 0.01 0.03];
oneLayerTemp = round(q(1).*(R1(1)/1000)./k(1),2);
%oneLayerTemp1 = q/sqrt(p.*k*BF*C);

%rate of heat deposition per unit volume from mmwave exposure (W/m^3)
Q_z = ((2*(1-R))/delta)*naughtI*exp(-2*(tissueDepth/1000)/delta);
Q_z(zDepthFat:end) = 0;
lambda = bloodFlowOverArea.*pCOverArea./kOverArea;
deltaTemp = zeros(1,zDepthMuscle);
deltaTemp(1) = oneLayerTemp-bloodTempOverArea(1);
currTemp = zeros(1,zDepthMuscle);
currTemp(1) = oneLayerTemp;
newDeltaTemp = deltaTemp(1);

for i=1:zDepthMuscle
    heatTransfer = lambda(i)*newDeltaTemp - Q_z(i)/kOverArea(i);
    deltaTemp(i+1) = currTemp(i)*heatTransfer*(tissueDepth(i)/1000)*...
        (surfaceArea/10000);
    currTemp(i+1) = currTemp(i)+deltaTemp(i+1);
    newDeltaTemp = currTemp(i+1)-bloodTempOverArea(i);
end

%4 layer and 3 layer model plots
threeLayerDistance = [distance(1) distance(2) distance(3) distance(4);
   ...
    distance(1) distance(2) distance(3)+distance(4) 0];
b = barh(threeLayerDistance, 'stacked');
yticklabels({'4 Layer Model','3 Layer Model'})
legend({'Epidermis','Dermis','Fat','Muscle'})
```

```
b(1).FaceColor = [0 0.4470 0.7410];
b(2).FaceColor = [0.9 0.7 0.5];
b(3).FaceColor = [0.9290 0.6940 0.1250];
b(4).FaceColor = [0.6350 0.0780 0.1840];

%plot temperature over tissue thickness for 4 layer model
plot(tissueDepth,currTemp(2:end))
epidermis = [0 0;0 oneLayerTemp; z(1) oneLayerTemp; z(1) 0];
dermis = [z(1) 0;z(1) oneLayerTemp; z(2) oneLayerTemp; z(2) 0];
fat = [z(2) 0;z(2) oneLayerTemp; z(3) oneLayerTemp; z(3) 0];
muscle = [z(3) 0;z(3) oneLayerTemp; z(4) oneLayerTemp; z(4) 0];
f = [1 2 3 4];
patch('Faces',f,'Vertices',epidermis,'FaceColor',[0 0.4470 0.7410],...
    'FaceAlpha',.35,'linestyle','none')
patch('Faces',f,'Vertices',dermis,'FaceColor',[0.9 0.7 0.5],...
    'FaceAlpha',.35,'linestyle','none')
patch('Faces',f,'Vertices',fat,'FaceColor',[0.9290 0.6940 0.1250],...
    'FaceAlpha',.35,'linestyle','none')
patch('Faces',f,'Vertices',muscle,'FaceColor',[0.6350 0.0780 0.1840],
   ...
    'FaceAlpha',.35,'linestyle','none')
legend({'Temperature','Epidermis','Dermis','Fat','Muscle'})
title({'Temperature Difference Across Tissue Depth',...
    ['Frequency: ' num2str(frequencyStart) 'GHz, Dermis Blood Flow: '
       ...
    num2str(bloodFlow(2)) 'ml/(s*ml)'],['Fat Thickness: '...
    num2str(tissueThickness(3)) 'mm, Incident Power: ' num2str(naughtI)
       ...
    'W/m^2']})
xlabel('Tissue Depth (mm)')
ylabel('Delta Temperature (C)')
ylim([0 oneLayerTemp])
```

Listing A.4: Thermal model based on Foster[27]

```
%Thermal response modeling of human skin based on the Foster
% paper. Combination of Pennes' Bioheat Equation with different
%tissue properties in order to show correct distribution of heat into
%tissue model
clear
clc
%Input variables
thermalConduc = [0.37 0.21 0.49 0.32]; %[W/m/C] tissue thermal
   conductivity
tissueDens = [1109 911 1090 1908 1050]; %[kg/m^3] tissue density
powerdBm = 12; %[dBm] power output from the transmitter
areaCM = 16; %[cm^2] area of distribution of power
bloodPerfusion = 1.767E-6; %[m^3/(kg/s)] volumetric perfusion rate of
   blood
%powerDensity = 10; %[W/m^2] incident power density on the tissue
transCoeff = 1; %energy transmission coefficient into the tissue
penetrationDepth = 0.41289; %[mm] energy penetration depth into the
   tissue
%for 77GHz, from: http://niremf.ifac.cnr.it/tissprop/htmlclie/htmlclie.
   php
tissueThickness = [0.1 1.5 8 15]; %[mm] tissue thickness
z = [tissueThickness(1) tissueThickness(1)+tissueThickness(2)...
```

```
    tissueThickness(1)+tissueThickness(2)+tissueThickness(3)...
    tissueThickness(4)]; %distance into tissue(mm)
tissueDepth = 0:0.1:tissueThickness(4); %[mm]incremental steps into
   tissue
tissueHeatCapac = [3391 2348 3421 1313 3617]; %[W*s/kg/C] the capacity
   of
%the tissue
time = 0:1:150; %[s] time array for measuring surface temperature

%Heat transfer of each tissue layer to predict temperature increase
zDepthSC = find(abs((tissueDepth-z(1)))<0.01);
zDepthSkin = find(abs((tissueDepth-z(2)))<0.001);
zDepthFat = find(abs((tissueDepth-z(3)))<0.001);
zDepthMuscle = length(tissueDepth);
areaThermalConduc = [repmat(thermalConduc(1),1,zDepthSC)...
    repmat(thermalConduc(2),1,zDepthSkin-zDepthSC)...
    repmat(thermalConduc(3),1,zDepthFat-zDepthSkin)...
    repmat(thermalConduc(4),1,zDepthMuscle-zDepthFat)];
areaTissueDens = [repmat(tissueDens(1),1,zDepthSC)...
    repmat(tissueDens(2),1,zDepthSkin-zDepthSC)...
    repmat(tissueDens(3),1,zDepthFat-zDepthSkin)...
    repmat(tissueDens(4),1,zDepthMuscle-zDepthFat)];
areaTissueHeatCapac = [repmat(tissueHeatCapac(1),1,zDepthSC)...
    repmat(tissueHeatCapac(2),1,zDepthSkin-zDepthSC)...
    repmat(tissueHeatCapac(3),1,zDepthFat-zDepthSkin)...
    repmat(tissueHeatCapac(4),1,zDepthMuscle-zDepthFat)];

%Calculate power density in W/m^2
powerW = 10^(powerdBm/10)/1000;
areaMeter = areaCM/10000;
powerDensity = powerW/areaMeter;
%Simplified form of Penne's bioheat equation (BHTE)
%calculate the microwave power deposition rate [W/kg]
SAR = (powerDensity.*transCoeff)./(areaTissueDens.*...
    (penetrationDepth/1000)).*exp(-(tissueDepth/1000)./...
    (penetrationDepth/1000));
%use SAR calc to find temperature differential at steady state
syms T
secDiffT = diff(diff(T));
tempRise = zeros(1,length(tissueDepth));
for k1 = 1:length(tissueDepth)
    SARcomp = SAR(k1);
    eqn = areaThermalConduc(k1)*secDiffT-areaTissueDens(k1)^2*...
        areaTissueHeatCapac(k1)*bloodPerfusion*T+areaTissueDens(k1)*...
        SARcomp == 0;
    solT = solve(eqn, T);
    tempRise(k1) = double(vpa(solT,5));
end
plot(tissueDepth,tempRise);
xlabel('Tissue Depth (mm)');
ylabel('Temperature (C)');
title('Delta Temperature Over Tissue Depth Using BHTE');
%Scaling Factor:1D Model:semi-infinite plane exposed to incident plane
   wave
%calculate time scales
alpha = areaThermalConduc/(areaTissueDens.*areaTissueHeatCapac);
```

```
tau1 = 1./(bloodPerfusion.*areaTissueDens);
tau2 = (penetrationDepth/1000)^2./alpha;
%calculate pure surface temperature with low perfusion rates
C1 = (2*powerDensity*transCoeff)./sqrt(pi.*areaThermalConduc.*...
    areaTissueDens.*areaTissueHeatCapac);
C2 = (powerDensity*transCoeff*(penetrationDepth/1000))./
    areaThermalConduc;
surfTemp = C1.*sqrt(time)-C2.*(1-exp(time/tau2).*erfc(sqrt(time/tau2)))
    ;
%calculate pure surface temperature with presence of blood flow
tauEff = (tau2-sqrt(tau1*tau2))./(tau2./(tau1-1));
steadyStateTemp = (SAR(1)/tissueHeatCapac(1))*tauEff;
%calculate the limiting value of steady state temperature when tau2<<
    tau1
ssTemp1D = (powerDensity*transCoeff)./(areaTissueDens.*...
    sqrt(areaTissueHeatCapac.*bloodPerfusion.*areaThermalConduc));
%plot surface temperature over time with no blood flow
%sqrtTime = sqrt(time);
%figure
%plot(sqrtTime,surfTemp);
%Scaling Factor: 2D Model: Irradiated disk with uniform irradiated area
%calculate uniform steady state temperature with R0/R1 going to
    infinity
R0 = sqrt(areaCM/10000);
R1 = sqrt(thermalConduc(1))/(tissueDens(1)*sqrt(bloodPerfusion*...
    tissueHeatCapac(1)));
x = R0/R1;
ssTemp2DUniform = ((powerDensity*transCoeff*R1)./areaThermalConduc)*...
    (1-exp(-x));
%calculate gaussian steady state temperature with R0/R1 going to
    infinity
ssTemp2DGaussian = ((powerDensity*transCoeff*R0*sqrt(pi))./...
    (2.*areaThermalConduc))*exp(x^2/4)*(1-erf(x/2));
figure
plot(tissueDepth,ssTemp2DUniform,tissueDepth,ssTemp2DGaussian,...
    tissueDepth,ssTemp1D);
legend('2D Uniform','2D Gaussian','1D');
```

A.2. Chapter 4 Matlab Code

Listing A.5: Code to extract data from files output by thermal camera

```
%read the asc files that come from the IR camera

clear
clc

folder = '\\tudelft.net\student-homes\r\cramsey\My Documents\Neonatal\
    Writing\Chapter4Pictures\77GHzCWHeatMaps\';

DataFolder = 'NearFieldOutsideIncubator\';

folder = strcat(folder,DataFolder);

ASCIIfiles=dir([folder '/*.asc']);
NumOfASCIIfiles=numel(ASCIIfiles);
```

```
ASCFile = extractFileText([folder ASCIIfiles(1).name]);
%Extract headers once
Startheaders = "T";
Endheaders = newline;
HeaderSetUp = extractBetween(ASCFile,Startheaders,Endheaders);
HeaderArray = split(HeaderSetUp);
HeaderArray(1) = "Time";
deviationFind = strfind(HeaderArray,"deviation");
numberofErrors = length(find([deviationFind{:}]==1));
for counter = 1:length(HeaderArray)
    if HeaderArray{counter,:} == "deviation"
        HeaderArray{counter,:} = [];
    end
end
HeaderArray(cellfun(@isempty,HeaderArray)) = [];
tableWidth = length(HeaderArray);
for ASCIIcount = 1:NumOfASCIIfiles
    %Extract rest of data
    ASCFile = extractFileText([folder ASCIIfiles(ASCIIcount).name]);
    DataString = split(ASCFile);
    DataString = DataString((length(HeaderArray)+numberofErrors+1):end
       -1);
    tableLength = length(DataString)/(tableWidth+1);
    DataString = reshape(DataString,[tableWidth+1,tableLength])';
    %Create Time Array in seconds
    HMS = str2double(split(DataString(:,2),':'));
    hours = -(HMS(1,1)-HMS(:,1));
    minutes = -(HMS(1,2)-HMS(:,2));
    seconds = -(HMS(1,3)-HMS(:,3));

    %put numbers in own array
    if ASCIIcount == 1
        DataNum = DataString(:,3:end);
        DataNum = str2double(strrep(DataNum,',','.'));
        TimeArray_s = hours*60*60+minutes*60+seconds+DataNum(:,1)/1000;
    else
        DataNum = [DataNum; DataString(:,3:end)];
        DataNum = str2double(strrep(DataNum,',','.'));

        AddlTime = hours*60*60+minutes*60+seconds+DataNum((101:end),1)
           /1000;
        TimeArray_s = [TimeArray_s; TimeArray_s(end)+AddlTime];
    end

end
%Plot values
HeaderArray = strrep(HeaderArray,'_',' ');
numCircles = (length(HeaderArray)-2)/5;
startCount = 1;
for circleCount = 1:numCircles
    maxLocation = 4+(circleCount-1)*5;
    avgLocation = 2+(circleCount-1)*5;
    minLocation = 3+(circleCount-1)*5;

    figure
    plot(TimeArray_s,DataNum(:,maxLocation),'LineWidth',2);
```

```
    hold on
    plot(TimeArray_s,DataNum(:,avgLocation),'LineWidth',2);
    plot(TimeArray_s,DataNum(:,minLocation),'LineWidth',2);
    xlabel('Time (sec)');
    ylabel('Temperature (C)');
    maxTemp = max(max(DataNum(:,maxLocation:end)))+0.05;
    minTemp = min(min(DataNum(:,minLocation)))-0.05;
    set(gca,'Fontsize',20);
    ylim([minTemp maxTemp]);
    if  startCount == 1
        [minimumVal,indexMin] = min(DataNum(:,avgLocation));
        startTime = TimeArray_s(indexMin);
    end
    startTime = 3.755; %for meat inside incubator
    indexMin = find((TimeArray_s-startTime)<0.0001,1,'last');
    startNewTime = 222.3;
    indexNew = find((TimeArray_s-startNewTime)<0.0001,1,'last');
    xline(startTime,'--b');
    %startTimeArray = startTime.*ones(1,length(TimeArray_s));
    %hold on
    %minToMaxTempStep = (maxTemp-minTemp)/(length(startTimeArray)-1);
    %minToMaxTemp = minTemp:minToMaxTempStep:maxTemp;
    %plot(startTimeArray,minToMaxTemp,'b--');
    averageTempBefore = mean(DataNum(1:indexMin,avgLocation));
    yline(averageTempBefore,'-.k');
    %hold on
    %averageTempBeforeArray = averageTempBefore.*ones(1,length(
        TimeArray_s));
    %plot(TimeArray_s,averageTempBeforeArray,'-.k');

    averageTempAfter = mean(DataNum(indexMin:indexNew,avgLocation));
    %averageTempAfterArray = averageTempAfter.*ones(1,length(
        TimeArray_s));

    yline(averageTempAfter,'-.k');
%     hold on
%     plot(TimeArray_s,averageTempAfterArray,'-.k');

    AVGaverageTempBefore = mean(DataNum(1:indexMin,avgLocation));
    AVGaverageTempAfter = mean(DataNum(indexMin:indexNew,avgLocation));
    MaxaverageTempBefore = mean(DataNum(1:indexMin,maxLocation));
    MaxaverageTempAfter = mean(DataNum(indexMin:indexNew,maxLocation));
    MinTempDelta = averageTempAfter-averageTempBefore;
    AverageTempDelta = AVGaverageTempAfter-AVGaverageTempBefore;
    MaximumTempDelta = MaxaverageTempAfter-MaxaverageTempBefore;
    title({'Change in Temperature Over Time For Adult Arm Inside
        Incubator at 35C, 20% Humidity For Far Field',['[Average Value
        Temperature Increase = ' num2str(MinTempDelta*1000) 'mC]']});
    %title('Change in Temperature Over Time For Adult Arm Outside
        Incubator for Far Field');
    legend(HeaderArray(maxLocation+1,1),HeaderArray(avgLocation+1,1),
        HeaderArray(minLocation+1,1),'Radar Start Time','Average Temp
        Before','Average Temp After');
    %legend(HeaderArray(maxLocation+1,1),HeaderArray(avgLocation+1,1),
        HeaderArray(minLocation+1,1));
    startCount = startCount+1;
```

```
end

if length(HeaderArray) > maxLocation + 2
    startLocation = maxLocation + 3;
    for pointLocation =  startLocation:length(HeaderArray)-1
        figure
        plot(TimeArray_s,DataNum(:,pointLocation),'LineWidth',2);
        xlabel('Time (sec)');
        ylabel('Temperature (C)');
        ylim([minTemp maxTemp]);
        xline(startTime,'--b');
        pointTempBefore = mean(DataNum(1:indexMin,pointLocation));
        yline(pointTempBefore,'-.k');
        pointTempAfter = mean(DataNum(indexMin:indexNew,pointLocation))
            ;
        pointTempDelta = pointTempAfter-pointTempBefore;
        yline(pointTempAfter,'-.k');
        title({'Change in Temperature Over Time For Meat Steak Inside
            Incubator at 35C, 20% Humidity For Far Field',['[Point
            Average Temperature Increase = ' num2str(pointTempDelta
            *1000) 'mC]']});
        legend(HeaderArray(pointLocation+1,1),'Radar Start Time','
            Average Temp Before','Average Temp After');
        set(gca,'Fontsize',20);
    end
end
```

Listing A.6: Signal processing to find heart and respiration rate

```
%Signal Processing To Find Heart And Respiration Rate
% Reads the .dat file that is created with CCS that contains the
% interleaved I and Q hex information and converts it into two columns
% containing decimal numbers. Then reads the profileconfig.txt file
% that contains the information of the chirp for that data file and
% calculates the time step and retrieves the sample frequency. Then
% plots the FFT of all the chirps, then divides the sample into
% individual chirps and plots one chirp as an example. Then calculates
% the bin size and finds the range bin that contains the peak
% frequency (position of the person) and plots the phase of the data.
% Then a bandpass filter is applied to the I and Q data and the max
% frequency is found containing the heart and respiration frequency.

clear
clc

%Import data
% import .dat file
datTable = readtable('Data\ProfileConfig4\HR_RR\Run1_Aug11_2020.dat');
if height(datTable) > 65280
    datArray = string(table2array(datTable(1:65280,1)));
else
    datArray = string(table2array(datTable(:,1)));
end
rx1QdataArray = zeros(length(datArray),1);
rx1IdataArray = zeros(length(datArray),1);
for extractCount = 1:length(datArray)
    Rx1QdataHex = datArray{extractCount,1}(1:4);
```

```
    rx1QdataArray(extractCount,1) = hex2dec(Rx1QdataHex);
    Rx1IdataHex = datArray{extractCount,1}(5:8);
    rx1IdataArray(extractCount,1) = hex2dec(Rx1IdataHex);
end
rx1Qdata = rx1QdataArray;
rx1Idata = rx1IdataArray;
% import txt file
filename = "ProfileConfig4\ProfileConfig.txt";
chirpConfiguration = extractFileText(filename);
% extract profile configuration data
startProfileCfg = "profileCfg ";
endProfileCfg = newline;
profileSetUp = str2num(extractBetween(chirpConfiguration,
   startProfileCfg,endProfileCfg));
% extract frame configuration data
startFrameCfg = "frameCfg ";
endFrameCfg = newline;
frameSetUp = str2num(extractBetween(chirpConfiguration,startFrameCfg,
   endFrameCfg));

%Variables
Fs = profileSetUp(11)*1E3; % Sampling frequency -- need smaller
   sampling frequency?
T = 1/Fs; % Sampling period
numOfSampsPerFrame = profileSetUp(10);
frameLength_ms = frameSetUp(5); %frame length (ms)
timeStep = (frameLength_ms/1e3)/numOfSampsPerFrame;
time = (0:timeStep:(timeStep*(length(rx1Qdata)-1)))';
L = length(time); % Length of signal
HRbw = [0.8 2]; %heart rate bandwidth for bandpass filter (Hz)
RRbw = [0.1 0.6]; %respiration rate bandwidth for bandpass filter (Hz)
%Plot I and Q data independently
figure
plot(time,rx1Idata);
hold on
plot(time,rx1Qdata);
xlim([0 100*timeStep])

%plot FFT of I and Q mixed together
sumIQ = rx1Idata+rx1Qdata;

sumIQfft = fft(sumIQ);
P2 = abs(sumIQfft/L);
P1 = P2(1:L/2+1);
P1(2:end-1) = 2*P1(2:end-1);

figure
f = Fs*(0:(L/2))/L;
plot(f,P1)
title('First FFT Single-Sided Amplitude Spectrum of X(t)')
xlabel('f (Hz)')
ylabel('|P1(f)|')

%Range bin selection: from one chirp and then add all bins together
% break time domain data into number of frames
numPointsperFrame = (frameLength_ms/1000)/timeStep;
```

```
numQelements = numel(rx1Qdata);
numIelements = numel(rx1Idata);
QcolumnsNum = floor(numQelements/numPointsperFrame);
IcolumnsNum = floor(numIelements/numPointsperFrame);
rx1Qdata = rx1Qdata(1:QcolumnsNum*numPointsperFrame);
rx1Idata = rx1Idata(1:IcolumnsNum*numPointsperFrame);
QframeArray = reshape(rx1Qdata,numPointsperFrame,QcolumnsNum);
IframeArray = reshape(rx1Idata,numPointsperFrame,IcolumnsNum);
%plot FFT of I and Q mixed together of different frames
sumIQFrames = (QframeArray+IframeArray);
sumIQfftperFrame = fft(sumIQFrames);
P2 = abs(sumIQfftperFrame/numPointsperFrame);
P1 = P2(1:numPointsperFrame/2+1);
P1(2:end-1) = 2*P1(2:end-1);
figure
f = Fs*(0:(numPointsperFrame/2))/numPointsperFrame;
plot(f,P1)
title('First FFT Of One Chirp Single-Sided Amplitude Spectrum of X(t)')
xlabel('f (Hz)')
ylabel('|P1(f)|')

%extract range bin
maxFreq = max(f);
totalTime = time(numPointsperFrame);
totalSamples = length(P1);
%remove DC component
P1 = P1(2:end-1);
f = f(2:end-1);
binSize = maxFreq/totalSamples; %bin size in Hz
[maxPeakmagFirstFFT, maxPeakindex] = max(P1); %find peak magnitude
binNum = maxPeakindex+2;
rangeBin = sumIQfftperFrame(binNum,:);
%extract phase from range bin
figure
Time = (1:1:length(rangeBin))*(frameLength_ms/1000);
ChirpNum = 1:1:length(rangeBin);
ly = length(rangeBin);
fy = (-ly/2:ly/2-1)/ly*Fs;
z = fftshift(rangeBin);
theta = angle(z);
q = unwrap(theta);
plot(Time,q,'-bo');
title('Range Bin Phase plot of first FFT for I and Q phase (Chest
   Displacement with Heart and Lungs)')
xlabel('Time (sec)')
%phase difference
phaseDiff = zeros(1,length(q));
phaseDiff(1) = q(1);
for counter = 1:length(q)-1
    phaseDiff(counter+1) = q(counter+1)-phaseDiff(counter);
end

%Bandpass filter for different rates of time signal to focus on
   respiration
%and heart rate
newSampleFreq = 1/(frameLength_ms/1000);
```

```
[PhaseDiffHR,d1] = bandpass(phaseDiff,HRbw,newSampleFreq);
[PhaseDiffRR,d3] = bandpass(phaseDiff,RRbw,newSampleFreq);
[qHR,d2] = bandpass(q,HRbw,newSampleFreq);
[qRR,d4] = bandpass(q,RRbw,newSampleFreq);
figure
plot(Time,PhaseDiffHR,'LineWidth',5);
title('Chest Displacement Caused by Heart Over Time')
xlabel('Time (sec)')
set(gca,'Fontsize',20);
figure
plot(Time,PhaseDiffRR,'LineWidth',5);
title('Chest Displacement Caused by Lungs Over Time')
xlabel('Time (sec)')
set(gca,'Fontsize',20);
%Find maximum of each fft
HRFFTsecond = fft(PhaseDiffHR);
HRFFTsecondP1 = abs(HRFFTsecond(1:IcolumnsNum/2+1));
HRFFTsecondP1(2:end-1) = 2*HRFFTsecondP1(2:end-1);
RRFFTsecond = fft(PhaseDiffRR);
RRFFTsecondP1 = abs(RRFFTsecond(1:IcolumnsNum/2+1));
RRFFTsecondP1(2:end-1) = 2*RRFFTsecondP1(2:end-1);
f2ndFFT = newSampleFreq*(0:(IcolumnsNum/2))/IcolumnsNum;
[maxHRMag, maxHRindex] = max(HRFFTsecondP1);
HzHR = f2ndFFT(maxHRindex);
if HzHR <0.8
    [aa,indices]=sort(HRFFTsecondP1,'descend');
    newIndexHR = indices(5);
    HzHR = f2ndFFT(newIndexHR);
end
[maxRRMag, maxRRindex] = max(RRFFTsecondP1);
HzRR = f2ndFFT(maxRRindex);
%Make decision
HeartRate_bpm = HzHR*60
RespirationRate_bpm = HzRR*60
```

Listing A.7: Signal processing to find maximum amplitude in first FFT

```
%Signal Processing To Find Maximum Amplitude
% Reads the .dat file that is created with CCS that contains the
% interleaved I and Q hex information and converts it into two columns
% containing decimal numbers. Then reads the profileconfig.txt file
% that contains the information of the chirp for that data file. Finds
% the bin containing the range and zooms in on that bin for all data
% files at different distances. Also plots the bins left and right of
% the center bins to show amplitude distribution across the bins

clear
clc

%Import data
filename = "\ProfileConfig4\ProfileConfig.txt";
dat1Table = readtable('Data\ProfileConfig4\BinMix\16cm_Run1_Aug19_2020.
    dat');
dat2Table = readtable('Data\ProfileConfig4\BinMix\16
    p001cm_Run1_Aug19_2020.dat');
dat3Table = readtable('Data\ProfileConfig4\BinMix\16
    p01cm_Run1_Aug19_2020.dat');
```

```
dat4Table = readtable('Data\ProfileConfig4\BinMix\16
    p02cm_Run1_Aug19_2020.dat');
dat5Table = readtable('Data\ProfileConfig4\BinMix\16
    p03cm_Run1_Aug19_2020.dat');

if height(dat1Table) > 65280
    dat1Array = string(table2array(dat1Table(1:65280,1)));
    dat2Array = string(table2array(dat2Table(1:65280,1)));
    dat3Array = string(table2array(dat3Table(1:65280,1)));
    dat4Array = string(table2array(dat4Table(1:65280,1)));
    dat5Array = string(table2array(dat5Table(1:65280,1)));
else
    dat1Array = string(table2array(dat1Table(:,1)));
    dat2Array = string(table2array(dat2Table(1:65280,1)));
    dat3Array = string(table2array(dat3Table(1:65280,1)));
    dat4Array = string(table2array(dat4Table(1:65280,1)));
    dat5Array = string(table2array(dat5Table(1:65280,1)));
end
Set1rx1QdataArray = zeros(length(dat1Array),1);
Set1rx1IdataArray = zeros(length(dat1Array),1);
Set2rx1QdataArray = zeros(length(dat1Array),1);
Set2rx1IdataArray = zeros(length(dat1Array),1);
Set3rx1QdataArray = zeros(length(dat1Array),1);
Set3rx1IdataArray = zeros(length(dat1Array),1);
Set4rx1QdataArray = zeros(length(dat1Array),1);
Set4rx1IdataArray = zeros(length(dat1Array),1);
Set5rx1QdataArray = zeros(length(dat1Array),1);
Set5rx1IdataArray = zeros(length(dat1Array),1);
for extractCount = 1:length(dat1Array)
    Rx1QdataHex = dat1Array{extractCount,1}(1:4);
    Set1rx1QdataArray(extractCount,1) = hex2dec(Rx1QdataHex);
    Rx1IdataHex = dat1Array{extractCount,1}(5:8);
    Set1rx1IdataArray(extractCount,1) = hex2dec(Rx1IdataHex);
    Rx1QdataHex = dat2Array{extractCount,1}(1:4);
    Set2rx1QdataArray(extractCount,1) = hex2dec(Rx1QdataHex);
    Rx1IdataHex = dat2Array{extractCount,1}(5:8);
    Set2rx1IdataArray(extractCount,1) = hex2dec(Rx1IdataHex);
    Rx1QdataHex = dat3Array{extractCount,1}(1:4);
    Set3rx1QdataArray(extractCount,1) = hex2dec(Rx1QdataHex);
    Rx1IdataHex = dat3Array{extractCount,1}(5:8);
    Set3rx1IdataArray(extractCount,1) = hex2dec(Rx1IdataHex);
    Rx1QdataHex = dat4Array{extractCount,1}(1:4);
    Set4rx1QdataArray(extractCount,1) = hex2dec(Rx1QdataHex);
    Rx1IdataHex = dat4Array{extractCount,1}(5:8);
    Set4rx1IdataArray(extractCount,1) = hex2dec(Rx1IdataHex);
    Rx1QdataHex = dat5Array{extractCount,1}(1:4);
    Set5rx1QdataArray(extractCount,1) = hex2dec(Rx1QdataHex);
    Rx1IdataHex = dat5Array{extractCount,1}(5:8);
    Set5rx1IdataArray(extractCount,1) = hex2dec(Rx1IdataHex);
end

Set1rx1Qdata = Set1rx1QdataArray;
Set1rx1Idata = Set1rx1IdataArray;
Set2rx1Qdata = Set2rx1QdataArray;
Set2rx1Idata = Set2rx1IdataArray;
Set3rx1Qdata = Set3rx1QdataArray;
```

```
Set3rx1Idata = Set3rx1IdataArray;
Set4rx1Qdata = Set4rx1QdataArray;
Set4rx1Idata = Set4rx1IdataArray;
Set5rx1Qdata = Set5rx1QdataArray;
Set5rx1Idata = Set5rx1IdataArray;
% import txt file
chirpConfiguration = extractFileText(filename);
% extract profile configuration data
startProfileCfg = "profileCfg ";
endProfileCfg = newline;
profileSetUp = str2num(extractBetween(chirpConfiguration,
    startProfileCfg,endProfileCfg));
% extract frame configuration data
startFrameCfg = "frameCfg ";
endFrameCfg = newline;
frameSetUp = str2num(extractBetween(chirpConfiguration,startFrameCfg,
    endFrameCfg));

%Variables
Fs = profileSetUp(11)*1E3; % Sampling frequency -- need smaller
    sampling frequency?
T = 1/Fs; % Sampling period
numOfSampsPerFrame = profileSetUp(10);
frameLength_ms = frameSetUp(5); %frame length (ms)
timeStep = (frameLength_ms/1e3)/numOfSampsPerFrame;
time = (0:timeStep:(timeStep*(length(Set1rx1Qdata)-1)))';
L = length(time); % Length of signal
BW = [9E3 11E3]; %bandwith, set by how much offset there is
BWSet1 = [99E3 101E3];
BWSet2 = [49E3 51E3];

%plot FFT of I and Q mixed together
sumIQSet1 = Set1rx1Idata+Set1rx1Qdata;
sumIQfftSet1 = fft(sumIQSet1);
P2Set1 = abs(sumIQfftSet1/L);
P1Set1 = P2Set1(1:L/2+1);
P1Set1(2:end-1) = 2*P1Set1(2:end-1);

sumIQSet2 = Set2rx1Idata+Set2rx1Qdata;
sumIQfftSet2 = fft(sumIQSet2);
P2Set2 = abs(sumIQfftSet2/L);
P1Set2 = P2Set2(1:L/2+1);
P1Set2(2:end-1) = 2*P1Set2(2:end-1);

sumIQSet3 = Set3rx1Idata+Set3rx1Qdata;
sumIQfftSet3 = fft(sumIQSet3);
P2Set3 = abs(sumIQfftSet3/L);
P1Set3 = P2Set3(1:L/2+1);
P1Set3(2:end-1) = 2*P1Set3(2:end-1);

sumIQSet4 = Set4rx1Idata+Set4rx1Qdata;
sumIQfftSet4 = fft(sumIQSet4);
P2Set4 = abs(sumIQfftSet4/L);
P1Set4 = P2Set4(1:L/2+1);
P1Set4(2:end-1) = 2*P1Set4(2:end-1);
```

```
sumIQSet5 = Set5rx1Idata+Set5rx1Qdata;
sumIQfftSet5 = fft(sumIQSet5);
P2Set5 = abs(sumIQfftSet5/L);
P1Set5 = P2Set5(1:L/2+1);
P1Set5(2:end-1) = 2*P1Set5(2:end-1);

subplot(1,3,2);
f = Fs*(0:(L/2))/L;
plot(f,P1Set1,'Linewidth',3)
hold on
plot(f,P1Set2)
hold on
plot(f,P1Set3)
hold on
plot(f,P1Set4)
hold on
plot(f,P1Set5)

title('Center Bin')
xlabel('f (Hz)')
ylabel('|P1(f)|')

%Range bin selection: from one chirp and then add all bins together
% break time domain data into number of frames
numPointsperFrame = (frameLength_ms/1000)/timeStep;
numQelements = numel(Set1rx1Qdata);
numIelements = numel(Set1rx1Idata);
QcolumnsNum = floor(numQelements/numPointsperFrame);
IcolumnsNum = floor(numIelements/numPointsperFrame);
Set1rx1Qdata = Set1rx1Qdata(1:QcolumnsNum*numPointsperFrame);
Set1rx1Idata = Set1rx1Idata(1:IcolumnsNum*numPointsperFrame);
Set2rx1Qdata = Set2rx1Qdata(1:QcolumnsNum*numPointsperFrame);
Set2rx1Idata = Set2rx1Idata(1:IcolumnsNum*numPointsperFrame);
Set1QframeArray = reshape(Set1rx1Qdata,numPointsperFrame,QcolumnsNum);
Set1IframeArray = reshape(Set1rx1Idata,numPointsperFrame,IcolumnsNum);
Set2QframeArray = reshape(Set2rx1Qdata,numPointsperFrame,QcolumnsNum);
Set2IframeArray = reshape(Set2rx1Idata,numPointsperFrame,IcolumnsNum);

%plot FFT of I and Q mixed together of different frames
Set1sumIQFrames = (Set1QframeArray+Set1IframeArray);
Set2sumIQFrames = (Set2QframeArray+Set2IframeArray);
Set1sumIQfftperFrame = fft(Set1sumIQFrames);
Set2sumIQfftperFrame = fft(Set2sumIQFrames);
Set1P2 = abs(Set1sumIQfftperFrame(:,1)/numPointsperFrame);
Set1P1 = Set1P2(1:numPointsperFrame/2+1);
Set1P1(2:end-1) = 2*Set1P1(2:end-1);
Set2P2 = abs(Set2sumIQfftperFrame(:,1)/numPointsperFrame);
Set2P1 = Set2P2(1:numPointsperFrame/2+1);
Set2P1(2:end-1) = 2*Set2P1(2:end-1);

 f = Fs*(0:(numPointsperFrame/2))/numPointsperFrame;

%extract range bin
maxFreq = max(f);
totalSamples = length(Set1P1);
binSize = maxFreq/totalSamples; %bin size in Hz
```

```
%remove DC component
Set1P1 = Set1P1(3:end-1);
Set2P1 = Set2P1(3:end-1);
f = f(3:end-1);
[Set1maxPeakmagFirstFFT, Set1maxPeakindex] = max(Set1P1); %find peak
    magnitude
binNumSet1 = Set1maxPeakindex+3;
rangeBinSet1 = Set1sumIQfftperFrame(binNumSet1,:);
[Set2maxPeakmagFirstFFT, Set2maxPeakindex] = max(Set2P1); %find peak
    magnitude
binNumSet2 = Set2maxPeakindex+3;
rangeBinSet2 = Set2sumIQfftperFrame(binNumSet2,:);
%
startFreqBin = f(binNumSet1)-binSize/100;
endFreqBin = f(binNumSet1)+binSize/100;
xlim([startFreqBin endFreqBin]);
ylim([0 16000]);
set(gca,'Fontsize',20);

subplot(1,3,1);
f = Fs*(0:(L/2))/L;
plot(f,P1Set1,'Linewidth',3)
hold on
plot(f,P1Set2)
hold on
plot(f,P1Set3)
hold on
plot(f,P1Set4)
hold on
plot(f,P1Set5)

title('Left Bin')
xlabel('f (Hz)')
ylabel('|P1(f)|')
f = Fs*(0:(numPointsperFrame/2))/numPointsperFrame;
f = f(3:end-1);
startFreqBin = f(binNumSet1-1)-binSize/100;
endFreqBin = f(binNumSet1-1)+binSize/100;
xlim([startFreqBin endFreqBin]);
ylim([0 16000]);
set(gca,'Fontsize',20);

subplot(1,3,3);
f = Fs*(0:(L/2))/L;
plot(f,P1Set1,'Linewidth',3)
hold on
plot(f,P1Set2)
hold on
plot(f,P1Set3)
hold on
plot(f,P1Set4)
hold on
plot(f,P1Set5)
legend('Start Location', '0.01mm Distance', '0.1mm Distance', '0.2mm
    Distance', '0.3mm Distance');
title('Right Bin')
```

```
xlabel('f (Hz)')
ylabel('|P1(f)|')
f = Fs*(0:(numPointsperFrame/2))/numPointsperFrame;
f = f(3:end-1);
startFreqBin = f(binNumSet1+1)-binSize/100;
endFreqBin = f(binNumSet1+1)+binSize/100;
xlim([startFreqBin endFreqBin]);
ylim([0 16000]);
set(gca,'Fontsize',20);
```

Listing A.8: Signal processing to intermodulation distortion of second FFT

```
%Signal Processing Function to Find Distortion
% Reads the .dat file that is created with CCS that contains the
% interleaved I and Q hex information and converts it into two columns
% containing decimal numbers. Then reads the profileconfig.txt file
% that contains the information of the chirp for that data file and
% calculates the time step and retrieves the sample frequency. Then
% plots the FFT of all the chirps, then divides the sample into
% individual chirps. Then calculates the range size and finds the
% range bin that contains the peak frequency (position of the person)
% then mixes the range bins together. Then plots the phase data. Also
% plots the frequency and does phase processing to get the new bin.
% Then does a second FFT of the new phase data and shows distortion.


clear
clc

%Import data
% import .dat file
filename = "\ProfileConfig4\ProfileConfig.txt";
dat1Table = readtable('Data\ProfileConfig4\BinMix\16cm_Run1_Aug19_2020.
    dat');
dat2Table = readtable('Data\ProfileConfig4\BinMix\16
    p001cm_Run1_Aug19_2020.dat');
if height(dat1Table) > 65280
     dat1Array = string(table2array(dat1Table(1:65280,1)));
     dat2Array = string(table2array(dat2Table(1:65280,1)));
else
     dat1Array = string(table2array(dat1Table(:,1)));
     dat2Array = string(table2array(dat2Table(1:65280,1)));
end
Set1rx1QdataArray = zeros(length(dat1Array),1);
Set1rx1IdataArray = zeros(length(dat1Array),1);
Set2rx1QdataArray = zeros(length(dat1Array),1);
Set2rx1IdataArray = zeros(length(dat1Array),1);
for extractCount = 1:length(dat1Array)
     Rx1QdataHex = dat1Array{extractCount,1}(1:4);
     Set1rx1QdataArray(extractCount,1) = hex2dec(Rx1QdataHex);
     Rx1IdataHex = dat1Array{extractCount,1}(5:8);
     Set1rx1IdataArray(extractCount,1) = hex2dec(Rx1IdataHex);
     Rx1QdataHex = dat2Array{extractCount,1}(1:4);
     Set2rx1QdataArray(extractCount,1) = hex2dec(Rx1QdataHex);
     Rx1IdataHex = dat2Array{extractCount,1}(5:8);
     Set2rx1IdataArray(extractCount,1) = hex2dec(Rx1IdataHex);
end
```

```
Set1rx1Qdata = Set1rx1QdataArray;
Set1rx1Idata = Set1rx1IdataArray;
Set2rx1Qdata = Set2rx1QdataArray;
Set2rx1Idata = Set2rx1IdataArray;
% import txt file
chirpConfiguration = extractFileText(filename);
% extract profile configuration data
startProfileCfg = "profileCfg ";
endProfileCfg = newline;
profileSetUp = str2num(extractBetween(chirpConfiguration,
    startProfileCfg,endProfileCfg));
% extract frame configuration data
startFrameCfg = "frameCfg ";
endFrameCfg = newline;
frameSetUp = str2num(extractBetween(chirpConfiguration,startFrameCfg,
    endFrameCfg));

%Variables
Fs = profileSetUp(11)*1E3; % Sampling frequency -- need smaller
    sampling frequency?
T = 1/Fs; % Sampling period
numOfSampsPerFrame = profileSetUp(10);
frameLength_ms = frameSetUp(5); %frame length (ms)
timeStep = (frameLength_ms/1e3)/numOfSampsPerFrame;
time = (0:timeStep:(timeStep*(length(Set1rx1Qdata)-1)))';
L = length(time); % Length of signal
BW = [9E3 11E3]; %bandwith, set by how much offset there is
BWSet1 = [99E3 101E3];
BWSet2 = [49E3 51E3];

%plot FFT of I and Q mixed together
sumIQSet1 = Set1rx1Idata+Set1rx1Qdata;
sumIQfftSet1 = fft(sumIQSet1);
P2Set1 = abs(sumIQfftSet1/L);
P1Set1 = P2Set1(1:L/2+1);
P1Set1(2:end-1) = 2*P1Set1(2:end-1);

sumIQSet2 = Set2rx1Idata+Set2rx1Qdata;
sumIQfftSet2 = fft(sumIQSet2);
P2Set2 = abs(sumIQfftSet2/L);
P1Set2 = P2Set2(1:L/2+1);
P1Set2(2:end-1) = 2*P1Set2(2:end-1);

f = Fs*(0:(L/2))/L;


%Range bin selection: from one chirp and then add all bins together
% break time domain data into number of frames
numPointsperFrame = (frameLength_ms/1000)/timeStep;
numQelements = numel(Set1rx1Qdata);
numIelements = numel(Set1rx1Idata);
QcolumnsNum = floor(numQelements/numPointsperFrame);
IcolumnsNum = floor(numIelements/numPointsperFrame);
Set1rx1Qdata = Set1rx1Qdata(1:QcolumnsNum*numPointsperFrame);
Set1rx1Idata = Set1rx1Idata(1:IcolumnsNum*numPointsperFrame);
Set2rx1Qdata = Set2rx1Qdata(1:QcolumnsNum*numPointsperFrame);
```

```
Set2rx1Idata = Set2rx1Idata(1:IcolumnsNum*numPointsperFrame);
Set1QframeArray = reshape(Set1rx1Qdata,numPointsperFrame,QcolumnsNum);
Set1IframeArray = reshape(Set1rx1Idata,numPointsperFrame,IcolumnsNum);
Set2QframeArray = reshape(Set2rx1Qdata,numPointsperFrame,QcolumnsNum);
Set2IframeArray = reshape(Set2rx1Idata,numPointsperFrame,IcolumnsNum);

%plot FFT of I and Q mixed together of different frames
Set1sumIQFrames = (Set1QframeArray+Set1IframeArray);
Set2sumIQFrames = (Set2QframeArray+Set2IframeArray);
Set1sumIQfftperFrame = fft(Set1sumIQFrames);
Set2sumIQfftperFrame = fft(Set2sumIQFrames);
Set1P2 = abs(Set1sumIQfftperFrame(:,1)/numPointsperFrame);
Set1P1 = Set1P2(1:numPointsperFrame/2+1);
Set1P1(2:end-1) = 2*Set1P1(2:end-1);
Set2P2 = abs(Set2sumIQfftperFrame(:,1)/numPointsperFrame);
Set2P1 = Set2P2(1:numPointsperFrame/2+1);
Set2P1(2:end-1) = 2*Set2P1(2:end-1);

f = Fs*(0:(numPointsperFrame/2))/numPointsperFrame;

%extract range bin
maxFreq = max(f);
totalSamples = length(Set1P1);
binSize = maxFreq/totalSamples; %bin size in Hz
%remove DC component
Set1P1 = Set1P1(3:end-1);
Set2P1 = Set2P1(3:end-1);
f = f(3:end-1);
[Set1maxPeakmagFirstFFT, Set1maxPeakindex] = max(Set1P1); %find peak
    magnitude
binNumSet1 = Set1maxPeakindex+3;
rangeBinSet1 = Set1sumIQfftperFrame(binNumSet1,:);
[Set2maxPeakmagFirstFFT, Set2maxPeakindex] = max(Set2P1); %find peak
    magnitude
binNumSet2 = Set2maxPeakindex+3;
rangeBinSet2 = Set2sumIQfftperFrame(binNumSet2,:);

%check to make sure bins are correct [TO DO]
if binNumSet1 == binNumSet2
    %extract phase from range bin
    %figure
    Time = (1:1:length(rangeBinSet1))*(frameLength_ms/1000);
    mixedBins = rangeBinSet1.*rangeBinSet2;
    newSampleFreq = 1/(frameLength_ms/1000);
    f2ndFFT = newSampleFreq*(0:(IcolumnsNum/2))/IcolumnsNum;

    MixedP1 = abs(mixedBins(1:IcolumnsNum/2+1));
    MixedP1(2:end-1) = 2*MixedP1(2:end-1);
    MixedP1 = fftshift(MixedP1);
    zMixed = fftshift(mixedBins);

    thetaMixed = angle(zMixed);
    qMixed = unwrap(thetaMixed/pi);


    %phase difference
```

```
    phaseDiff = zeros(1,length(qMixed));
    phaseDiff(1) = qMixed(1);
    for counter = 1:length(qMixed)-1
        phaseDiff(counter+1) = qMixed(counter+1)-phaseDiff(counter);
    end
    %figure
    %plot(Time, phaseDiff, '-b.');

    %Find maximum of each fft

    FFTsecond = fft(phaseDiff);
    FFTsecondP1 = abs(FFTsecond(1:IcolumnsNum/2+1));
    FFTsecondP1(2:end-1) = 2*FFTsecondP1(2:end-1);
    FFTsecondP1 = fftshift(FFTsecondP1);
    figure
    plot(f2ndFFT,FFTsecondP1,'LineWidth',5);
    title('Outer Third-Order Intercept Point (OIP3) of Mixed Range Bins
       ')
    ylabel('Magnitude')
    xlabel('Frequency (Hz)')
    %xlim([2 3]);
    set(gca,'Fontsize',20);
    %legend('5mm', '4mm','3mm','2mm','1mm');
else
    disp('Bins are not the same, adjust FMCW parameters to place
       measurements in one bin.');
end
```

Bibliography

[1] D. K. Stevenson *et al.*, “Very low birth weight outcomes of the National Institute of Child Health and Human Development Neonatal Research Network, January 1993 through December 1994," *American Journal of Obstetrics and Gynecology*, vol. 179, no. 6, pp. 1632-–1639, Dec. 1998.

[2] R. H. Steinhorn, “Persistent Pulmonary Hypertension of the Newborn," *Pediatric Critical Care Medicine*, vol. 11, no. 2, pp. S79–S84, Mar. 2010.

[3] K. D. Fairchild and T. M. Oshea, “Heart Rate Characteristics: Physiomarkers for Detection of Late-Onset Neonatal Sepsis," *Clinics in Perinatology*, vol. 37, no. 3, pp. 581–598, Sep. 2010.

[4] “Causes of newborn mortality and morbidity in the European Region," *World Health Organization*, 2012. [Online]. Available: http://www.euro.who.int/en/health-topics/Life-stages/maternal-and-newborn-health/causes-of-newborn-mortality-and-morbidity-in-the-european-region. [Accessed: 12-Jun-2019].

[5] A. Boardman, F. S. Schlindwein, N. V. Thakor, T. Kimura, and R. G. Geocadin, “Detection of asphyxia using heart rate variability," *Medical Biological Engineering & Computing*, vol. 40, no. 6, pp. 618–624, May 2002.

[6] Z. Kutlubay *et al.*, “Newborn Skin: Common Skin Problems," *MAEDICA – a Journal of Clinical Medicine*, vol. 12, no. 1, pp. 42—47, Mar. 2017.

[7] H. Uk Chung *et al.*, “Binodal, wireless epidermal electronic systems with in-sensor analytics for neonatal intensive care," *Science*, vol. 363, no. 6430, Mar. 2019.

[8] J. Dudink and A. V. D. Hoogen, “Assessing, improving and utilizing sleep in high risk neonates," *Early Human Development*, vol. 113, p. 77, Jul. 2017.

[9] R. Flacking *et al.*, “Closeness and separation in neonatal intensive care," *Acta Paediatrica*, vol. 101, no. 10, pp. 1032-–1037, Jul. 2012.

[10] R. Aihara and Y. Fujimoto, “Free-Space Estimation for Self-Driving System Using Millimeter Wave Radar and Convolutional Neural Network," *2019 IEEE International Conference on Mechatronics (ICM)*, 2019.

[11] M. Alizadeh, G. Shaker, J. C. M. D. Almeida, P. P. Morita, and S. Safavi-Naeini, “Remote Monitoring of Human Vital Signs Using mm-Wave FMCW Radar," IEEE Access, vol. 7, pp. 54958–54968, Apr. 2019.

[12] C. Iovescu and S. Rao, “The fundamentals of millimeter wave - TI.com." [Online]. Available: http://www.ti.com/lit/wp/spyy005/spyy005.pdf. [Accessed: 03-Apr-2020].

[13] R. McMillan, “Terahertz Imaging, Millimeter-Wave Radar," *Advances in Sensing with Security Applications (NATO Security Through Science Series)*, VOL. 2, P. 243-268, 2006.

[14] M. Caris, S. Stanko, W. Johannes, S. Sieger, and N. Pohl, “Detection and tracking of micro aerial vehicles with millimeter wave radar," *2016 46th European Microwave Conference (EuMC)*, Oct. 2016.

[15] A. Ahmad, “Driver vital sign detection demonstration using mmWave radar sensors," *TI Training*, 13-Sep-2018. [Online]. Available: https://training.ti.com/driver-vital-sign-detection-demonstration-using-mmwave-radar-sensors. [Accessed: 03-Apr-2020].

[16] *Dielectric Properties of Body Tissues: HTML clients*, 2015. [Online]. Available: http://niremf.ifac.cnr.it/tissprop/htmlclie/htmlclie.php. [Accessed: 03-Apr-2020].

[17] A. Ahmad, J. C. Roh, D. Wang, and A. Dubey, “Vital signs monitoring of multiple people using a FMCW millimeter-wave sensor," *2018 IEEE Radar Conference (RadarConf18)*, 2018.

[18] M. Solis Vu, “SOMNUS: An Ultra-Wideband Radar-Based Approach for Neonatal Sleep State Classification", M.S. thesis, Delft University of Technology, 2017.

[19] R. L. Stavis, By, R. L. Stavis, and Last full review/revision Jun 2019| Content last modified Jun 2019, “Premature Newborn - Children’s Health Issues," *MSD Manual Consumer Version*, Jun-2019. [Online]. Available: https://www.msdmanuals.com/home/children-s-health-issues/general-problems-in-newborns/premature-newborn. [Accessed: 03-Apr-2020].

[20] “Apnea and Bradycardia," *Apnea and Bradycardia | Emory School of Medicine*. [Online]. Available: https://med.emory.edu/departments/pediatrics/divisions/neonatology/apnea.html. [Accessed: 03-Apr-2020].

[21] V. Oliveira *et al.*, “Early Postnatal Heart Rate Variability in Healthy Newborn Infants," *Frontiers in Physiology*, vol. 10, Aug. 2019.

[22] *IEEE Standard for Safety Levels with Respect to Human Exposure to the Radio Frequency Electromagnetic Fields, 3 kHz to 300 GHz*, IEEE Standard C95.1, 2005.

[23] T. Wu, T. S. Rappaport, and C. M. Collins, “Safe for Generations to Come: Considerations of Safety for Millimeter Waves in Wireless Communications," *IEEE Microwave Magazine*, vol. 16, no. 2, pp. 65–84, Mar. 2015.

[24] M. C. Ziskin, S. I. Alekseev, K. R. Foster, and Q. Balzano, “Tissue models for RF exposure evaluation at frequencies above 6GHz," *Bioelectromagnetics*, vol. 39, no. 3, pp. 173–189, Feb. 2018.

[25] M. Jajoo, K. Kapoor, L. Garg, V. Manchanda, and S. Mittal, “To study the incidence and risk factors of early onset neonatal sepsis in an out born neonatal intensive care unit of India," *Journal of Clinical Neonatology*, vol. 4, no. 2, p. 91, Apr. 2015.

[26] “Sepsis," *Mayo Clinic*, 16-Nov-2018. [Online]. Available: https://www.mayoclinic.org/diseases-conditions/sepsis/symptoms-causes/syc-20351214. [Accessed: 06-Apr-2020].

[27] K. R. Foster, M. C. Ziskin, and Q. Balzano, “Thermal Response of Human Skin to Microwave Energy," *Health Physics*, vol. 111, no. 6, pp. 528–541, Dec. 2016.

[28] R. B. Knobel and D. Holditch-Davis, “Physiological effects of thermoregulation in transitional ELBW infants", Ph.D. Dissertation, University of North Carolina at Chapel Hill, 2006.

[29] T. Wu, T. S. Rappaport, and C. M. Collins, “The human body and millimeter-wave wireless communication systems: Interactions and implications," *2015 IEEE International Conference on Communications (ICC)*, Jul. 2015.

[30] A. Sola, J. Perez, S. Golombek, and C. Fajardo, “A laminar flow unit for the care of critically ill newborn infants," *Medical Devices: Evidence and Research*, p. 163, 2013.

[31] M. K. Logani, A. Bhanushali, M. C. Ziskin, and T. J. Prihoda, ”Micronuclei in peripheral blood and bone marrow cells of mice exposed to 42 GHz electromagnetic millimeter waves," *Radiat. Res.*, vol. 161, no. 3, pp. 341–345, 2004.

[32] C. Le Quément, C. N. Nicolaz, M. Zhadobov, F. Desmots, R. Sauleau, M. Aubry, D. Michel, and Y. Le Dréan, ”Whole-genome expression analysis in primary human keratinocyte cell cultures exposed to 60 GHz radiation," *Bioelectromagnetics*, vol. 33, no. 2, pp. 147–158, 2012.

[33] M. Zhadobov, R. Sauleau, L. Le Coq, L. Debure, D. Thouroude, D. Michel, and Y. Le Dréan, “Low-power millimeter wave radiations do not alter stress-sensitive gene expression of chaperone proteins," *Bioelectromagnetics*, vol. 28, no. 3, pp. 188–196, 2007.

[34] A. Beneduci, G. Chidichimo, R. De Rose, L. Filippelli, S. V. Straface, and S. Venuta, “Frequency and irradiation time-dependant antiproliferative effect of low-power millimeter waves on RPMI 7932 human melanoma cell line," *Anticancer Res.*, vol. 25, no. 2A, pp. 1023–1028, Mar. 2005.

[35] A. A. Radzievsky, O. V. Gordiienko, I. Szabo, S. I. Alekseev, and M. C. Ziskin, "Millimeter wave-induced suppression of B16 F10 melanoma growth in mice: Involvement of endogenous opioids," *Bioelectromagnetics*, vol. 25, no. 6, pp. 466–473, Sept. 2004.

[36] M. K. Logani, I. Szabo, V. Makar, A. Bhanushali, S. Alekseev, and M. C. Ziskin, "Effect of millimeter wave irradiation on tumor metastasis," *Bioelectromagnetics*, vol. 27, no. 4, pp. 258–264, 2006.

[37] M. A. Rojavin and M. C. Ziskin, "Medical application of millimetre waves," *Q. J. Med.*, vol. 91, no. 1, pp. 57–66, 1998.

[38] A. B. Gapeyev, E. N. Mikhailik, and N. K. Chemeris, "Antiinflammatory effects of low-intensity extremely high-frequency electromagnetic radiation: Frequency and power dependence," *Bioelectromagnetics*, vol. 29, no. 3, pp. 197–206, Apr. 2008.

[39] A. B. Gapeyev, E. N. Mikhailik, and N. K. Chemeris, "Features of anti-inflammatory effects of modulated extremely high-frequency electromagnetic radiation," *Bioelectromagnetics*, vol. 30, no. 6, pp. 454–461, Sept. 2009.

[40] M. Zhadobov, R. Sauleau, V. Vie, M. Himdi, L. Le Coq, and D. Thouroude, "Interactions between 60-GHz millimeter waves and artificial biological membranes: Dependence on radiation parameters," *IEEE Trans. Microwave Theory Tech.*, vol. 54, no. 6, pp. 2534–2542, 2006.

[41] I. Szabo, J. Kappelmayer, S. I. Alekseev, and M. C. Ziskin, "Millimeter wave induced reversible externalization of phosphatidylserine molecules in cells exposed in vitro," *Bioelectromagnetics*, vol. 27, no. 3, pp. 233–244, 2006.

[42] Y. Le Dréan, Y. S. Mahamoud, Y. Le Page, D. Habauzit, C. Le. Quément, M. Zhadobov, and R. Sauleau, "State of knowledge on biological effects at 40–60 GHz," *Comptes Rendus Physique*, vol. 14, no. 5, pp. 402–411, May 2013.

[43] H. P. Schwan and K. R. Foster, "RF-field interactions with biological systems: Electrical properties and biophysical mechanisms," *Proc. IEEE*, vol. 68, no. 1, pp. 104–113, Jan. 1980.

[44] *Thermal protection of the newborn: a practical guide*. Geneva: Maternal and Newborn Health/Safe Motherhood Unit, Division of Reproductive Health (Technical Support), World Health Organization, 1997.

[45] S. Delanaud, F. C. Yassin, E. Durand, P. Tourneux, and J.-P. Libert, "Can Mathematical Models of Body Heat Exchanges Accurately Predict Thermal Stress in Premature Neonates?," *Applied Sciences*, vol. 9, no. 8, p. 1541, 2019.

[46] K. Belghazi, P. Tourneux, E. B. Elabbassi, L. Ghyselen, S. Delanaud, and J.-P. Libert, "Effect of posture on the thermal efficiency of a plastic bag wrapping in neonate: Assessment using a thermal 'sweating' mannequin," *Medical Physics*, vol. 33, no. 3, pp. 637–644, 2006.

[47] A. E. Wheldon, "Energy balance in the newborn baby: use of a manikin to estimate radiant and convective heat loss," *Physics in Medicine and Biology*, vol. 27, no. 2, pp. 285–296, 1982.

[48] A. Kanezaki, S. Watanabe, A. Hirata, and H. Shirai, "Theoretical Analysis for Temperature Elevation of Human Body Due to Millimeter Wave Exposure," *2008 Cairo International Biomedical Engineering Conference*, 2008.

[49] M. Alonso-Delpino, M. D. Rosa, M. Simeoni, M. Spella, C. D. Martino, and M. Spirito, "A Planar Near-Field Setup for Millimeter-Wave System-Embedded Antenna Testing," *IEEE Antennas and Wireless Propagation Letters*, vol. 16, pp. 83–86, 2017.